Textile-based Sensors for In-situ Monitoring in Electrochemical Cells and Biomedical Applications

by

Sadegh Hasanpour
B.Sc., University of Tehran, 2013
M.Sc., The University of British Columbia, 2016

A Dissertation Submitted in Partial Fulfillment of the
Requirements for the Degree of

DOCTOR OF PHILOSOPHY

in the Department of Mechanical Engineering

Textile-based Sensors for In-situ Monitoring in Electrochemical Cells and Biomedical Applications

by

Sadegh Hasanpour
B.Sc., University of Tehran, 2013
M.Sc., The University of British Columbia, 2016

Supervisory Committee

Dr. Ned Djilali, Co-Supervisor
(Department of Mechanical Engineering)

Dr. Mohsen Akbari, Co-Supervisor
(Department of Mechanical Engineering)

Dr. Jeremy Wulff, Outside Member
(Department of Chemistry)

Supervisory Committee

Dr. Ned Djilali, Co-Supervisor
(Department of Mechanical Engineering)

Dr. Mohsen Akbari, Co-Supervisor
(Department of Mechanical Engineering)

Dr. Jeremy Wulff, Outside Member
(Department of Chemistry)

ABSTRACT

This work explores the blending of e-textile technology with the porous electrode of polymer electrolyte membrane fuel cells (PEMFCs) and with smart wound patches to allow monitoring and in-situ diagnostics. This work includes contributions to understanding water transport and conductivity in the carbon cloth gas diffusion layer (GDL), and further developing thread-based relative humidity (RH) and temperature sensors, which can be sewn on a cloth GDL in PEMFCs. We also explore the application of the developed RH and temperature sensors in wearable biomonitoring.

First, an experimental prototype is developed for evaluating water transport, thermal conductivity and electrical conductivity of carbon cloth GDLs under different hydrophobic coatings and compressions. Second, we demonstrate the addition of external threads to the carbon cloth GDL to (1) facilitate water transport and (2) measure local RH and temperature with a minimal impact on the physical, microstructural and transport properties of the GDL. We illustrate the roll-to-roll process for fabricating RH and temperature sensors by dip-coating commodity threads into a carbon nanotubes (CNTs) suspension. The thread-based sensors response to RH and temperature in the working environment of PEMFCs is investigated. As a proof-of-concept, the local temperature of carbon cloth GDL is monitored in an ex-situ experiment.

Finally, we optimized the coating parameters (e.g. CNTs concentration, surfactant concentration and a number of dipping) for the thread-based sensors. The response of the thread-based sensors in room conditions is evaluated and shows a linear resistance decrease to temperature and a quadratic resistance increase to RH. We also evaluated the biocompatibility of the sensors by performing cell cytotoxicity and studying wound healing in an animal model. The novel thread-based sensors are not only applicable for textile electrochemical devices but also, show a promising future in wearable biomonitoring applications.

Contents

List of Tables

List of Figures

ACKNOWLEDGEMENTS

First, I would like to thank my supervisors Dr. Mohsen Akbari and Dr. Ned Djilali, for their support and trust during my Ph.D. time at the University of Victoria. I learned not to be afraid of exploring new topics, learning and growing. I want to thank Dr. Jeremy Wulff for his fruitful suggestions and revisions on my proposal and thesis.

I want to thank Laboratory for Innovation in Microengineering (LiME) members, Tavia Walsh, Maryam Jahanshahi, Zhina Hadisi and Lucas Karperian, that they helped me to carry out my research. I also want to thank Institute for Integrated Energy Systems (IESVic) for providing me with social support and opportunities to meet many enthusiastic and knowledgeable researchers in the field of sustainable energy and especially thanks to Pauline providing such a welcoming environment there.

I would like to thank Shanna Knights, Alan Young, and Monica Dutta for providing an opportunity for carrying out parts of the experimental work and doing my internship at Ballard Power Systems. I also want to acknowledge Dr. Mohammad Ahadi and Armin Rashidi for their collaborations on the experimental parts of my thesis at SFU and UBC, respectively.

Finally, I want to thank my friends and family who supported me over the last four years. Specifically, I want to acknowledge my supportive friend, Mehran, who has helped me over the previous years.

My sincere gratitude goes to my parents, who have always been there for me and supported me in all difficult and happy times.

DEDICATION

To my parents (Safoura and Ghorbanali), they were there for me when I needed them the most.

Chapter 1

Introduction

Freedom of thought is best promoted by the gradual illumination of men's minds which follows from the advance of science.

Charles Darwin

This dissertation describes new contributions to (i) characterize transport properties in carbon cloth gas diffusion layers (GDLs) and (ii) develop textile sensors for monitoring relative humidity (RH) and temperature in polymer electrolyte membrane fuel cells (PEMFCs) and evaluate the sensors for wearable biomonitoring applications. Section 1.1 discusses the research background and motivation of this study. The literature review section is organized into five subsections: Sections 1.2.1 and 1.2.2 review the characterization methods for GDL water transport and conductivity; Section 1.2.3 and 1.2.4 provide an overview of water management strategies and in-situ temperature and RH diagnostics for PEMFCs; and Section 1.2.5 is a brief overview of the development of fibre-based RH and temperature sensors. The objectives and structure of the thesis are presented in Section 1.3 and 1.4.

1.1 Background and Motivation

PEMFCs use hydrogen and oxygen in the anode and cathode side and produce electricity and water in the cell. Figure 1.1 illustrates the geometry of a single cell of a membrane electrode assembly (MEA) with flow fields on the cathode and anode sides. A stack of PEMFCs consists of several cells connected in parallel to provide the desired power output. Each cell consists of five main constituent layers. Reactant

gases travel through these layers from the flow field to the reaction zone. Each constituent has specific functions ensuring optimum performance of the cell. Each layer is described below.

Membrane: The core of each cell is a proton conductive membrane responsible for conducting protons and blocking electrons. Nafion membranes are widely used materials that have high protonic conductivity in a hydrated environment.

Catalyst Layer (CL): This thin porous layer consists of catalyst particles (i.e. platinum), ionomers (i.e. perfluorosulfonic acid (PFSA)) for transferring protons, conductive support particles (i.e. carbon) for transferring electrons and pores for transporting the reactant and by-product. The amount of catalyst particles is higher on the cathodic side due to sluggish cathode reaction kinetics. The CL is typically around 5-10 µm thick and is either coated on the membrane or the microporous layer (MPL) side.

Microporous layer (MPL): MPL has carbon particles combined with a hydrophobic polymer (e.g. polytetrafluoroethetylene (PTFE)), which are sintered on top of the GDL to provide an interface between the CL and the GDL, reduce the contact resistance between GDL and CL, and provide uniform distribution of reactants in the CL and effectively remove water from the CL to the GDL. This layer has a porosity around 25% and pore size distribution in order of 20 to 500 nm. Depending on the manufacturing process, it might have cracks on the surface.

Gas diffusion layer (GDL): this highly porous layer (porosity 70 to 90%) provides pathways for reactants, by-products and electron transport in and out of the cell. The thickness of this layer is in the range of 100 to 300 µm with pore sizes of around 10-100 µm. Carbon-based GDLs are widely used and they are coated with hydrophobic polymers mainly PTFE or in some cases with fluoroethylenpropylene (FEP). Two main groups are woven and non-woven GDLs. Woven GDLs are also known as carbon cloth are fabricated by weaving carbon fibers. Non-woven GDLs are fabricated with a random distribution of carbon fibers with a binding that improves the mechanical stability of the GDLs. The GDL is an ortothropic material that has different transport properties in the in-plane and through-plane directions. The former is the direction across the thickness of the GDL and the latter is the direction in the plane of GDL.

Flow field plate: The flow field consists of channels to uniformly distribute reactant over the whole active area of the cell; it is also a pathway to collect electrons and remove by-products (i.e. water) out of the cell. Different designs of channels

exist such as parallel, straight line, interdigitated or serpentine. Each has pros and cons due to different modes of transport or pressure drops from the inlet to the outlet of the cell.

This work is motivated by the need to better understand the carbon cloth GDL transport properties and to explore potential opportunities for developing textile-based sensors not only for electrochemical devices such as PEMFCs but also for wearable biomonitoring applications. A flexible carbon cloth GDL is suitable to embed fibers for enhancing water transport or sensing for further improving the performance and integrate *in-situ* PEMFCs diagnostics.

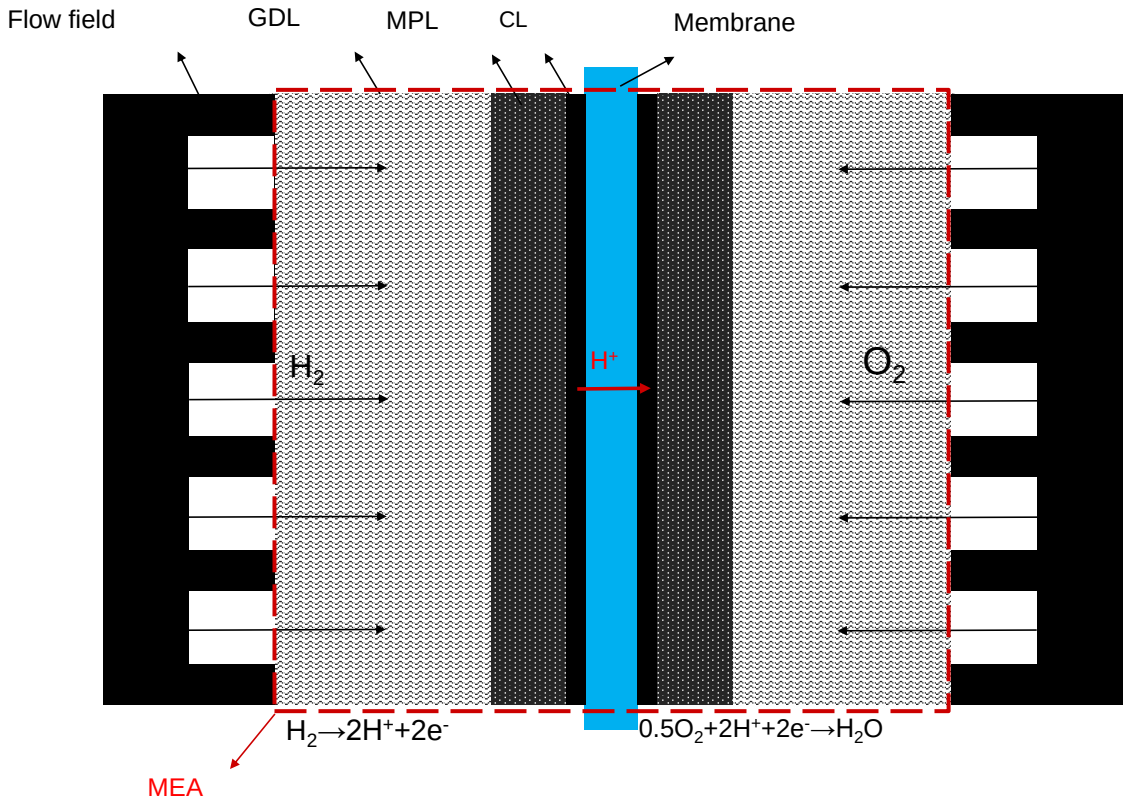

Figure 1.1: Schematic of the main components of a single cell PEMFCs with reactants directions and electrochemical reactions.

1.2 Literature Review

This section reviews the progress in the literature toward developing experimental procedures for (1) evaluating water transport, thermal conductivity and electrical conductivity of GDLs; (2) improving water management within GDLs through different physical modifications, addition of external components, or chemical modifications; (3) monitoring local temperature and RH within PEMFCs; and (4) developing fibre-based RH and temperature sensors.

1.2.1 Water Transport and Conductivity Analysis of GDLs of PEMFCs

Various studies show that coating GDLs with hydrophobic polymer improves the performance of PEMFCs [6, 7]. Hydrophobic coating facilitates water removal from the cell, specifically in high current density. Since the operating temperature is commonly between 60 °C and 90 °C, a combination of liquid water and water vapour exists within GDLs. The vapour phase is transported predominantly by diffusion due to concentration and temperature gradients between GDLs and channels. The liquid phase transport is dominated by capillary transport, which is a function of the structure and internal wettability of the GDLs pores [8]. Liquid water leaves the GDL through minimal pressure pathways [5]. Commercial GDLs are made out of carbon fibres and are treated with hydrophobic polymers to avoid the accumulation of water within GDL pores, a phenomenon known as "*flooding*". Common industrial practice is to coat GDLs with PTFE via dipping, spraying or brushing; this is known as a bulk treatment. The amount of PTFE is usually between 5% to 30 wt% [9]. Based on the coating procedure, the distribution of PTFE in GDLs varies. Mathias et al. [9] showed that slow drying (e.g. air drying) results in uniform PTFE distributions with more PTFE in the center of the GDL and fast drying (e.g. convective oven) results in more accumulation of PTFE near the surface of the GDL. Bazylak et al. [10] combined scanning electron microscopy (SEM) and energy-dispersive X-ray spectroscopy (EDS) analysis to monitor the distribution of PTFE in the through-plane for three types of commercial GDLs (paper, felt and cloth) with 10 wt% PTFE added to the GDLs. The results show that the paper GDL have higher accumulation of PTFE near the surface resulting in a 5% porosity drop near the surface; however, PTFE distributes more evenly in carbon cloth GDLs due to the transverse structure

of carbon fibres [11]. PTFE distribution changes the properties of the materials and affects transport properties, thermal and electrical conductivity and water transport behaviours within the microstructure.

GDLs in an operating fuel cell are under compression. The compression reduces contact resistances and provides sealing, resulting in optimum performance for the cell [12]. This compression has a direct impact on porous structure and on the effective transport properties. As a result of the collector plates geometry, the GDL in an operating fuel cell experiences non-uniform compression. It is, therefore, essential to characterize the properties of the GDL under non-homogenous compression, particularly for thermal conductivity, electrical conductivity and water transport.

Water management is a complex process that needs to be carefully considered in different components of the PEMFCs. On the one hand, the polymer membrane requires sufficient hydration, and on the other hand, the porous structure of GDLs, MPLs and CL need to remain fully opened (i.e. free of liquid water) under a variety of different operating conditions. The multi-objective aspects of water management have impacts on overall performance, and different strategies are necessary for the various PEMFCs components: (1) membrane, (2) CL, (3) MPL, (4) GDL and (5) channels. Since GDL water transport is the focus of this work it is discussed next in more detail [6].

Pattern of water transport within GDLs

The determination of water transport in the 3D anisotropic structure of GDLs is complicated and has been investigated through numerical [13] and experimental modeling [14, 15, 16]. Innovative methods to track water transport experimentally mainly rely on liquid water visualization techniques [17]. The capability of each imaging technique depends on (1) spatial and temporal resolutions, (2) capability for in-situ testing with minimal invasiveness, (3) compatibility with materials and (4) accessibility. Neutron imaging is capable of detecting water within GDLs due to high sensitivity to hydrogen atoms in water, and is a suitable technique to observe water transport in operating fuel cells [18]. However, the low resolution is not favourable for tracking transport at the microstructural level; also, accessibility to this imaging technique is limited. X-ray microtomography (X-µCT), which has been used widely for analysis of porous structures, has also been used to track water transport in ex-situ [16] and in operando fuel cell [19]. However, for 3D imaging, the technique is not capable of dynamic track-

Table 1.1: Summary of liquid water visualization techniques for GDL.

Research	Imaging	Spatial resolution	Temporal resolution	Type	Merits	Challenges
Bazylak et al. [15]	FS	21.4 µm	0.3 s	Carbon paper	Online tracking of water	Limited depth of field
Zenyuk et al. [21]	X-ray	1.3 µm	8 min	Carbon paper	Water distribution in micron level	Scanning time does not allow dynamic monitoring of water
Wu et al. [22]	Neutron imaging	26 µm	5 s	Carbon paper	Good sensitivity to water	It does not generate water distribution in micron level
Gostick et al. [23]	X-ray	1.3 µm	2 min	Carbon paper	Water distribution in microstructural level was obtained	Time of scan does not allow dynamic monitoring of water

ing due to the required imaging time. On the other hand, synchrotron X-ray shows promising results by scanning at the sub-second for tracking dynamic water transport [20]. Florescent (FS) microscopy provides high temporal and special resolutions that can give good descriptive behaviour water transport of GDLs [14, 15]; however, the challenge associated with this imaging technique is the production of 2D images with limited depth of field. Research has focused on the mechanism of water transport within non-woven GDL which are increasingly used in industry, with relatively little work on woven GDLs. Table 1.1 lists ex-situ techniques for observing water transport with a focus on compression and hydrophobic treatment.

1.2.2 Electrical and Thermal Conductivity

Electrical and thermal conductivities are important properties that have direct effects on ohmic losses and thermal management of the cell, respectively. As a result, high thermal and electrical conductivity are necessary for optimum performance of the cell, and their correct estimation are essential to predicting cell performance.

Electrical conductivity measurement methods

Electrons are generated in the CL and transport through different constituents of the cell. The flow of electrons is accompanied by ohmic losses that consist of the internal resistances of materials and interfacial contact resistances between components (e.g. the GDL and the CL interface). The protonic current in the membrane also generates

ohmic losses. The internal resistances are a function of morphology, hydrophobic treatment and compression of each component. Here, we examine, briefly, methods to measure the electrical conductivity of the GDL.

The measurement of the in-plane conductivity is performed by a four-point probe to effectively exclude the effect of contact resistance, as shown in Figure 1.2. Furthermore, since the conductivity is measured along the fibre in the in-plane directions, the impact of compression and hydrophobic treatment is minimal. Conductivity measurement in the through-plane direction is challenging since a four-point probe measurement along a thin layer of GDL is not feasible. In addition, the effect of compression on the through-plane direction is significant as the mechanism of conductivity is due to fibre-to-fibre connections. In addition, hydrophobic treatment, which covers the outer layer of fibres, affects the through-plane electrical conductivity. The through-plane resistivity for the schematic shown in Figure 1.2(b) is:

$$R_{total} = 2R_e + R_s + R_{GDL} + R_{GDL-s} + R_{s-e} \tag{1.1}$$

where R_e is the bulk resistance of the copper electrode, R_s is the bulk resistance of stainless-steel disk, R_{GDL} is the resistance of the GDL, R_{GDL-s} is the interfacial resistance between the GDL and the stainless steel and R_{S-e} is the interfacial resistance between the stainless-steel disc and the copper electrode. The apparatus resistance (R_a) is measured when no GDL is between the probes.

$$R_a = 2R_e + R_s + R_{s-e} \tag{1.2}$$

To effectively find the interfacial resistance (R_{GDL-s}) and R_{GDL}, samples of the GDL with different thicknesses are required. Then, by plotting the resistance vs. thickness, the y-intercept represents the interfacial resistance, and two resistances can be effectively separated. However, this method is not applicable if samples of different thicknesses are unavailable (which is the case for some GDL samples). In addition, the effect of the hydrophobic coating distribution across the through-plane direction is not uniform even for similar GDLs with different thicknesses, which causes errors in measurement. For these cases, (1) using a gold plate as an electrode to reduce the contact resistance and (2) stacking the same GDLs to make a thicker sample are approaches to separate the GDL resistance from contact resistances effectively.

The in-plane electrical conductivity is an order of magnitude higher than the

through-plane conductivity, which allows the proper utilization of the entire GDL [9]. Also, it is shown that the limiting factor in ohmic losses is the through-plane direction [9]. Compression on electrical conductivity is more critical when the sample is coated with hydrophobic coatings, which tend to accumulate near the surface area and also changes the distribution of the hydrophobic polymer in the through-plane direction. Although the contact resistance between GDL and bipolar plates plays a significant role in the through-plane conductivity, the effect of hydrophobic coating on the intrinsic through-plane conductivity of GDL is not well-understood.

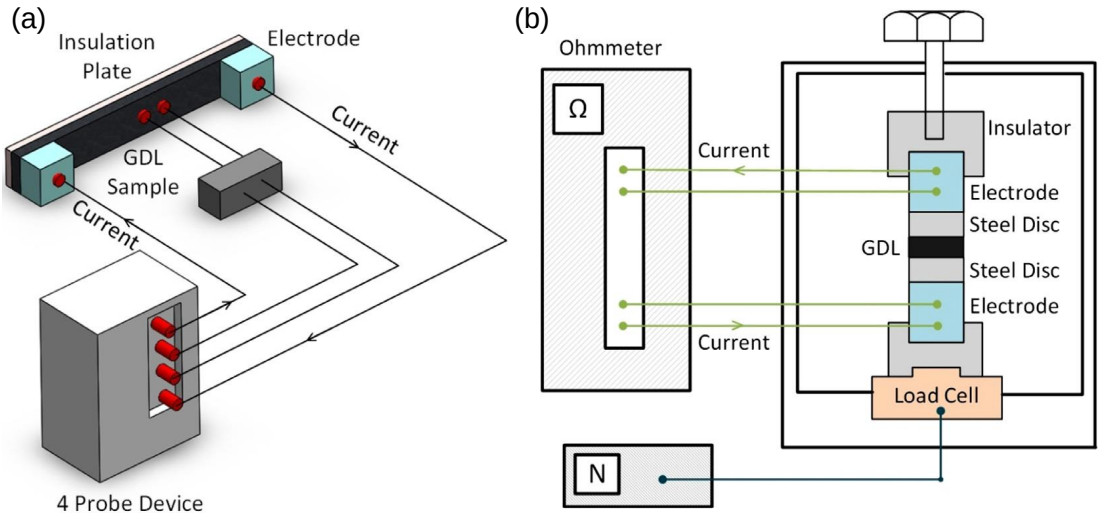

Figure 1.2: Schematic of the experimental setup for measuring electrical conductivity in (a) in- and (b) through-plane direction [24].

Thermal conductivity measurement methods

The exothermic reaction of PEMFCs, combined with irreversibilities and losses generate heat that distributes within different constituent of the cell. The temperature gradient across the cell impacts the transport mechanism, relative humidity and the durability of the cell. An active cooling system combined with optimized heat management is necessary to achieve a highly efficient cell design. The heat management strategy requires detailed information on the constituents' thermal conductivity properties and interfacial thermal conductivity between components similar to electrical conductivity. Among different components, the GDL plays a significant role since it

impacts many of the losses within a cell.

The (1) highly anisotropic porous structure of GDL combined with (2) multiphase flow, (3) hydrophobic treatment, and (4) effect of compression leads to an elaborate analysis of evaluating thermal conductivity of the GDL. As a result, the effective thermal conductivity is a more accurate term since each parameter, as mentioned earlier, has a significant effect on assessing this parameter. First, methods to obtain thermal conductivity in through-plane will be reviewed, and then we move on to the in-plane direction.

Through-plane: A uniform one-dimensional heat flux must be generated in the through-plane direction to measure the thermal conductivity of the GDL. A high conductivity rod with known thermal conductivity property is connected to the top hot plate and three thermocouples are located along the rod's length with the same interval. The same architecture is in place in contact with the cold plate. This guarded heat flux meter is compatible with the ASTM standard. Steady state conditions are considered to be attained when the temperature at each point remains constant within ± 0.5°C [25]. Following Fourier thermal conductivity formula, from the top rod, the heat flux is evaluated by:

$$Q = -k(T)A_r \frac{dT}{dx} \tag{1.3}$$

where Q is heat flux, $k(T)$ is the thermal conductivity and A_r is the cross-sectional area, and $\frac{dT}{dx}$ is the temperature gradient. Then, the temperature differences between the top and bottom sample (i.e. GDL) obtained from the thermocouples will be divided by heat flux to get the thermal resistance following the formula:

$$R_t = \frac{\Delta T_s}{Q} \tag{1.4}$$

where R_t includes thermal resistance and two contact thermal resistances between the top and bottom plate in contact with the GDL. Thermal resistance and thermal contact resistance both are functions of the compression pressure. To exclude the contact resistance, stacking several samples of GDLs results with thermal resistance vs. the number of layers in which the intercepting line gives the contact resistance (similar to electrical conductivity measurement) [25]. As mentioned earlier, the GDL experiences water saturation that has a direct impact on the thermal conductivity estimation. Xu et al. artificially soaked the GDL sample and performed the test to evaluate the effect of water saturation on the thermal conductivity. However, the

study did not provide the level of saturation, which can be investigated in future research [26].

The outcome of extensive research indicates that compression increases the through-plane thermal conductivity for GDLs. However, hydrophobic coating higher than 30 wt% reduces the thermal conductivity by hindering fibre to fibre connection in GDLs [27]. Future work investigating optimum hydrophobic treatment for thermal conductivity is needed to provide detailed data about the effect of hydrophobic treatment vs through-plane thermal conductivity.

In-plane: Determination of in-plane thermal conductivity needs a more complex setup. For steady-state thermal conductivity measurement, there are two methods reported in the literature. Sadeghi et al. [28] developed a novel approach to determine the in-plane thermal conductivity by generating constant flux travelling in the in-plane direction of GDL. The second technique, which has some advantages over the first method, is parallel thermal conductance. The parallel thermal conductance method brings high accuracy with faster data collections. In this method, as shown in Figure 1.3, low conductivity material places parallel with the GDL sample [29]. A direct current supply generates a constant temperature in the heat source. The conductivity of the low conductive material is measured without placing a GDL between two thermocouples. The thermal resistance is:

$$R_0 = \frac{T_h - T_c}{IV} \tag{1.5}$$

T_h and T_c are temperatures in hot and cold locations captured by thermocouples, respectively. I and V are current and voltage for generating constant temperature. The captured resistance consists of conductivity of low conductive material and apparatus (thermocouples, wiring) and radiation of surrounding (i.e. R_0). The test is performed in a vacuum chamber to mitigate the effect of natural convection (similar to through-plane measurement). The test is repeated with GDL in place, and the new resistance is captured, following the parallel formula as:

$$\frac{1}{R} = \frac{1}{R_0} + \frac{1}{R_s} \tag{1.6}$$

where R is the thermal resistance from the second experiment, and R_s is the thermal

resistance between two edges. The in-plane thermal conductivity is calculated as:

$$k_{GDL,in} = \frac{L}{Wt}(\frac{1}{R} - \frac{1}{R_s}) \tag{1.7}$$

L, W and t are length, width and thickness of the GDL in the test setup. The reviewed techniques managed to obtain in-plane thermal conductivity. However, the effect of compression and saturation on the in-plane thermal conductivity has yet to be analyzed.

The in-plane thermal conductivity (e.g. TGP-H-120 5 wt% PTFE $= 17.39\ Wm^{-1}K^{-1}$) is by order of 10 higher than the through-plane conductivity (e.g. TGP-H-120 5 wt% PTFE $= 1.62\ Wm^{-1}K^{-1}$), which indicates the bottle-neck is in the through-plane direction [24]. Furthermore, hydrophobic treatment increases the thermal conductivity by filling voids and replacing it with polymers, which has a higher conductivity than air. Quantifying the effect of hydrophobic treatment vs. in-plane thermal conductivity should be performed to determine the optimal hydrophobic treatment for thermal conductivity.

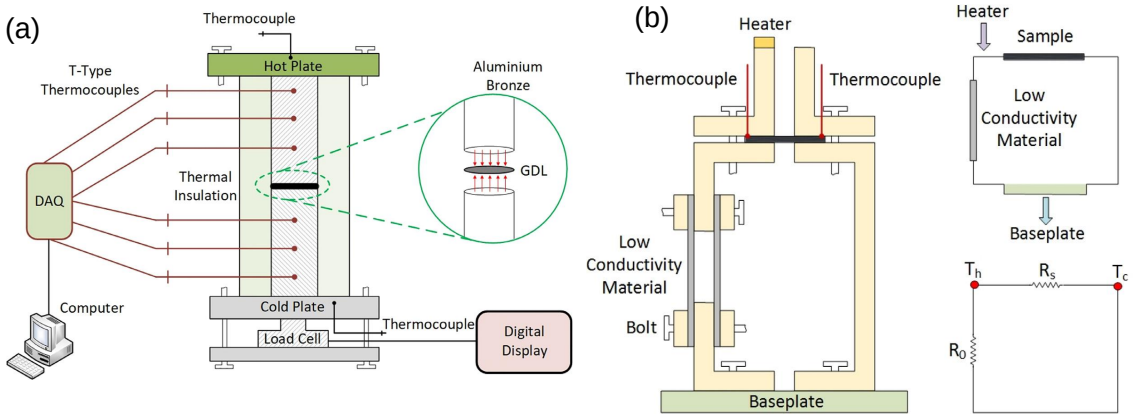

Figure 1.3: Schematic of experimental setup for measuring thermal conductivity in (a) through-plane and (b) in-plane direction [24].

1.2.3 Strategies for Enhanced Water Management

Effective water management in PEMFCs is necessary to obtain optimal performance across a range of current densities and environmental conditions. Water in operating fuel cells is a by-product of electrochemical reactions in the cell and is also introduced by the humidified inlet gases. At high current densities and when water and heat management are inadequate, water vapour can condense and form liquid water in the porous electrode blocking the pathways of the reactants to the CL, and causing mass transport limitations [14, 17]. The excess water has other deleterious effects, such as inhomogeneous current density, membrane swelling, and delamination of PEMFCs components in freeze/thaw processes [30]. On the other hand, membrane hydration is an important factor in optimal performance since a dehydrated membrane results in high ionic resistance and performance degradation [13, 17].

The GDL serves several important functions, including (1) reactant and product permeability, (2) electrical conductivity, (3) thermal conductivity, and (4) mechanical support for the membrane electrode assembly (MEA) [9]. This layer is a prime candidate to employ different strategies for water management. These strategies fall into three main categories (1) physical modifications; (2) addition of external components; and (3) chemical modifications. Other options have also been explored, such as perforated metallic plates or metallic porous substrate instead of fibrous carbon-based materials [31].

Physical modification

Modifications to enhance water transport have been mainly directed at fibrous carbon-based GDLs, which are widely used in commercial fuel cells. Gerteisen et al. [1] generated through-plane holes with 80 µm diameter in a carbon paper GDL. These holes were located under the channel of the flow field and result in improved of water transport dynamics and cell performance, with gain in limiting current density of the cell under humidified conditions (Figure 1.4(a)-(c)). The through-plane pores are generated by either electric discharge machining, micro-drilling, or laser perforation. The process of perforating pores melts the binder in GDLs and can close the pores; this can be a severe problem for samples with high binder loading. In addition, the laser perforation and the electric discharge machining alter the hydrophobic surface of the pores into hydrophilic surfaces. Okuhata et al. [32] investigated differences between electric discharge machining and micro-drilling for generating perforated holes and

achieved better performance with micro-drilling, which maintains hydrophobicity of perforated walls. Th r idea of perforated pores has been studied with samples with MPLs [33, 34, 2]. Manahan et al. [34, 2] made 100 to 300 µm pores with and without hydrophilic heat-affected zones (HAZs) (Figure 1.4(d) and (e)). The HAZs are hydrophilic and preferential pathways for water removal. The results indicated that at 75% RH, the GDL with 300 µm and HAZs performed better; however, for the over-humidified condition (i.e. in cold start-up) the fuel cell performance dropped due to water flooding. Physical modifications have gained much attention in the literature as they are relatively easy to implement; however, the effectiveness of this approach is limited to specific running conditions of the cell (e.g. specific RH and temperature conditions).

Another promising approach is the development of GDL with graded porosity from the CL to the flow channel. The idea is to decrease the capillary pressure in the through-plane direction and speed up water removal from the reaction zone into the channel. Numerical studies have been carried out to determine the optimal porosity distribution. The results suggest a linear porosity distribution from CL to the flow channel. However, achieving such morphologies with carbon-based GDLs adds extra difficulties in the manufacturing process [35]. Other innovative approaches, such as electrospinning [36] or functionally graded materials in powder metallurgy, are promising avenues to pursue [35].

Addition of external components

Another approach to improve water management is adding an external layer. One of the passive methods consists of adding a conductive wicking layer between the GDL and the flow field. This layer prevents flooding under broad operational conditions for air-breathing PEMFCs (Figure 1.4 (g)) [3]. The wicking layer was combined with an electroosmotic (EO) pump to actively remove excess water from the cell. The pump required less than 2% of the fuel cell power, but eliminated the cathode flooding and helps improve stability and water management (Figure 1.4(h)-(i)). The application of this system was shown for a small-scale fuel cell (less than 5W) [4]. However, it adds an extra layer to the MEA and complexity to the system, and its implementation has not been demonstrated in fuel cells with higher power outputs.

Chemical modifications

As the nature of the process indicates, water transport is a complex phenomenon and requires adaptive solutions for various conditions. A number of studies have explored chemically altering hydrophobicity of the GDL and pattering hydrophilic/hydrophobic [37]. Paul Scherrer Institute researchers developed a novel method for generating hydrophilic/hydrophobic channels on off-the-shelves GDLs with varying width sizes from 100 µm up to 1000 µm. Figure 1.4(I) shows a schematic of the process. A commercial GDL (i.e. Toray TGP-H-060) was first dip-coated with an FEP solution (due to higher water-repelling quality in comparison with PTFE); a mask with pre-defined patterned was then placed on the coated sample and exposed to an electron beam. Subsequently, the GDL was immersed into hydrophilic monomer, N-vinyl formamide (NVF), to graft pNVF to FEP. This process reduces the contact angle (CA) from 105° to 20° and effectively alteres the region from hydrophobic to hydrophilic (Figure 1.4(k)). EDS analysis indicated the presence of pNVF in the area exposed to irradiation on both sides of the GDL (Figure 1.4(m)). The effect of capillary pressure on a different area of the modified GDLs was observed with neutron radiography and shows that hydrophilic channels need a lower capillary pressure (10 mbar) compares to hydrophobic channels (40 mbar). An in-situ fuel cell with GDLs having 500 µm wide hydrophilic channels and 950 µm wide hydrophobic channels shows a considerable improvement in fuel cell performance(Figure 1.4(n)) [5]. The successful demonstration of the novel GDLs was thoroughly studied from synthetic approach [38], ex-situ water transport analysis [18] and in-situ fuel cell testing [39]. However, a challenge is the degradation of the hydrophobic/hydrophilic pattern at the high temperature required for MPL sintering. The authors suggest alternative MPL sintering approaches such as local heating using infrared. Another challenge is that the method is not suitable for nonuniform porosity GDLs.

Chemically altering hydrophobicity of MPL either by using different hydrophobic polymers in MPL materials (ex. perfluoroalkoxy (PFA) and fluorinated polyurethane based on perfluropolyesther (PFPE) blocks) or adding hydrophobic agents or multiple layers of hydrophilic-hydrophobic structure have also been investigated in the literature and are discussed in Ref [35].

1.2.4 In-situ RH and Temperature Measurement

Fuel cell operating parameters such as voltage, current, inlet and outlet RH and temperature, and stoichiometry are parameters to control fuel cell performance and avoid water flooding. However, these properties are averaged out over the entire system and do not necessarily represent local conditions as they are typically non-uniform. Nonuniform conditions accelerate the degradation of the cell and, ultimately, cause performance drop. In-situ measurement of local conditions (e.g. temperature and RH) provides detailed information on RH and temperature distribution in a cell, which facilitates implementation of effective water management strategies for fuel cell stacks. Furthermore, obtaining local parameters provides pathways for adaptive smart porous materials for controlling reactants and product transport within the cell [40]. Here, we briefly review diagnostics techniques for measuring temperature and RH locally within fuel cells.

The local temperature has a direct effect on a reaction rate, membrane conductivity and, additionally, the transport properties of the membrane. RH is the second key control parameter. This parameter is closely coupled with temperature and determines membrane conductivity and water balance in PEMFCs. In addition, the membrane thickness is proportional to the RH of the cell, and non-uniform distribution of RH accelerates the mechanical degradation of the membrane. The challenge is to locally measure these parameters as closely as possible to the reaction zone with minimal impact on the performance of the cell.

Commercial probes (ex. thermocouples and capacitive RH sensors), Micro-electro-mechanical-systems (MEMS) device and optical sensors (e.g. fibre optics) are commonly used tools for monitoring local temperature and RHs. These sensors are placed on either the flow field or the membrane or between constituent layers (i.e. membrane and CL or CL and GDL or flow field and GDL). Zhang et al. [41] placed thermocouples between GDL and CL in the cathode where they were distributed from the inlet to the outlet of the cell and captured the local temperature at different operating conditions. The results show that there is a gap between local temperature and back-plate temperature (i.e. nominal test temperature), and also, the local temperature and local current densities are well correlated. The sensors, however, covered valuable areas of the CL. Pei et al. [42] designed an experimental setup to measure temperature distribution in a stack of cells. Thermocouples were placed in the cathode side of the flow field in contact with the GDL. It shows that not only is there a temperature

distribution in each cell, but also, temperatures are varied in the stack and shows parabola temperature distribution along with the stack. Placing thermocouples on the outside of the flow field also shows non-homogenous temperature distributions within a single cell [43, 44]. Discssion of use of commercial probes to measure RH is limited in the literature. One successful demonstration uses different capacitive RH sensors in the flow field of both anode and cathode for a single cell. RH gradient formed from the inlet to the outlet for both anode and cathode side along the channel. Although the commercial probes provide detailed temperature and RH maps, their footprint is considerable, and most of them are located at a the distance from the reaction zones and require modification of flow field design for the stack of PEMFCs.

MEMS fabrication techniques benefit from a small footprint, monitoring different parameters on a single chip and ability to mount on surfaces. A resistance temperature detector (RTD) in a serpentine pattern with a capacitive humidity sensor in the interdigitated structure was fabricated and located on the flow field of PEMFCs [45]. In a subsequent study, five sensors in one MEMS device were combined to obtain local temperature, voltage, pressure, flow rate and current and located on the flow field of cathode [46]. Embedding sensors on MEA is attractive due to collecting information in a crucial area. Lee et al. [47] fabricated a MEMS device with a footprint of 400 µm × 400 µm with the thickness of the 2 µm and hot-pressed it on the membrane surface. It shows more than 5 °C difference existed between the MEA and a bipolar plate surface. However, this diagnostic technique costs in performance loss due to CL's coverage and reducing the active area of the CL.

Employing optical sensors is another promising avenue for in-situ diagnostic in PEMFCs. Tunable diode laser absorption spectroscopy [48], phosphorescence-based sensors [49, 50], and fibre grating sensors(FBG) [51, 52, 53] have been utilized in the literature. Inman et al. [50] employed the principal of phosphor thermometry to measure the surface temperature of the a GDL. Phosphor materials were applied on the surface of the GDL, and an optical fibre was located on the channel to provide optical path from the phosphor to the photodetector. That allowed to monitor temperature on the surface of the GDL locally at different operating conditions. The implantation of the sensor did not have a negative impact on cell performance. David et al. [52] utilized FBG sensors in the channel of PEMFCs and obtained temperature and RH simultaneously in the flow field with relatively fast response to RH changes(in order of 10 s). These sensors are mainly suitable for monitoring environmental conditions in the flow field and also need a significant change in the flow field's design. In addition,

the sensors are delicate and fragile. The more detailed information about the fibre optic sensors are provided in Refs [54, 53].

1.2.5 Fibre-based Temperature and Humidity Sensors

Conventional techniques to measure the local properties in PEMFCs either require significant design changes or cause a drop in performance. To address these drawbacks, embedding sensors that can fit within the GDL structure is essential. A promising possibility is use of sensitive fabrics that can be added to carbon cloth GDL to work as embedded sensors without compromising the performance. Flexible fibre-like sensors that can be weaved or sewn on to carbon cloth resulting in advanced sensing textiles have shown some promise in wearable technology and advanced health system monitoring.

E-textiles that combine electronics with well-established textile technology enable the development of smart fabrics that can sense and respond to external stimuli such as strain [55], temperature and humidity [56]. This section reviews the development and fabrication of fibre-like sensors for measuring RH and temperature.

Fabrication process

There are three major routes to make functional textiles: (1) fibre making, (2) coating/printing and (3) embedding microelectronics within textiles. The backbone of the fibre making and coating/printing process is on blending nanomaterials, and then later takes advantage of high precision microelectronics for developing smart textiles [57].

Fibre-making; in this process functional materials are added into precursors to form fibres with methods such as wet-spinning and electrospinning. The fibre-making process allows homogenous modification with embedding functional materials in a sub-micrometre structure and gives the ability to a more detailed design of the internal structure. However, coarse fibre quality and low durability are among the important challenges that need to be overcome for scaling up such methods.

Coating and Printing; this scalable and straightforward process forms an electrically conductive layer on the surface of fibres, yarn or textile, thereby transforming them into functional materials. The benefits are low cost and the ability to mass-produce coated textiles by existing production processes. However, this process dose not allow embedding of functional materials in the inner layer of the fibre struc-

ture. Dip-coating, screen printing and inkjet printing are main approaches to form a conductive layer on fibre and textiles.

Embedding electronics within textiles; this method takes advantage of existing technology in microelectronics with good accuracy and durability. However, the procedure has high costs and lower flexibility.

Fibre-based humidity sensors

Zhou et al. [58] developed a wet-spun single-wall carbon nanotube (SWCNTs)-polyvinyl alcohol (PVA) filament that shows a resistive response to RH changes. The PVA swells by exposing it to humidity and interrupting the connections between SWCNTs within the structure of the fibre. The resistance of the thread has a quadratic response when exposed to increasing RH. The developed filament can detect the humidity changes between 60% to 100%. In 2008, Shim et al. dip-coated a cotton thread into SWCNTs suspension for detecting albumin, a protein in the blood. Interestingly, they found that the CNT-coated cotton thread is responsive to humidity changes [59].

Using MEMS fabrication techniques such as chemical vapour deposition (CVD) or vacuum physical vapour deposition (PVD) to deposit graphene and graphene oxide has been used to develop thin-film sensors for applications such as electronic skin [60, 61]. Comprehensive studies addressing the principles, mechanisms and fabrication technologies for humidity sensors are available in Refs [61, 62]. The developed MEMS device then can be blended into textiles for monitoring humidity [63].

Fibre-based temperature sensors

One of the simplest designs is embedding a metallic wire within textile substrates for temperature monitoring. Li et al. sewed platinum metal wire with a diameter of 20 µm on a piece of cotton fabrics and measured the temperature of the substrates [64]. The wire shows a linear increase in resistance by increasing temperature (0.0039 $\Delta R/R_0\%^{\circ}C^{-1}$). A linear response accompanied by stability and a wide temperature range are favourable for metallic wires. However, the rigidity and low sensitivity restrict the application of such wires in many wearable systems. Furthermore, it is not suitable for conductive substrates such as carbon cloth materials.

Coating and printing nanomaterials ink on textiles, fibres, or threads is another promising approach for developing a textile-based temperature sensor. Rosace et al.

[65] coated MWCNT-polyacrylic nanocomposite on cotton fabrics and achieved a linear resistive sensitivity of 8 $\Delta R/R_0\%K^{-1}$, but the coated fabric shows a response to humidity changes, which limits the application of such coating. CNT-coated cotton thread via a dip-coating process showed a linear increase in resistance of the coated thread by increasing temperature [66]. Batch-to-batch steps were used to coat polypyrrole on commodity threads (i.e. cotton, nylon and polyester) with stable electrical conductivity under bending and strain cycles show a linear temperature response for the coated fabrics. PEDOT:PSS polymer dyed on cotton fabrics and achieve a linearly negative temperature coefficient from -50 °C to 80 °C [67]. Although many of the mentioned papers show promising results to detect temperature, poor selectivity in coating and printing process is a formidable challenge to overcome.

Similar to RH development, MEMS fabrication techniques are utilized to deposit temperature-sensitive materials on a flexible substrate such as PDMS [60] and flexible Kapton [68]. Fixing MEMS devices within textiles by weaving them on the substrate is an approach to measure the temperature of the textile.

1.3 Objectives

The main objectives of this thesis are:

(1) To investigate the effect of hydrophobic coating on water transport and conductivity of the GDLs, Chapter 3.

(2) To develop integrated textiles for water transport and embed RH and temperature diagnostics tool within the textile electrode of PEMFCs, Chapter 4.

(3) To develop thread-based temperature and RH sensors for wearable applications and investigate biocompatibility of these devices, Chapter 5.

1.4 Structure of Thesis

This thesis consists of six chapters. Chapter 1 provides the background and motivations with a detailed introductory literature review. A summary of the key results is presented in Chapter 2. Chapters 3 to 5 present in manuscript format the main contributions of this thesis with relevant background, experiments, and results.

Chapter 3 presents the experimental procedure for evaluating water transport, thermal conductivity and electrical conductivity of carbon cloth GDLs. The effect of

hydrophobic coating (FEP) and compression are evaluated.

Chapter 4 demonstrates the integration of the external threads to facilitate water transport and also monitoring RH and temperature via fibre-like sensors within carbon cloth GDLs. Physical, microstructural and transport properties of the modified GDL were evaluated. The process of fabricating sensors was also explained, and sensor response for PEMFCs working conditions was investigated.

Chapter 5 presents the development of hybrid temperature and humidity sensors for application in wearable biomonitoring. The study investigates the coating process with the variable concentration of CNTs and surfactants. Further, it characterizes the CNT-coated thread response to temperature and relative humidity. Finally, the biocompatibility of the sensors was evaluated.

Chapter 6 summarizes the key findings, contributions and suggestions for future work based on the outcomes of three research studies presented in Chapter 3 to 5.

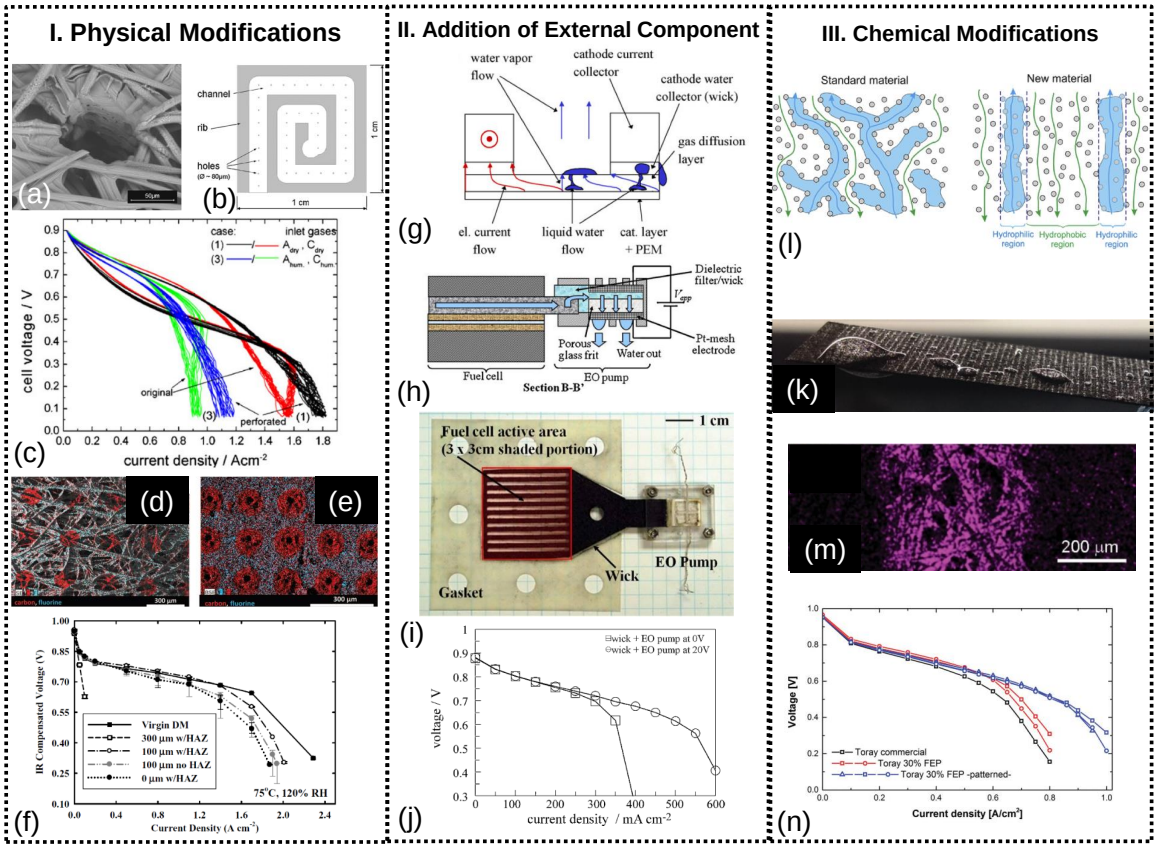

Figure 1.4: **Summary of different water management strategies.** I. Physical Modification; (a) GDL with laser perforated pores, (b) schematic of locations of perforation holes along the flow channel, (c) comparison of fuel cell polarization curve for pristine and perforated GDL [1]. (d) HAZ with perforated pores on the GDL and (e) MPL [2]. (f) Polarization curve under over-humidified conditions showing a pristine sample outperforms a modified sample. [2] II. Addition of External Component; (g) addition of a conductive wicking layer [3], (h) schematic of additional EO pump, (i) MEA with EO pump and (j) fuel cell polarization curve for MEA with and without EO pump [4]. III. Chemical Modifications (l) schematic presentation of water transport in conventional GDL and GDL with hydrophobic and hydrophilic pathways, (a) GDL with hydrophilic/hydrophobic channels, (m) EDS analysis is showing existing hydrophilic polymer (pNVF) on carbon paper GDL and (n) fuel cell polarization curve for MEA with and without a patterned in GDL [5].

Chapter 2

Summary of Key Findings

This chapter summarizes the key results of the three studies undertaken in this dissertation and discussed in detail in Chapters 3 to 5. The first study analyzes the trade-off between hydrophobic coating on water transport and conductivity for carbon cloth GDLs. In the follow up work, we explored the addition of external threads into cloth GDLs by integrating textile sensing for water and thermal management in PEMFCs. The last study focuses on the development of thread-based temperature and humidity sensors with emphasis on application in wearable biomonitoring.

2.1 Woven gas diffusion layer for polymer electrolyte membrane fuel cells: liquid water transport and conductivity trade-offs

Hydrophobic coatings are widely used in the industry to improve water transport in GDLs. The coating alters water transport, thermal conductivity and electrical conductivity of the porous GDL. Previously, the effect of hydrophobic coating on transport properties for non-woven GDLs was studied thoroughly. This study aims to investigate the impact of such coatings on a woven GDL since the structure provides a suitable substrate for adding functional fibres for sensing but is significantly different from the non-woven counterpart.

A test setup was designed to monitor water transport and water pressure in porous structure using upright fluorescent microscopy to track dyed water transport within the porous GDL. Three different hydrophobic coated GDLs (0%, 30 wt% and 55

wt% FEP) were evaluated. The results show that the hydrophobic coating led to better usage of pores within GDLs and water transported in the in-plane directions compared to non-coated GDLs. The through-plane conductivity analysis shows that the electrical conductivity reduces by increasing hydrophobic coating; however, the thermal conductivity has an optimum amount of conductivity with FEP loading.

The key contributions and findings of this study are: (1) a procedure is developed to monitor water transport and capture water pressure in the highly porous structure. (2) FEP loading improves the water transport in woven GDLs and utilizes pores in the in-plane directions more effectively compared to non-coated samples. (3) The electrical conductivity reduces by increasing the hydrophobic coating; however, thermal conductivity increases first (up to 30% FEP loading) and then decreases. (4) There is a trade-off between better water transport and conductivity of GDLs while using the hydrophobic coating.

This section of the thesis is presented in detail in Chapter 3.

2.2 Integrated textile-based sensors for water and thermal management in polymer electrolyte membrane fuel cells

PEMFCs experiences non-uniform water and heat transfer with a gradient of temperature and humidity within the cell. Smart components that can adapt to a variety of dynamic changes are vital criteria to improve the performance and durability of the cells. Generating water transport pathways and combining real-time measurement of temperature and RH distributions witihn a textile GDL allows improvement in performance and paves the routes toward adaptive materials within PEMFCs. This study aims to (1) generate hydrophilic pathways within woven GDLs and investigate the effect of that external hydrophilic threads on transport properties, and (2) develop embedded threaded sensors for monitoring temperature and RH locally in woven GDLs. Hydrophobic threads were sewn on woven GDLs for facilitating water removal. We analyzed the effect of threads on the physical and microstructural properties of GDLs. Our results show that threads embedded well in microstructure of woven GDLs with minimal impact on transport properties. The in-situ fuel cell testing indicates that the GDL with hydrophilic threads has no adverse effect on the performance.

Temperature and RH sensing threads were developed by dip-coating them with CNT ink and sewing them on a woven GDL. The CNT-coated thread shows RH and temperature sensitivity in the working range of PEMFCs. To be able to use these sensors in the fuel cell environment, PDMS was coated on top of the CNT-coated thread to generate an electrical insulating layer and also achieve water vapour transmission for detecting RH. PDMS+CNT-coated thread is responsive to RH changes. FEP coating provides an electrical and vapour insulating layer and also mitigates the RH sensitivity. FEP+CNT-coated thread is solely responsive to temperature. The RH and temperature sensitivity of both threads PDMS+CNT-coated and FEP+CNT-coated threads) were characterized, and an ex-situ experiment shows the workability of such sensors in woven GDLs.

The key contributions and findings of this study are: (1) external hydrophilic threads embedded in woven GDL generated water pathways. (2) Physical, microstructural and transport properties of GDLs with external threads were analyzed and showed minimal impact on GDLs properties. (3) Temperature and RH sensing threads suitable for PEMFCs working conditions were developed and tested in an ex-situ experiment.

Chapter 4 explains in detail this section of the thesis.

2.3 A hybrid thread-based temperature and humidity sensor for continuous health monitoring

In the previous study, thread-based temperature and RH sensors were developed for the working conditions of PEMFCs. The application of these sensors is not limited to diagnostic tools in woven electrodes. These thread-based sensors have prospective use in a wearable biomonitoring system, which works in a lower temperature range (e.g. room temperature). The main objective of the third study is to investigate the use of these sensors in biomedical applications, particularly wound monitoring.

The CNT ink for dip-coating cotton threads is compromised of functionalized multiwalled carbon nanotubes (fMWCNTs) and sodium dodecyl sulfate (SDS) in distilled water. The effect of concentration of each component and the number of dipping on the thread resistance are investigated. Furthermore, the CNT attachment on the cotton filaments is evaluated with SEM imaging. The response to RH and temper-

ature of the CNT-coated thread are further analyzed and shows the responsiveness to both RH and temperature. FEP coating reduces the RH response and shows only temperature sensitivity for CNT+FEP-coated thread. For the proof of concept, the thread-based temperature sensor is combined with a heating thread to control the local temperature within a textile.

Finally, the cytotoxicity response and compatibility of the CNT-coated (i.e. RH sensor) and FEP+CNT-coated (i.e. temperature sensor) threads are evaluated for potential use in smart wound dressing. The analysis shows that the thread-based sensors do not develop a cytotoxic response to cell growth. Furthermore, placing the sensors on healthy mice wounds did not affect the wound healing process in mice.

The key contributions and findings of this study are: (1) dip-coating parameters (i.e. concentration of CNTs, surfactant and number of dipping) are optimized for developing CNT-coated thread. (2) The response of the CNT-coated thread to temperature and humidity is investigated and shows a linear decrease in response to temperature change and quadratic resistance increase to RH changes. (3) FEP coating successfully mitigates the RH sensitivity of the CNT-coated thread and results in solely a thread-based temperature sensor. Combining both CNT-coated and FEP+CNT-coated threads can monitor both temperature and RH in textile substrates. (4) Finally, the cell cytotoxicity and animal results show thread-based sensors are biocompatible for wearable biomonitoring.

Chapter 5 explains in detail this section of the thesis.

Chapter 3

Woven gas diffusion layer for polymer electrolyte membrane fuel cells: liquid water transport and conductivity trade-offs

(Journal of Power Sources, volume 403, 2018, 192-198)

3.1 Abstract

Gas diffusion layers (GDLs) provide pathways for water removal in a PEM Fuel Cell. Woven GDLs, have shown higher capability to contain water and improve performance under humid conditions compared to non-woven GDLs. In this work, we investigate water transport, distribution and location of breakthrough in woven GDLs using fluorescent microscopy. GDLs with no coating, 30, and 55 wt% fluorinate ethylene propylene (FEP) were investigated. FEP increases hydrophobicity and affects thermal and electrical conductivities. The results show that the FEP-treated GDLs have higher breakthrough pressures and water contact angles than non-treated GDLs. For untreated samples, water breakthrough occurs in non-compressed regions; whereas, for FEP-treated samples emergence occurs in the compressed regions. Furthermore, water was observed to first cover visible pores inside the GDLs prior to breakthrough. Increasing FEP loading promotes the propagation of water inside the GDLs. Thermal conductivity is found to improve with FEP coating and attains a maximum at 30 wt%

FEP loading, whereas electrical conductivity decreases with increasing FEP loading. This analysis shows more pores are engaged in water transport with higher FEP loading. Implementation of woven GDLs in fuel cell design requires a balancing of the water and heat transport benefits with the reduced electrical conductivity.

Keywords: Woven Gas Diffusion Layers, Water Breakthrough, Fluorescent Microscopy, Thermal conductivity, Electrical Conductivity

3.2 Introduction

The gas diffusion layer (GDL) plays a central role in performance of polymer electrolyte membrane fuel cells (PEMFCs) [9]. The GDL facilitates transport of reactants from the flow channels to the catalyst layer and contributes to the transport of electrons and heat from the membrane electrode assembly (MEA), where the electrochemical reactions occur. Additionally, the GDL helps control the level of moisture in a fuel cell. Proper water management ensures that by-product water is removed from the catalyst layer to prevent flooding while maintaining the catalyst layer and MEA hydrated at the same time [15].

The GDL is a porous structure that is fabricated either by weaving carbon fibers into a carbon cloth or randomly distributing carbon fibers to form a non-woven carbon paper. Carbon fibers are mostly made of polyacrylonitrile (PAN) using a solvent spinning process [9]. Spun PAN yarns, used to make carbon cloth, are produced through the Worsted process, where yarns are generated and wrapped around a bobbin for weaving. The woven carbon fiber is then carbonized at a minimum temperature of 1600 °C (often under vacuum) [9]. This manufacturing process leads to a more flexible GDL structure. Non-woven GDLs are manufactured using the papermaking technology followed by sintering [9]. This process leads to a different microstructure for the non-woven GDLs than their woven counterparts. The pore sizes in woven GDLs vary in a wide range from 2 µm to 100 µm, whereas pore sizes in non-woven GDLs range from 10 µm to 30 µm. The wide range of pore size distribution in the woven GDLs is due to the multiscale microstructure of the constituent yarns that are formed from packed fine fibrils with large pores located between the yarns [69, 70]. Moreover, woven GDLs have lower porosity and less tortuous structure compared to non-woven GDLs [69]. In addition, the in-plane porosity distribution in woven GDLs has a sinusoidal shape, which varies between 80 to 90%, whereas non-woven GDLs porosity distribution is more random. GDLs are commonly treated with hydrophobic

polymers such as polytetrafluoroethylene (PTFE) or fluorinated ethylene propylene (FEP) [5] to improve the hydrophobicity of the GDLs using dipping, spraying, or brushing methods. Another process that improves the performance of the GDL is applying a thin microporous layer (MPL), to the side which is in contact with the catalyst layer (CL), to facilitate the wicking of liquid water from the CL to the GDL. MPLs have a pore size distribution much smaller than GDLs, from $\sim$ 100 to 500 nm [9].

Experimental studies to characterize GDLs have been conducted (1) to understand transport properties, such as permeability, diffusivity, breakthrough pressure, electrical conductivity and thermal conductivity; and (2) to analyze the microstructure, including bulk porosity, pore size distribution, and porosity distribution. One of the key properties of GDLs is water breakthrough. Breakthrough analysis [71, 72, 73, 16] provides information about the required pressure to overcome the capillary force and also the location of the water breakthrough in GDLs. Benziger et al. [71] investigated water breakthrough pressure for woven and non-woven GDLs without an MPL and showed that woven GDLs have a lower breakthrough pressure ($\sim$2 kPa) compared to non-woven GDLs (Toray samples $\sim$7 kPa). The lower breakthrough pressure of woven samples is due to larger pores located between yarns of the woven GDLs. Furthermore, increasing the PTFE loading of the GDL slightly increases the breakthrough pressure. Lu et al. [73] investigated non-woven GDLs with and without MPL (SGL 25BA and SGL 25BC). SGL samples are more porous compared to Toray samples and have larger pores and porosity values [74]. A breakthrough pressure of 1.7 kPa was reported for GDLs without MPL and 6.7 kPa for GDLs with MPL [73]. This is due to the smaller pores of the MPL, which are expected to increase the breakthrough pressure.

Visualization of water breakthrough in GDLs has been studied with different imaging techniques. Two main techniques are X-ray microtomography and fluorescent microscopy. Fluckiger et al. [16] performed X-ray tomography imaging of water breakthrough on non-woven GDLs to observe their water content. The scan time was as low as 5 min with sample size of 2.5 mm in diameter. This study showed the saturation curve in different water intrusion pressure. In 2015, Weber et al. [21] designed a new test setup to replicate the land and channel in the flow field in order to observe the water saturation in GDLs. The scan time was about 8 min with a sample size of 3.2 mm in diameter. Although X-ray microtomography shows high resolution and strong ability to characterize GDLs and interfaces in MEAs (e.g., between GDL and

MPL [74], and between MPL and CL [14]), the small sample size and low temporal resolution were challenges for the breakthrough analysis. However, the recent studies try to improve the 3D µCT in sub second, Eller et al. showed the scan time can reduce to 3.2 s with 1% false water detection [20]. However, fluorescent microscopy with high temporal and spatial resolution allows better tracking of the emergence of water. The challenges with optical fluorescent microscopy are the depth of field, which does not allow to observe the whole structure of GDLs, and sample holders should be modified to provide access of light to the GDLs structure. Litster et al. [14] visualized water transport through the thickness of non-woven GDLs and found the location of the breakthrough on the surface. Bazylak et al. [15] investigated the effect of compression on the location of the breakthrough in non-woven GDLs and showed that compression damages the PTFE and fiber structure and creates preferential pathways for water removal in the compressed areas.

Previous studies mainly characterized non-woven GDLs. However, a comprehensive study to understand water transport in woven GDLs is warranted since these GDLs have a higher capacity to keep water compared to non-woven GDLs (cf. [75]). The present study aims to investigate water transport in woven GDLs at the microstructure level. For this purpose, carbon cloth GDLs with three different FEP loadings (0, 30 wt% and 55 wt%) were used to visualize water transport. The study reveals why woven GDLs have a higher capacity to keep water inside compared to non-woven GDLs, and documents the associated changes in thermal and electrical conductivity.

3.3 Experimental

3.3.1 Preface

The experimental part of this chapter was performed as follow: I was responsible for performing the water transport experiments, data analysis and writing the article. Dr. Mohammad Ahadi performed electrical conductivity and thermal conductivity testing at Ballard Power Systems.

3.3.2 GDL

In this study, a woven GDL, Avcarb 1071 HCB (from Fuelcell Earth), was used. This woven GDL has a thickness of 350 µm and porosity of 65%. FEP solution (Teflon FEPD 121 Fluoroploymer Dispersion) was used to treat the AvCarb GDLs with 30 and 55 wt% FEP loadings. GDLs were dipped into the solution for 1 min and then placed on needle-point holders. The holders were kept in the vacuum oven at room temperature for an hour; the temperature was then increased to 100 °C for one additional hour. This process allowed evaporation of water and other solvents from the GDLs. To evaporate the surfactant, the GDLs were kept in a muffle oven for 50 min while the oven temperature was ramping up to reach 260 °C, and then for an additional 10 min at a constant 260 °C. To sinter the polymer, the temperature was ramped up to 280 °C over 20 min and kept at 280 °C for 20 min (also see [5]).

3.3.3 Visualization and Breakthrough Pressure

The apparatus to measure the breakthrough pressure and perform fluorescence microscopy to visualize water transport is described below. A dilute water solution of 1 millimolar rhodamine B (excitation: emission 540 nm: 625 nm) was prepared to trace water transport in the plane of the GDLs. Since this solution was dilute, dying the water had negligible effect on the properties of water (compared to pure water).

Apparatus

Samples were placed in an assembly and water was injected with a syringe pump at a rate of 0.02 $ml.min^{-1}$. The clamping device has a top plate made from Plexiglas to visualize water, and it has a small hole (with diameter of 5 mm) for water removal. The O-ring diameter is 9 mm and the area between O-ring and open hole is under pressure. The test performed in isothermal at room temperature. An upright fluorescent microscope (DP 73 Olympus BX51), with CY3 filter and 2X objective having a numerical aperture of 0.06, was used in this experiment. A schematic of the clamping device and microscope is shown in Figure 3.1. Images were all taken in black and white. The sample was illuminated with fiber optic, Figure 3.1(a). The acquisition software was Olympus CellSense. Water pressure was measured with a differential pressure transducer (Honeywell FP2000) connected to a DAQ system. The apparatus to measure the breakthrough pressure and perform fluorescence microscopy to

visualize water transport is described below. A dilute water solution of 1 millimolar rhodamine B (excitation: emission 540 nm: 625 nm) was prepared to trace water transport in the plane of the GDLs. Since this solution was dilute, dying the water had negligible effect on the properties of water (compared to pure water).

Image and Data Acquisition

A cooled CCD (charge-coupled device) camera was used to capture the transient transport of water. The nominal depth of the field, calculated from $d_{field} = \lambda/NA^2$, was found to be 150 µm, allowing signals to reveal inside the porous structure. The depth of field of view for the sample was 100 µm that could cover 7∼8 fibres as well as the space where the water flowed. Intensity of the 8-bit images could be correlated to the height of the water on the surface, using the following formula [14]:

$$\eta = \frac{100\mu m}{255I} \tag{3.1}$$

where η is the observable height and I is the intensity of the image. The field of view was 6.5 mm × 5 mm with a spatial resolution of 4.6 µm. This field of view was large enough to cover many pores (∼ 2 to 100 µm [70]) on the surface. Scanning electron microscopy (SEM; Hitachi S-3500N) and energy dispersive X-ray spectroscopy (EDS; Hitachi S-3500N) were employed to observe microstructure of GDLs with different FEP loadings, and also to deduce distribution of FEP in the GDLs.

3.3.4 Thickness Measurement

The thickness of the GDL samples were measured at different pressures using a custom-made testbed (Thickness Under Compression-Resistivity Under Compression, or TUC_RUC) and protocol described in detail in [76].

3.3.5 Thermal Conductivity Measurement

Thermal conductivities were measured using a guarded heat flux (GHF) testbed, which was custom-made based on ASTM Standard E1530-11 and described in detail in [76, 25, 77]. The procedure for measuring bulk thermal conductivity relies on the measurement of thermal resistances of at least two material samples with different thicknesses and then deconvoluting the bulk and contact thermal resistances by

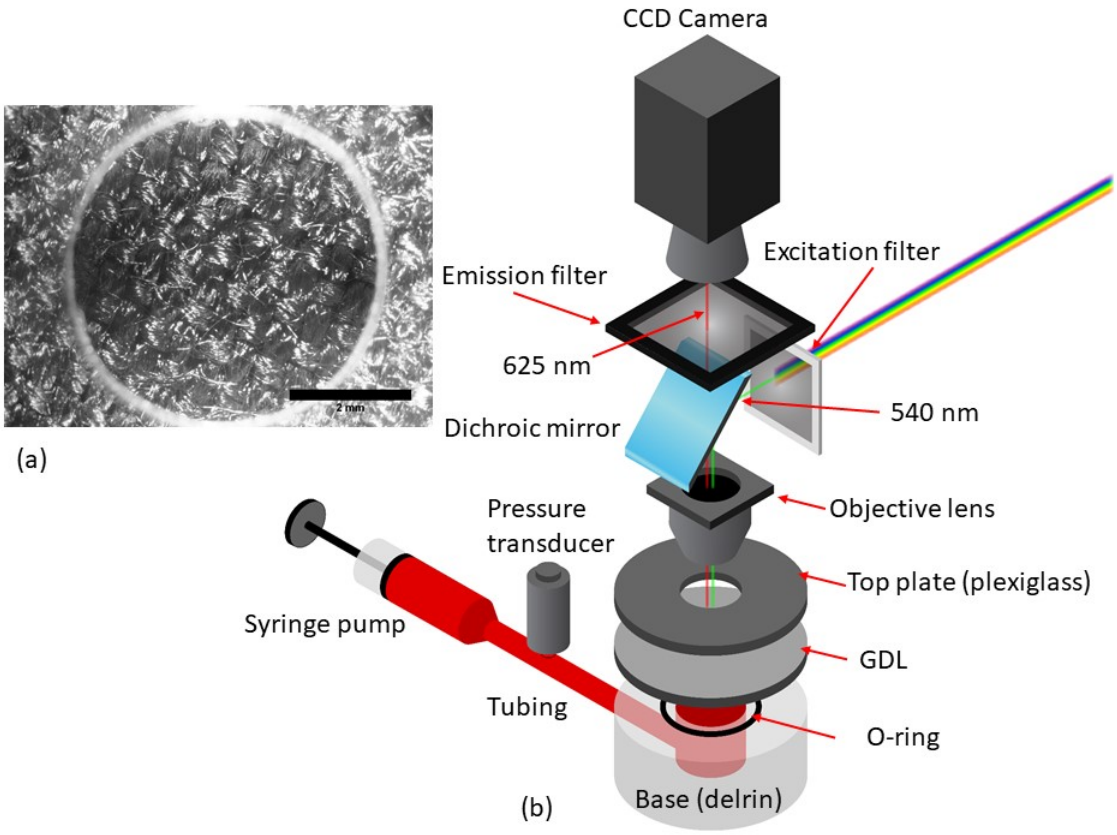

Figure 3.1: (a) Black and white image of woven GDL (scale bar is 2 mm) (b) Schematic of the fluorescent microscopy of GDL.

subtracting the two resistances as follows:

$$k_b = \frac{t_2 - t_1}{(R_2 - R_1)A} \tag{3.2}$$

where R_1 and R_2 are the resistances measured inside the testbed; k_b is the bulk conductivity of the sample, and t_1 and t_2 are the thicknesses of the measured sample. In this study, since only one thickness of GDL was available, different thicknesses were simply made by stacking the material. It should be noted that the total thermal resistance measured by the GHF testbed consists of the bulk resistance and two thermal contact resistances (TCRs) between a sample and the apparatus (the GHF fluxmeters). However, in a stack of several samples, there is an additional TCR between the samples in contact with each other. Therefore, when subtracting resistances of two stacks of samples $(R_2 - R_1)$ in Equation 3.2, the two TCRs between the stacks and

the apparatus (fluxmeters) cancel out, and only the difference in bulk resistances of the samples in the stacks and the TCRs between the samples remain. However, as also shown in refs. [78, 79, 80, 81], TCRs between GDLs in a stack of GDL samples are negligible compared to the bulk resistances of the samples. Therefore, the result of subtraction of resistances in Equation 3.2 (i.e. $R_1 - R_1$) provides an accurate measure of the difference in bulk resistances of the samples in the stacks. This stacking method has been widely used in the literature for measuring different layers of fuel cells, including porous transport layers [78, 79, 80, 81] and catalyst layers [82].

3.3.6 Electrical Conductivity

Measurements of electrical conductivity were performed using a Micro Junior 2 micro ohmmeter (Raytech, USA) comprising four custom-made gold-plated probes. A sample was clamped between the probes, and a clamping pressure of 1500 kPa was applied on the probes. Similarly, to the GIF thermal resistance measurements, the electrical conductivity could be deconvoluted from measurements of at least two sample thicknesses using Equation 3.2. Again, different thicknesses were made simply by stacking.

3.4 Results and Discussion

The clamping device compressed the GDL under an O-ring at a pressure of 1.6 MPa (the pressure film, which is provided by sensor products Inc., was used for the test. The film is sensitive between 400 kPa and 2400 kPa. The photo of the pressure film is available in supplementary information (FigureA.1). This compression is in a same range of compression that GDLs experience in actual fuel cell operation [15]. In-plane and through-plane SEM images of three different woven GDL samples, namely AvCarb 1071 HCB with 0, 30 and 55 wt% FEP loadings, are shown in Figure 3.2. The images show that more FEP material is located on the surface than through the bulk structure of the GDLs. Increasing FEP loading changes the physical properties of the woven GDLs from flexible to more rigid. This may be due to filling the pores between fibers and yarns by FEP, which increases stiffness. The distribution of this polymer within the sample is important since an even distribution of FEP enhances the whole structure's hydrophobicity. The polymeric coating for the samples was investigated using EDS to map fluorine material on the surface and along the in-plane direction

of the GDLs, and the resulting in-plane and through-plane distributions of fluorine and carbon are shown in Figures 3.3 (a) and (b), and the enhanced FEP content with higher loading is clearly illustrated, with a relatively even distribution through the two planes; we note that AvCarb without FEP shows trace amount of fluorine.

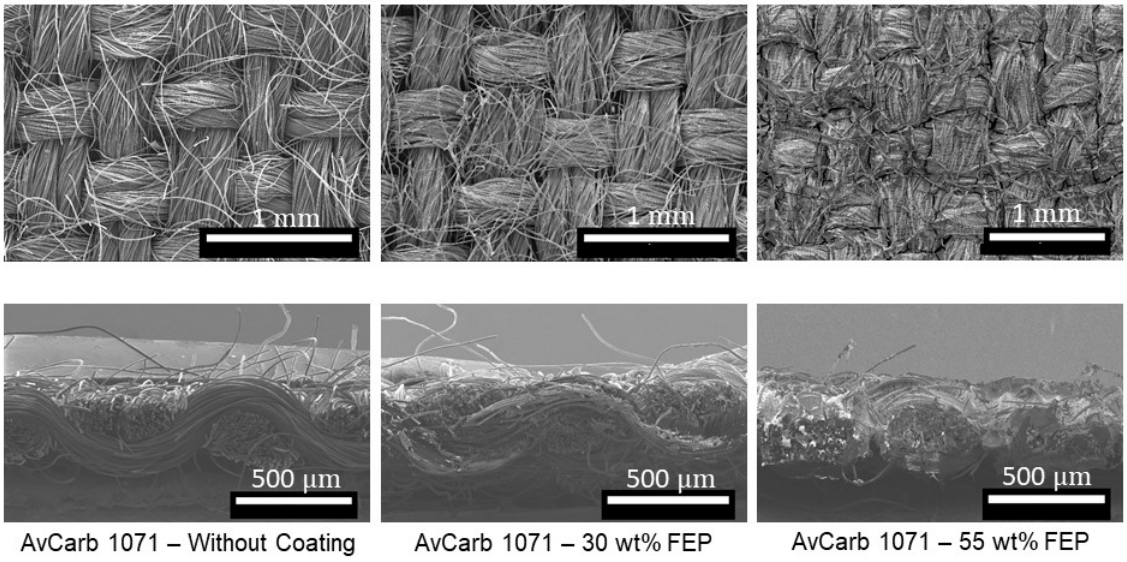

Figure 3.2: SEM images of the in-plane and through-plane of GDLs for different FEP loading (0, 30 wt% and 55 wt% FEP).

EDS analysis can also be used to quantify the material content. Table 3.1 shows weight percentage of each element in Figure 3.3 (a) (in-plane) and (b) (through-plane). There are errors associated for the weight percentage of fluorine and carbon on the surfaces and the cross sections (the detailed report of the quantification analysis are available in the supplementary information FigureA.2). Fluorine accumulates more on the surface, as indicated by the higher percentage of fluorine in the in-plane direction than the through-plane direction. Similar results were reported for non-woven GDLs [11]. The higher content of hydrophobic polymer (PTFE or FEP) on

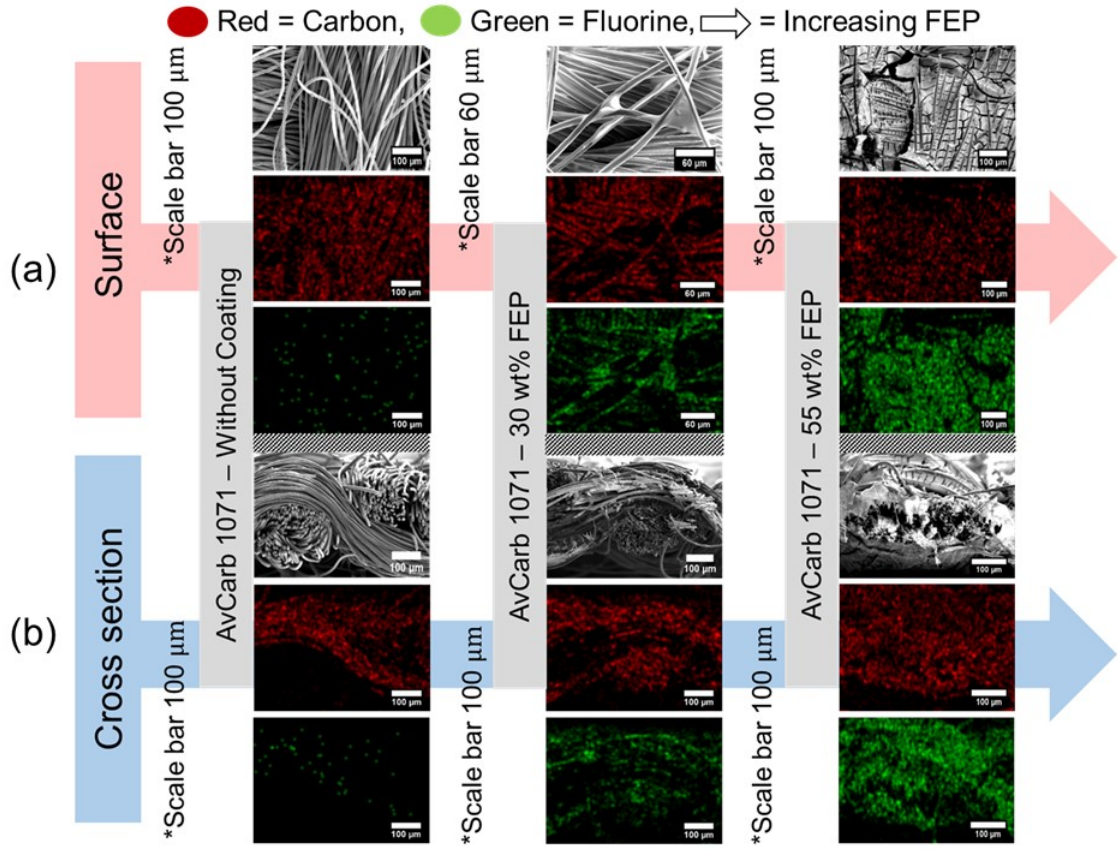

Figure 3.3: EDS analysis mapping (a) in-plane distribution (b) through-plane of carbon (red) and fluorine (green) for different FEP loading sample (0, 30 and 55 wt%).

the surface results in lower porosity near the surface for the treated GDLs. The measured breakthrough pressures for the samples are shown in Figure 3.4(a). Increasing FEP/hydrophobicity of the GDL can reduce the pore sizes and increase the contact angle, see Figure 3.4(b); these factors in turn result in higher breakthrough pressure with higher FEP loading.

Visualizations at the starting time of the breakthrough and following breakthrough are monitored using fluorescent microscopy. Figure 3.5 (a) shows the saturation curve over time, which is obtained by monitoring water emergence from the top plate of clamping device. The transient saturation curve shows the low amount of saturation before the breakthrough. However, after the breakthrough, the saturation increased significantly. For both cases, higher percentage of saturation was observed for modified GDLs compared to the pristine sample. Figure 3.5 (b) shows four instances

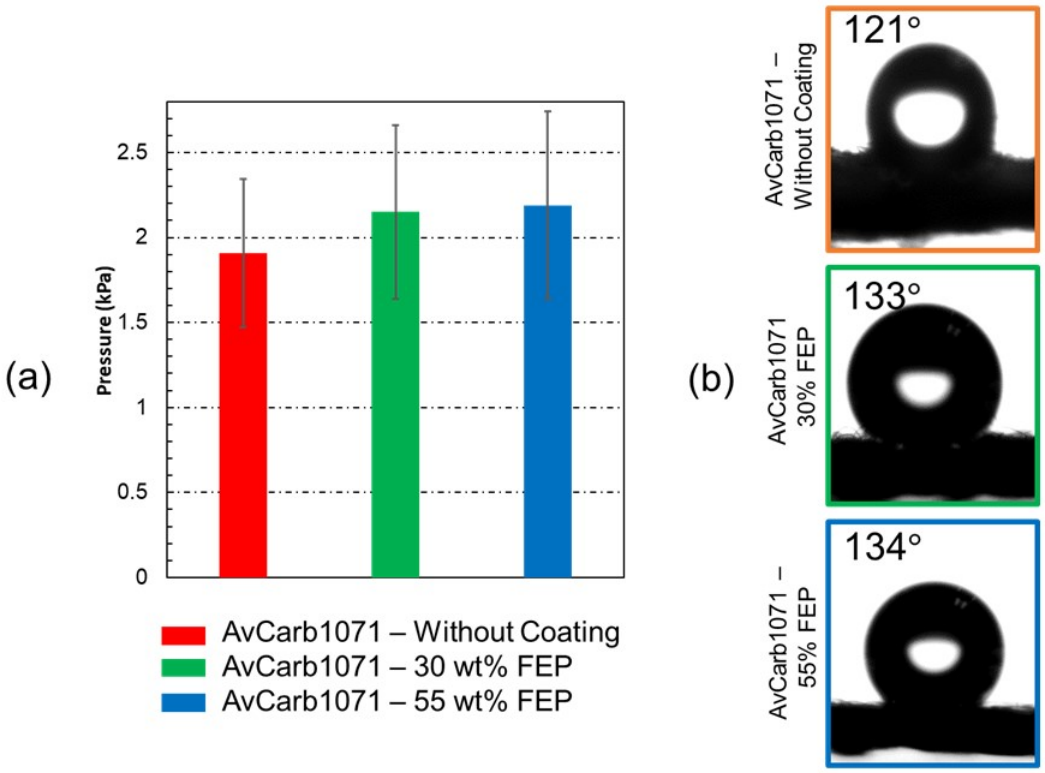

Figure 3.4: (a) Breakthrough pressure and (b) water droplet contact angles of GDLs with different FEP loading (number of sample = 3).

of water transport in the woven GDLs. Water first filled the pores under the open window for all samples as the open window is located on the top of the injection hole. For the 0% FEP sample, breakthrough occurred in the circular open window, and water covered the surface. However, samples with 30 and 55 wt% FEP followed a different scenario. Water first filled the pores in the circular window and then propagated to other pores in the in-plane direction of the GDLs; finally, breakthrough occurred in the compressed areas, with water covering the surface. The supplementary video of water transport for three different GDLs (without coating, 30 wt% FEP and 55 wt% FEP) can be found in the supplementary information (Figure A.3). To provide reproducibility of this test, the same test was performed on more samples and similar results were obtained, which are available in supplementary information. There are some possible explanations for the differences in water distribution patterns. The water flow experienced higher resistance in the through-plane direction.

Table 3.1: Carbon and fluorine percentage for 0, 30 and 55 wt% FEP loading GDLs.

Materials	In-plane [wt%]		Through-plane[wt%]	
	Carbon	Fluorine	Carbon	Fluorine
AvCarb 1071-Without Coating	99.7	0.3	99.8	0.2
AvCarb 1071-30 wt% FEP	62.2	37.8	65.5	34.5
AvCarb 1071-55 wt% FEP	29.4	70.6	41.9	58.1

As a result, the lower resistance pathways are preferential. The hydrophobicity of the GDLs increases and it affects the breakthrough pressure and contact angles of the modified GDLs (Figure 3.4). More hydrophobic pathways cause more propagation of water towards lower resistance regions. This experiment shows that water moves in the in-plane direction, which might have better pore connectivity and lower tortuosity compared to the through-plane direction. Another hindering fact of water transport in the through-plane direction is the accumulation of more FEP on the surface of GDLs, which causes having the smaller pores near the surface and more pressure requires to overcome this barrier. These aforementioned reasons cause increasing the resistance in the through-plane direction, and consequently, water moves inside the GDL and fills the pores first and then, breaks through in the region under compression.

The intensity of the grayscale image can be correlated to the water height [14]. In Figure 3.6(a), the circular shape is subtracted from the breakthrough image, and the corresponding water height distribution is illustrated in the 3D map. Emergence of water for the 0% FEP sample occurs in the circular windows. However, for the FEP-loaded samples, water covers pores first in the areas under compression, and then emerges from the compressed regions. This is attributed to distortion of the GDL microstructure under compression. Compression can open some pathways for water in FEP-loaded woven GDLs, as was also shown for non-woven GDLs [15]. Figure 3.7 illustrates through-plane water transport for untreated and treated GDLs. Water travels toward the open window and with no lateral movement in untreated samples; however, in the treated samples, water is forced to move laterally first and then emerges on the surface.

The variation of GDL thickness with compression is shown in Figure 3.8 for samples with different FEP loadings; the error bars for these measurements are smaller than the data points and are not shown. The measurements show that the samples swell with increasing FEP treatment due to impregnation of fibers and the filling of

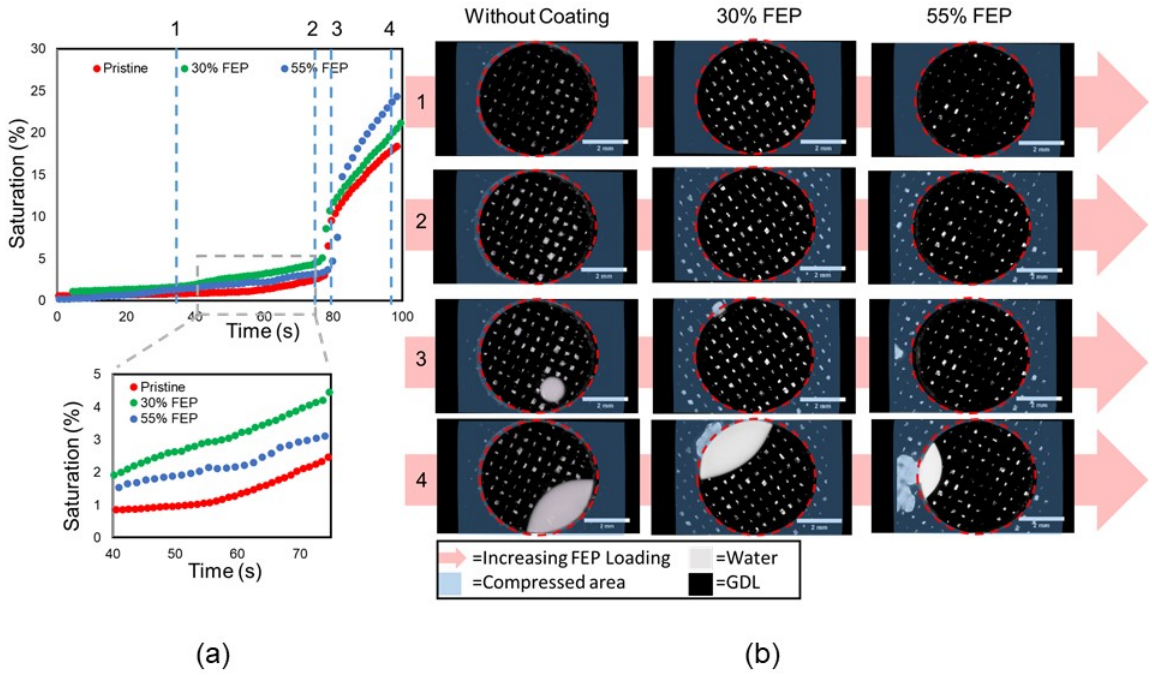

Figure 3.5: (a) saturation over time (b) four instances of water saturation for GDLs without FEP, 30 wt% FEP and 55 wt% FEP (the scale bar is 2 mm).

gaps between fibers. Settling down of FEP material on the surfaces of the samples could also contribute to the increased thickness.

Thermal conductivity results, shown in Figure 3.8(b), indicate that the 30% FEP loading GDL has the optimum thermal conductivity. This is a direct result of impregnation of the samples by the FEP material, which has a higher thermal conductivity than air ($\sim 0.2\ Wm^{-1}K^{-1}$ for FEP compared to the value of $0.02\ Wm^{-1}K^{-1}$ for air). The optimal value is a result of the trade-off between the higher conductivity of FEP material with the increased thickness of the FEP-treated GDLs which lengthens the conduction path inside the samples. The through-plane thermal conductivity values measured in this study are in the same range as through-plane values reported in the literature for woven GDLs [79]($\sim$ 0.28-0.32 $Wm^{-1}K^{-1}$) and non-woven GDLs [83]($\sim$ 0.15-2.1 $Wm^{-1}K^{-1}$).FEP loading has a significant impact on electrical conductivity as shown in Figure 3.8(c). Whereas FEP provide better heat conduction pathways

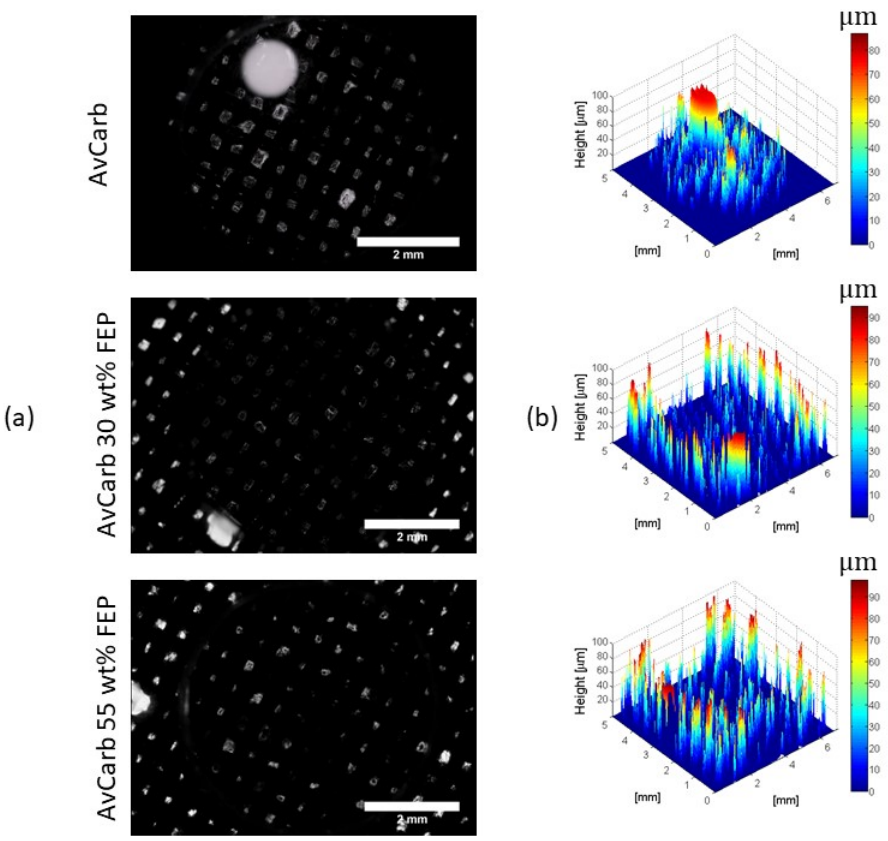

Figure 3.6: (a) Fluorescent microscopy of the breakthrough location (scale bar is 2 mm) (b) 3D map of water height in GDL and breakthrough location on the surface.

than air, it is an insulator for electric current, and the combination of impregnation of fibers, deposition of an insulating layer on the surface, and increased thickness result in a significant drop in electrical conductivity. Through-plane electrical conductivity data reported in literature are in the range of $\sim$ 250 - 2500 Sm^{-1} for non-woven GDLs [84, 85, 86].

3.5 Conclusion

Water transport, thermal conductivity, and electrical conductivity of woven GDLs with different FEP loadings were investigated in isothermal conditions at room temperature. Fluorescent microscopy visualization of water transport showed that for woven GDLs without FEP loading, water first fills bigger pores between yarns in

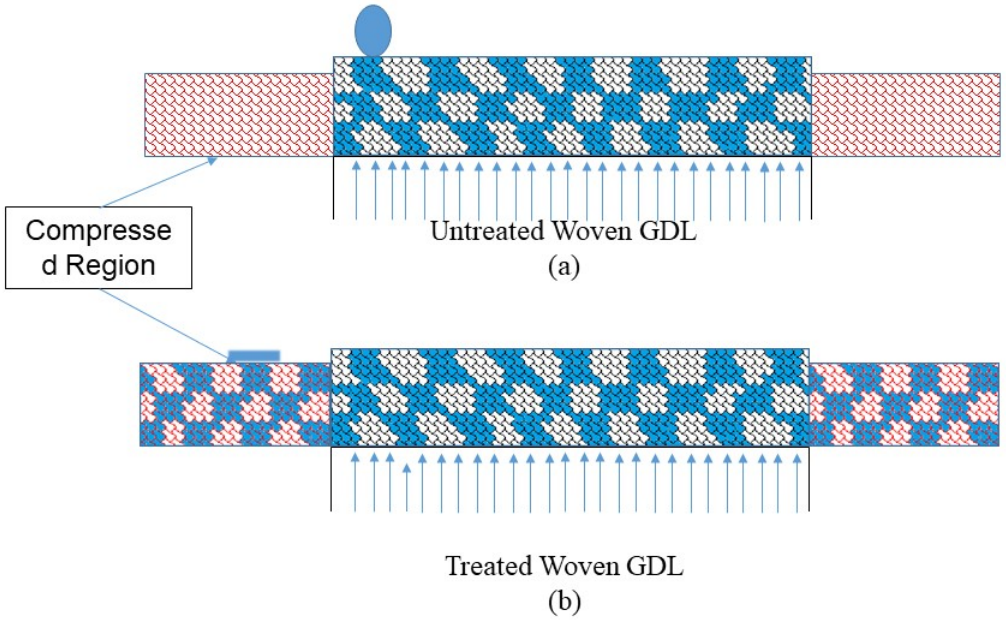

Figure 3.7: Water transport inside of (a) untreated and (b) treated woven GDLs.

the woven GDLs and then, breaks through a pore in the open area of the structure. FEP loaded-GDLs, however, have higher breakthrough pressures due to smaller pores and higher hydrophobicity. As such, water flows more in the in-plane direction of the GDLs. Furthermore, the occurrence of the breakthrough is in the area under compression. As in the case of non-woven GDLs [15], water breakthrough is due to distortion of the fibers and FEP material under compression. Higher FEP loading results in the swelling of the GDL due to partial filling of pores, possibly impregnation of fibers, as well as coverage of the sample surfaces with FEP material. Thermal conductivity measurements showed the existence of an optimum FEP loading (near 30%) as a result of a trade-off between the partial filling of the pores and increased the thickness of the sample by FEP. On the other hand, electrical conductivity decreased monotonically and significantly with FEP loading. In implementing woven GDLs in fuel cells, FEP treatment needs to be carefully determined in terms of trade-offs

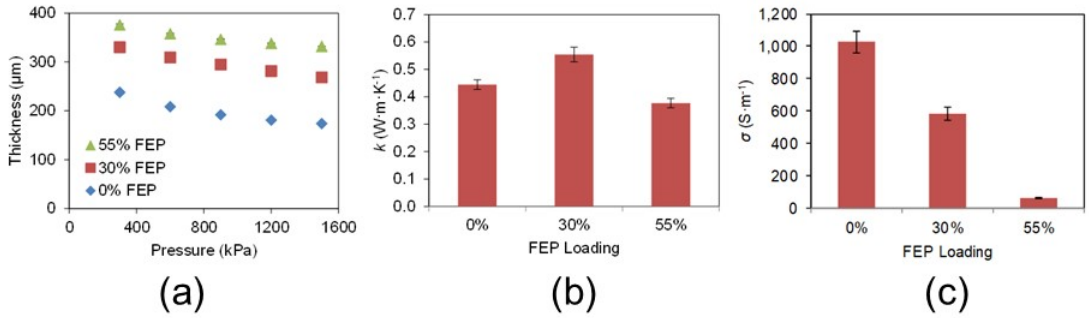

Figure 3.8: (a) Thicknesses of GDL samples versus pressure, (b) Thermal conductivity and (c) Electrical Conductivity versus FEP loading (number of sample = 3).

between improved water transport, heat, and electrical conduction, possibly using multi-objective optimization [87, 88].

Chapter 4

Electrode-integrated textile-based sensors for temperature and relative humidity monitoring in electrochemical cells

4.1 Abstract

Advances in textile technologies for transporting biomarkers and smart sensing are exploited in textile electrodes for electrochemical devices to achieve control of water transport as well as relative humidity and temperature sensing. The concepts are implemented and demonstrated within a textile gas diffusion layer (GDL) of the electrode of polymer electrolyte membrane fuel cells (PEMFCs). Ex-situ and in-situ characterization show that threads can be introduced in the GDL structure to inscribe water highways within the GDL with minimal impact on GDL microstructure and transport properties. Furthermore, a low-cost procedure was developed to transform commodity threads into temperature and humidity sensors by coating the threads with carbon nanotubes (CNTs) ink. Fluorinated ethylene propylene (FEP) is coated on top of the CNT coated thread to decouple the response to temperature and humidity; the resulting threads achieve a linear change of resistance with temperature (-0.31 %/°C), while relative humidity (RH) is monitored with a second thread coated with polydimethylsiloxane (PDMS). The combination of both threads allows minimally invasive and dynamically responsive monitoring of local temperature and RH

within the electrode of PEMFCs.

4.2 Introduction

Electrochemical energy conversion and storage technologies are central to the decarbonization of the transportation and power sectors. They provide the reliability and flexibility required to bring low-cost intermittent renewable energy sources into major energy consumer sectors [89]. Porous electrodes are pivotal components in many electrochemical devices, such as polymer electrolyte membrane fuel cells (PEMFCs) [5] and redox-flow batteries [90, 91]. Electrodes typically consist of a multi-layered porous structure, and their performance is significantly influenced by the structure and wetting properties of the pores2. Porous electrodes of PEMFCs require a water management strategy to ensure adequate durability and performance [5]. A particularly challenging aspects of water management is dealing with the inhomogeneous reaction and water production rates in the catalyst layer (CL) [92, 52] and the non-uniform temperature and humidity distribution.

Water management requires balancing both membrane humidification to ensure good ionic conductivity and removal of excess water, which can block the pores and hamper reactant gases transport to the CL, i.e. the "flooding" phenomenon [6, 7, 14]. Poor water management leads to increase stack size, higher cost and reduced power density [17]. Gas diffusion layer (GDL) is a porous structure responsible for the transport of air and hydrogen (reactants), water (by-product), heat and electrical current [14, 9]. Water transport is mainly controlled by capillary pressure, which is a function of pore size and hydrophobicity of the GDL. In high current density, the excess amount of water reduces PEMFCs performance significantly due to flooding. Different avenues for GDL water management have been pursued. (1) Using perforated metallic GDLs with different pore sizes and distributions shows better performance at high current density. However, the durability of these GDLs is significantly reduced by corrosion [93, 94]. (2) Generating through-plane holes ($\sim$ 80 µm) in the cathode side of the GDL under the flow channels has been shown to reduce the capillary pressure and remove the excessive water [1, 33, 34, 32]. This approach improved the performance of the fuel cell by reducing the cathode overpotential, particularly, in a low humidity environment. However, a drop in performance was observed at high humidity and current densities [32]. (3) Adding a wicking layer to the back of the GDL to remove excess water by hydraulically linking the entire cathode surface was

practiced [3]. Although this approach alleviates the flooding issue in fuel cells, the performance gain is minimal. (4) Fabian et al. [4, 95] invented an active water management strategy by introducing a micro pump to enhance water removal. Promising results were presented for air-breathing fuel cells, but the application of such pump in large scale stacks has not been studied. Furthermore, this approach would increase cost. (5) Tuning wettability of the GDLs and microporous layers (MPLs) [96] (i.e. a thin layer added to the GDL to achieve more uniform reactant distributions) is a promising avenue that has been studied recently. Forner-Cuenca et al. [5] engineered the hydrophobicity of the GDL by radiation grafting of hydrophilic polymers and generating water channels in off the shelve GDLs. The results indicated better water management and better performance of the cells in low humidity (cathode side) environment. In three consecutive studies, the grafting strategy [38], *ex-situ* analysis [18] and *in-situ* fuel cell testing via neutron imaging were studied [39]. However, the large-scale utilization of this improvement requires significant changes in manufacturing facilities. The path forward in the enhancement of GDL performance is to devise responsive systems that retain water as needed in specific locations or at certain operating points, while removing water that accumulates in the porous structure at other locations/conditions; monitoring of local parameters (e.g. temperature and relative humidity) is critical to implementing this approach. This paper describes a new approach that simultaneously allows monitoring and improves water management.

Reducing non-uniformity of temperature and humidity [97] is crucial to maintaining ionic conductivity [98] and alleviating degradation of polymer electrolyte membranes [98]. Accurate knowledge of local temperature and humidity is essential for improving water management as well as for improving the accuracy of performance predictions. Conventional methods of temperature and humidity monitoring lack spatial resolution and typically measure temperature and humidity of reactants at the input and the by-product at the output of the cell [99]. Various methods to access the cell temperature locally have been proposed using thermocouples [41, 100, 101, 42], optical sensors [52, 50] and micro-electro-mechanical systems (MEMS) [47, 46, 102, 103, 104, 102, 45]. Zhang et al. [41] placed 11 thermocouples between the GDL and the CL to monitor temperature distributions. The flow field was modified to place these thermocouples, thus covering valuable area of the CL and reducing the active area for the catalysis. This approach has also been employed by other researchers [100, 101, 42]. Use of optical sensors was demonstrated by David et al. [52, 53, 105] who developed an in-fiber Bragg grating (FBG) sensor and imple-

mented it an operating fuel cell to simultaneously measure temperature and relative humidity (RH). In addition to good accuracy, this sensor provides dynamic response up to 1Hz. The size of the fibers ($\sim$ 30 µm) however restricted its deployment to a distance from the reaction zones in the CL. MEMS have paved the way for new sensing techniques. For example, Lee et al. [47] fabricated a MEMS device located between the membrane and the CL that captures local temperature and RH. This device requires MEMS fabrication on the membrane with partial covering, and monitoring of different locations requires fabrication of a different MEMS-membrane which is both costly and cumbersome.

While non-uniformity of parameters such as temperature and RH in the plane of the electrode is well established, studies also show that there are significant *through-plane* gradients between outer plate temperature and the reaction zone temperature [7]. While several methods have been successful in monitoring these non-uniformities *in-situ* [104, 106] they have not been adopted for monitoring in commercial stacks due to a combination of (1) requirement for significant design changes of the cell, (2) need of additional components, and (3) reduction in active area and negative impact on performance.

The development of appropriate sensing, thermal and water management solutions for electrochemical energy applications can take advantage of innovations in textile technologies that have for instance shown promising results in biomedical applications. One of the avenues relies on wicking property of threads to transport biomarkers through the threads [107, 66, 108]. Threads can be easily patterned on a textile substrate to design a network for transport of different stream of flows. Junker et al. [109] showed that a network of threads can be used in a low cost process for designing a microfluidic circuits. In addition to facilitating transport, threads have been used for sensing in biomedical applications by coating commodity threads with novel materials such as carbon nanotubes (CNTs). Such thread-based sensors have been used to monitor physical and chemical properties such as [110], pH [111], temperature [66] and humidity [58]. Akbari et al.[66] demonstrated a process in which a commodity thread was transformed into a temperature sensor by simple dip coating in a CNT ink; the sensor exhibited a simple linear relationship between temperature and thread resistance. Besides temperature, CNT coated substrates are also responsive to change of humidity as has been shown for a variety of substrates such as cellulose papers [112], composite films [113] filaments and fabrics [58]. Zhou et al. [58] developed high strength filaments out of CNT and poly(vinyl alcohol) via a wetspinning process. The

filament resistance followed a quadratic response to change of RH between 60% to 100% over a range of temperatures [25 °C to 75 °C] that coincides with PEMFCs.

Based on the promising results of textile technology in bio-medical application, thread-based temperature and humidity sensors were for the first time developed and integrated within a carbon cloth GDL for continuous temperature and humidity monitoring. Taking advantage of the wicking properties of the thread, water pathways were engineered by patterning GDLs to facilitate transport of excess water. Microstructure analysis, scanning electron microscopy (SEM) and X-ray microtomography (X-µCT), were performed to characterize modified porous GDL. In-situ fuel cell testing was performed on modified samples and pristine samples to evaluate the effect of threads on the performance of the fuel cell over a range of conditions representative of actual fuel cell operation.

4.3 Results and Discussion

Integrating multifunctional threads within carbon cloth GDLs provides (1) preferential water "pathways" and (2) sensing capability within the fuel cell membrane-electrode assembly (MEA). Figure 4.1(a) shows the process for treating and sewing hydrophilic threads onto carbon cloth GDLs using a commercial sewing machine. The proposed low-cost process uses roll-to-roll system to coat commodity threads with CNT inks by dipping and drying (Figure 4.1(b)). Threads made of polyester, which has high wicking property compared to other commodity threads (see FigureB.1), provided preferred pathways for water to cross carbon cloth GDL (Figure 4.1(a)) with a minimal impact on GDL microstructure. To add sensing within GDLs, the conductive CNT coated threads were functionalized to be temperature and humidity sensors. This requires a layer to insulate the thread from the conductive substrate (carbon cloth GDLs), as well as a protective layer to mitigate the sensitivity to humidity. Polydimethylsiloxane (PDMS) is an insulator with the high water vapor transmissivity required for RH sensitivity. PDMS can be easily wrapped around the CNT coated thread via a dip coating process (Figure 4.1(c)). To achieve temperature sensitivity, fluorinated ethylene propylene (FEP) was used to coat the CNT-coated thread; this provides both insulation and mitigation of water vapor transmission allowing measurement of temperature independently. The thread-based sensors monitor temperature and humidity locally and communicate wirelessly with a personal computer (PC) or smartphone. A schematic of sewing thread-based sensors on a piece of car-

bon cloth GDL is shown in Figure 4.1(d). The detailed analysis of these integrated sensors-textile electrodes is presented in the following figure panels.

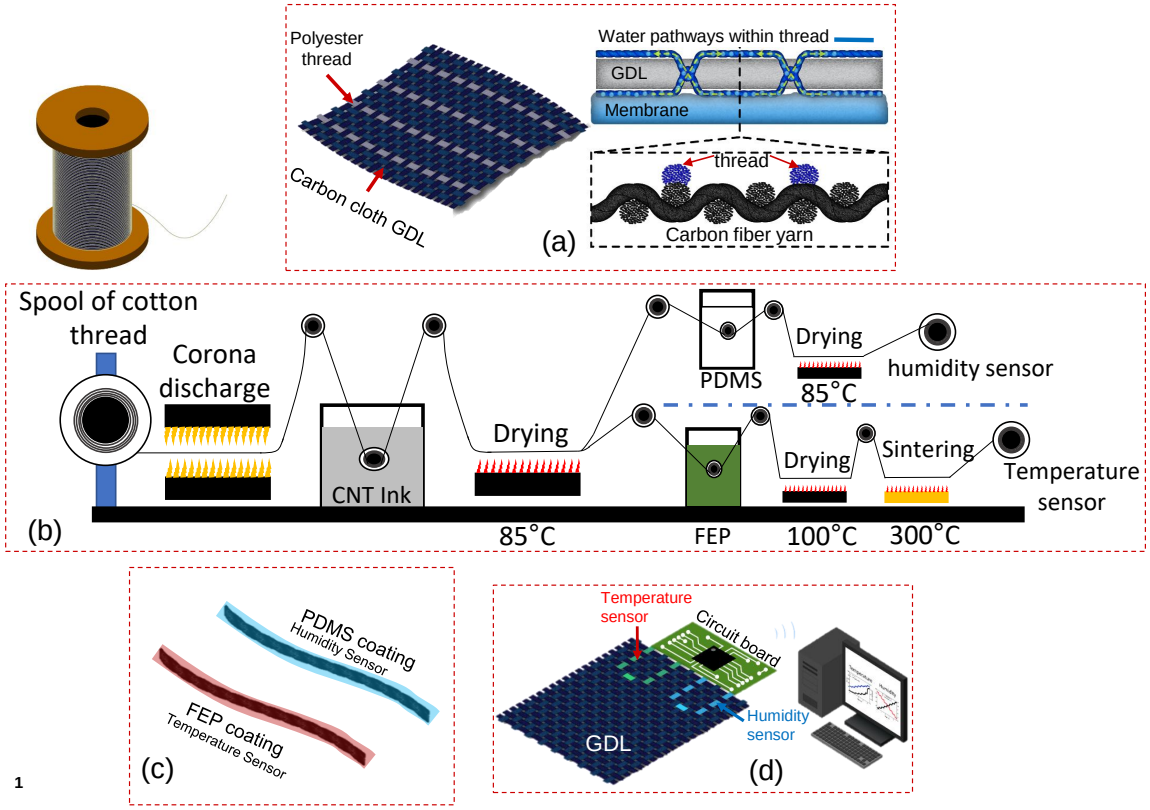

Figure 4.1: Schematic of process to modify carbon cloth GDL via sewing hydrophilic, temperature and humidity sensing threads. (a) Polyester threads were sewed on carbon cloth GDL generating hydrophilic pathways for water removal. (b) Roll-to-roll process of dip-coating cotton thread to confer humidity and temperature sensitivity. (c) FEP for temperature sensing and PDMS coating for humidity sensing. (d) Sewing of thread-based sensors for wireless monitoring of temperature and humidity.

We evaluated the effect of addition of threads on physical properties of the GDL. A carbon cloth GDL has a plain weave of carbon yarns with a size of ∼422±3 µm. The SEM image revealed the two-dimensional (2D) view of the microstructure of a plain GDL in Figure 4.2(a). A piece of polyester thread was treated with a corona discharge to enhance the wicking property of the thread (Figure B.2 showed the wicking test results and the SEM images of the thread in Figure B.3). The treated polyester thread with a diameter of ∼ 232±3 µm was sewed on a piece of cloth GDL,

as depicted in Figure 4.2(b). The SEM image showed the thread was embedded in the pristine GDL with a minimal impact on microstructure. For non-woven GDLs, such as Toray 090, the microstructure was impacted as is shown in Figure B.4. Threads were sewed in a straight line on a GDL with two patterns, 1 mm and 4 mm distance apart with a pitch of 1 mm. An in-house tool, thickness under compression and resistance under compression TUC_RUC), was utilized to measure the thickness and through-plane electrical conductivity in different compression pressures. This tool has been used and evaluated in previous studies [27, 114]. The thickness increased by 100 µm for the 1 mm distance threaded GDL and 60 µm for the 4 mm at 1500 kPa. It showed that the thickness of the modified GDL is in the range of commercial products (Gray area in Figure 4.2(b) 370 μm for Toray 120 and 110 µm for Toray 030 are the thickness of these two commercial products). On the other hand, electrical resistance under compression yields similar results compared to the pristine sample, even though the threads are non-conductive (Figure 4.2(b)). Another property is the effect of thread on the water breakthrough pressure, i.e. the required pressure for water to penetrate a porous structure. This test was performed on pristine and threaded samples. The breakthrough pressure decreased 30% for threaded GDLs (Figure 4.2(c)); however, the breakthrough pressure for non-woven GDL is zero due to significant structure alteration (Figure B.4). The reason for lower breakthrough pressure might be due to a change in hydrophobicity of the structure rather than the sewing process. Hydrophobicity and contact angle were characterized using sessile drop tests. A water droplet was placed on the GDL the contact angle remained constant over 6 minutes (115°); however, for water droplets on the thread the angle changed (from 101° to zero) and the droplet wicked through the polyester thread in 6 minutes (Figure 4.2(d)). This suggests that the thread wicking property can be used to developed water pathways within GDLs.

In this panel, we investigated the effectiveness of the thread in creating water transport pathways using fluorescent microscopy. High temporal resolution was used to track dynamic water transport through the porous structure [27]. Figure 4.3(a) shows that water first transported in the in-plane direction and filled pores of the GDL, and then, the breakthrough occurred; however, for the GDL with thread, water transported through the threaded regions with the remaining area open for eventual reactants transport (Figure 4.3(b)). The three-dimensional (3D) view of the water transport confirmed that the threaded area is the main pathway for water transport compared to the pristine sample. In addition, the breakthrough location remained

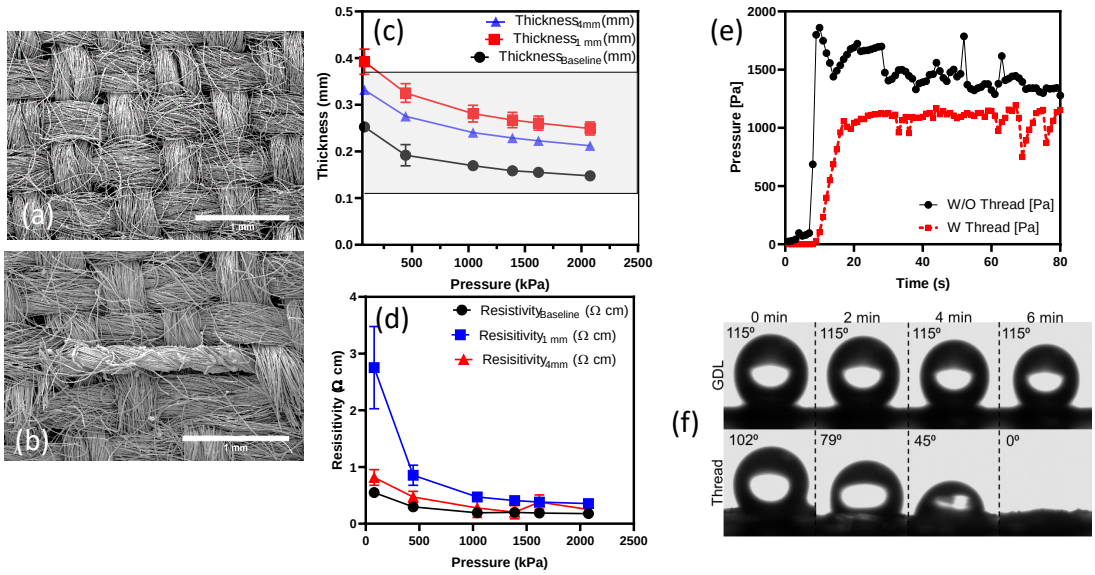

Figure 4.2: Investigating effect of threads on physical properties of GDL. SEM image of carbon cloth GDL (a) pristine and (b) with hydrophilic thread (scale bar is 1 mm). (c)Thickness under compression and resistance under compression for pristine carbon cloth, with 1 mm and 4 mm distance with 1 mm pitch distance of the hydrophilic thread. (e) Effect of hydrophobic thread on water breakthrough pressure. (f) Contact angle of sessile water droplet on carbon cloth GDL and thread. Error bars represent standard deviation (SD) (n = 3).

fixed for the modified GDL, whereas for the pristine GDL, water transport occurred in three different locations (shown with yellow arrow) in three consecutive breakthrough tests (Figure 4.3(c)). The effect of thread hydrophobicity was also analyzed with the blue area corresponding to a hydrophilic thread (polyester) and the red area to a hydrophobic thread (carbon fiber yarn); both threads were sewed similarly on the substrate. The water breakthrough test showed the hydrophilic region was wetted and the hydrophobic thread did not show any sign of water. This indicates that the wetting properties are more important than the sewing process in determining preferential water breakthrough location (Figure 4.3(d)). These results demonstrate that threads can be embedded in the structure of GDL to effectively create water pathways.

The depth of field of 2D SEM images limits observations to the inner layer of modified GDLs. Internal change in microstructural properties were analyzed using X-µCT. High resolution (voxel size of 3.16 µm) tomography resolves the pores and

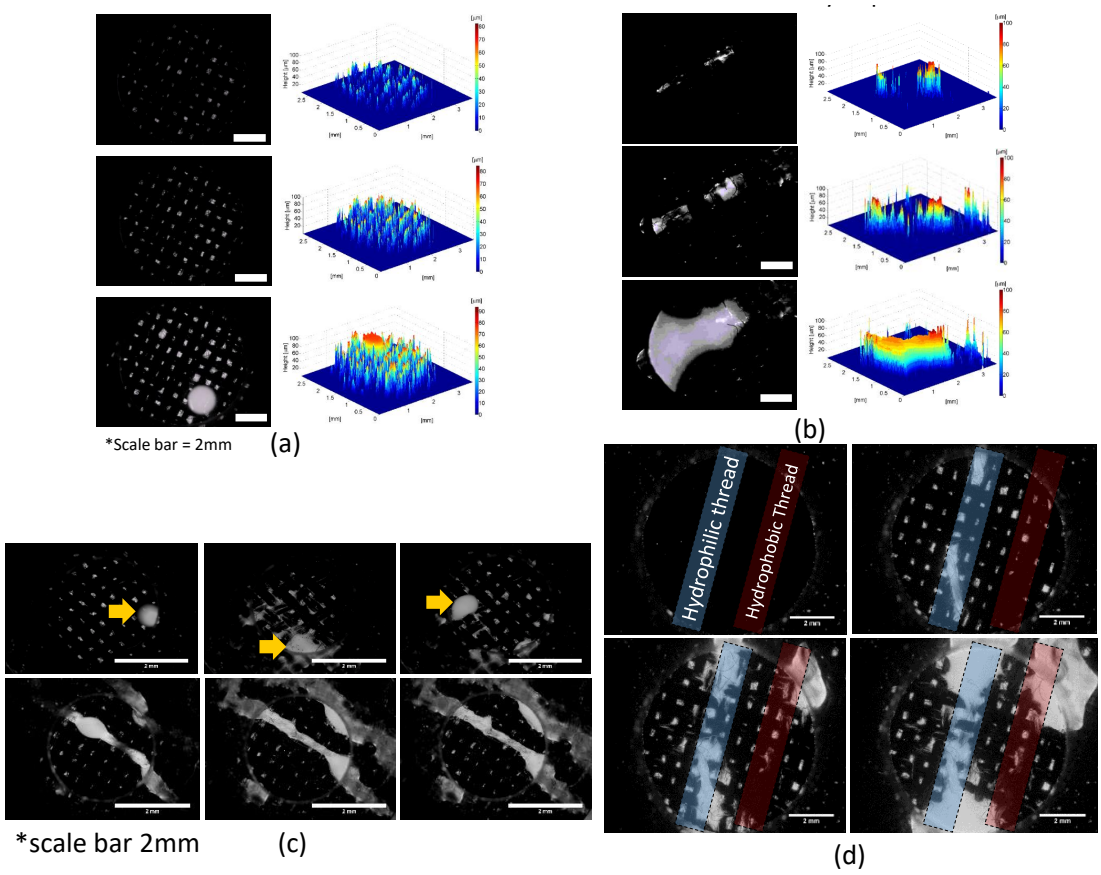

Figure 4.3: Water transport analysis via fluorescent microscopy. (a) Pristine carbon cloth and (b) with hydrophilic thread. (c) Fixed water breakthrough location for GDL with thread and (d) effect of hydrophobic and hydrophilic thread on breakthrough location.

3D structure of the GDL allowing evaluation of the transport properties. A piece of carbon cloth GDL with and without thread was scanned. The grayscale images consist of voxels with different grayscale values. The voxels of (1) pores were assigned to zero, (2) carbon fibers to one and (3) the thread to two via a manual segmentation tool using Avizo software, which allows generation of a 3D image of the substrate and segments three different phases. The sample size with an area of (2.7 mm $\times$ 2.7 mm) is shown in Figure 4.4(a) and (b). One of the key properties is the bulk porosity, which is a fraction of pore volume to the total volume, was found to drop by $\sim$5% compared to pristine samples (Figure 4.4(c)). The 3D image allows for not only an estimation of the bulk porosity, but also the variations of the porosity along any directions. The through-plane (TP) direction is shown in red and the two in-plane

(IP) directions perpendicular to TP are shown in blue and green in Figure 4.4(a). For the sample with stitch, the IP direction was separated in two parts, parallel to the thread ($IP_{Parallel}$), blue, and perpendicular to the thread ($IP_{Perpandicular}$), green. Because the thread direction imparts complete anisotropy, these two directions must be investigated separately. Porosity distributions in three main axes shows the non-homogeneity of the porous structure along different directions [115]. The TP and ($IP_{Perpandicular}$) to the threads show a similar trend of porosity distributions compared to the pristine sample (the black line (TP) and the red line ($IP_{Perpandicular}$) graph in Figure 4.4(d) and (e)). However, there is a sharp drop in local porosity in the parallel to the thread direction compared to the pristine sample (the blue line ($IP_{Parallel}$) in Figure 4.4(d) and (e)). The porosity dropped $\sim 40\%$ locally in $IP_{Parallel}$. This drop however, is a location that potentially will be filled with water during the fuel cell operation due to water wicking and will be emitted in effective porosity estimation of the sample [16]. Although it shows significant porosity changes locally, it could keep other pores available for the reactant transport.

For the model based on X-µCT images, these properties were estimated using Avizo Xlab [74]. This software solves continuum transport equations through a representative reconstructed porous domain [116]. The domain size that can be a representative volume element of the porous media was chosen to be 500 µm × 500 µm × Thickness [74, 117].Since GDLs have an inhomogeneous structure, the permeations were measured in three main directions, TP, $IP_{Parallel}$ and $IP_{Perpandicular}$. The permeability measurement is based on Darcy's law. As expected from the literature [118], the TP direction has lower permeability values than IP directions. Introducing a thread reduced the permeation in the TP and IP directions. In the $IP_{Perpandicular}$, the change was more significant (from 51.6 μm^2 to 22.6 μm^2) relative to the $IP_{Parallel}$ (Figure 4.4(f)). The diffusivity was estimated based on Fick's law and found to be lower compared to the pristine GDL. it can be estimated that the molecular diffusion is less affected as a result of this modification (Figure 4.4(g)). Finally, the thermal conductivity was determined in similar steps. The thermal conductivity decreased with the introduction of thread; however, there is no difference in $IP_{Perpandicular}$ and $IP_{Parallel}$ (Figure 4.4(h)). In summary, investigation of microstructural and transport property changes show that introducing threads for combined water management and sensing threads comes with the penalty of slightly lower but still acceptable transport properties compared to commercial products (i.e. Toray 090 permeability 10.5 μm^2 in IP and 3.5 μm^2 and diffusivity 0.36 in TP and 0.63 in IP [74]).

The trade-off between improved water transport and reduced transport properties was evaluated by in-situ testing of threaded GDLs in an operating fuel cell. A carbon cloth GDL with a thread 4 mm apart, parallel to the flow field channel, was located on the cathode side where water management is more crucial. A pristine carbon cloth GDL was placed on the anode side to make a membrane electrode assembly (MEA) and compared the results with an MEA with pristine woven GDLs on both sides. Figure 4.5(a)-(c) shows the polarization curve of the threaded MEA (blue line) and the pristine MEA (black line). The tests were performed at three different RH values (100%, 60% and 40% at 60 °C). At high RH, the performance of both MEAs is similar; however, in low RH the pristine sample exhibited better performance; this is expected as excess water/flooding does not typically occur under low RH conditions. The in-situ testing indicated that the usage of thread did not drastically alter the fuel cell performance in various conditions. It shows that the potential capability of introducing sensing threads for monitoring temperature and humidity with minimal adverse effects on the performance of PEMFCs.

In previous experiments, it was shown that threaded GDLs do not reduce fuel cell performance; next *sensing* threads that can monitor temperature and humidity locally, were investigated. Sensing was achieved by coating a cotton thread (Figure 4.6(a)) with CNT ink (functionalized multiwalled carbon nanotubes (fMWCNTs) with sodium dodecyl sulfate (SDS) dissolved in distilled water) (Figure 4.6(b)). The key properties of fMWCNTs for this application are (1) conductivity and (2) sensitivity to both [66] and humidity [58]. The resistance of the CNT coated substrate changed according to temperature and humidity changes. Previous studies used the sensing property of CNTs for either temperature or humidity monitoring. Since both parameters can vary simultaneously in an operating fuel cell, the signals have to be segregated. This requires a coating that (1) insulates from a conductive substrate (e.g. carbon cloth), (2) mitigates the response to either humidity changes, and (3) is flexible enough to be sewn into a substrate. PDMS, a flexible polymer that can easily coat a variety of substrates, was used to provide a thin insulating layer around the thread (Figure 4.6(c)). PDMS also has a high water vapor transmission rate and therefore does not inhibit RH sensing with CNT coated threads. For temperature sensing, FEP was used to stop/reduce RH sensitivity. FEP is a hydrophobic polymer that increases the hydrophobicity of a GDL [5], has a low water vapor transmission rate, and also has sufficient flexibility to be sewed on a substrate. The CNT coated thread was coated with a 55% FEP solution. There are cracks on the surface of

the FEP layer. The reason might be because of the fast drying process during the sintering of FEP on the thread. Figure B.6 shows similar surface cracks for different threads. During the sintering process Each coat (PDMS and FEP) increased the diameter of the thread. In this work, a cotton thread with a diameter of 350 µmm was used. After PDMS coating, the diameter increased to 400 µm, and with FEP coating increased to 590 µmm. This can be easily tuned by choosing a thread with a different initial diameter. Figure 4.6(f) shows images of the two sensing threads.

To analyze the response of both sensors, three samples (3 cm long thread) of (1) PDMS+CNT- coated, and (2) FEP+CNT-coated were prepared and tested in an environmental chamber. The testing conditions were similar to those in a typical fuel cell (60 °C and RH varying between 30% and 90%). The measurements were performed after steady state conditions were reached in the environmental chamber (30 minutes for each state and for ramping time). The resistance of the threads was monitored at 20 second intervals. Figure 4.7(a) shows that the resistance of PDMS coated threads followed RH cycle (blue line) at constant temperature (red line). However, the resistance of FEP coated thread showed a small change with large RH changes (less than 15%). The PDMS coated thread resistance showed the same trend for repeated cycles over a 7-hour test cycle (Figure B.7). The tests were repeated three times for each condition and a similar pattern with a variation of 4.5% was observed as shown in Figure B.8. This indicates that FEP coating can mitigate the RH response of the CNT coated thread and can be used solely to monitor temperature, while PDMS coated threads can be used for RH sensing. The environmental chamber was programmed to change RH from 30% to 90% for over 13 hours. The resistance of the PDMS coated thread (black line) followed the pattern of the RH curve (blue line) (Figure 4.7(b)). The change of the resistance of the thread was more sensitive in high RH values (more than 60% RH), which is more critical for PEMFCs application since the membrane of fuel cells must always to be hydrated [119]. The test was repeated at °C and 85 °C. It was shown that the thread resistance followed a quadratic function of RH. A similar pattern was observed for all three temperatures with slightly higher sensitivity at 75 °C. The variations between different samples might be associated with the dip-coating procedure of CNT and PDMS on the thread (Figure 4.7(c)).

Thread-based temperature sensor response was characterized first by rapid temperature cycling from 50 °C to 120 °C. The resistance varied inversely with temperature and returned to the initial resistance with no hysteresis. The tests showed

good repeatability (Figure 4.7(d)). The temperature response of FEP+CNT coated thread characterized by varying temperature between 50 °C to 120 °C in steps (with increment of 10 °C and ramping time of 1 hour and steady time of 1 hour). Figure 4.7(e) shows the stepwise decrease in resistance of the thread by increasing temperature. The linear graph of the thread resistance vs. temperature (with the slope of -0.31%/°C) is illustrated in Figure 4.7(f). The combination of both threads, PDMS coated and FEP coated, can be embedded in textile GDL in an operating fuel cell for mapping temperature and humidity locally. In order to showcase the feasibility of the proposed approach and provide a proof of the concept, two pieces of thread-based temperature sensors (FEP coated) were sewed on a piece of carbon cloth GDL to monitor temperature of the substrate locally (Figure 4.8(a)). The modified GDL was placed on a flow field (Figure 4.8(b)) and then exposed to non-uniform heat, which was generated by a hot plate to develop a non-uniform temperature distribution across the GDL. The sample was monitored by an Infrared (IR) camera over 30 minutes. Four snapshots from the IR camera indicated the temperature distributions from 27 °C up to 95 °C. The temperature sensor locations are labelled in Figure 4.8 as '1' and '2'. The resistance of the threads was monitored wirelessly via an in-house made circuit board that communicated with a smartphone, (Figure 4.8(c)). The resistance was correlated to the temperature based on a linear decrease in the value. The sensors monitored the temperature rising from 50 °C to 90 °C and 35 °C to 65 °C for location 1 and 2, respectively. Meanwhile, the temperature was captured via an IR camera and compared with thread-based temperature sensors. Six time points were chosen for comparison between these two measurement methods, exhibiting a good agreement between the IR camera results and the thread-based temperature sensors (Figure 4.8(d)). The temperature map at four time points were depicted in Figure 4.8(e). These results indicated that thread-based sensors can easily map temperature on a textile electrode.

4.4 Conclusions

In this work, we developed an integrated approach for sensing and water management in fuel cells that uses functionalized threads. Selective hydrophilic pathways were generated within the porous structure of an electrode through low cost sewing threads that provide. The microstructural analysis showed external threads were embedded within the GDL with minimal impact on transport properties. In-situ fuel cell testing

suggested that the impact on the overall performance is minimal while enhancing the water management at the expense of reducing transport properties. Furthermore, cotton threads were transformed into humidity and temperature sensors via incorporating CNTs into cotton yarns with two separate protective layers (PDMS for the humidity sensor and FEP for the temperature sensor). The thread-based humidity sensors showed a quadratic resistance increase to the change of RH (between 60% and 90%) while temperature sensor responded a linear resistance decrease to change of temperature (between 50 °C and 120 °C). These sensors can be embedded into the textile electrode for monitoring temperature and RH locally without compromising the fuel cell performance. The ex-situ temperature monitoring was performed on a carbon cloth GDL with a non-homogenous temperature distribution, which proved the workability of the sensors. This study indicates that textile electrodes in electrochemical devices, specifically fuel cells, can be modified to control the transport of by-products, i.e. water, and also monitor local parameters, i.e. temperature and RH, by adding sensing yarn to textile electrodes. Besides, these electrodes have potential applications in flexible and wearable textile batteries [120, 121, 122].

4.5 Experimental Section

4.5.1 Preface

The experimental part of this chapter was performed as follow: I was responsible for the water transport experiments, thickness and electrical conductivity measurement, performing transport analysis, CNT ink perpetration, coating process, the experimental setup of temperature and RH measurement, data analysis and writing the article. An in-situ fuel cell test was performed at the Ballard power system. Tavia Walsh performed wireless monitoring of temperature. Armin Rashidi performed X-ray microtomography at UBC Okanagan.

Materials:A woven GDL, AvCarb 1071 HCB, non-woven GDL, Toray 090, and fluorinated ethylene propylene (FEP) (FEPD121 DuPont 55% solids) were purchased from Fuelcell Earth, functionalized multiwalled carbon nanotubes (fMWCNT), sodium dodecyl sulfate (SDS) and rhodamine B were purchased from Sigma-Aldrich.

Microscopy: The scanning electron microscopy (SEM) images were captured by Hitachi S-4800N. Fluorescent microscopy was performed via an upright fluorescent microscope (DP 73 Olympus BX51), with CY3 filter and 2X objective and numerical

aperture (NA) of 0.06 to observe water transport. A sessile drop of distilled water contact angle was measured with a goniometer from DataPhysics (model TBU 90E).

Fluorescent Visualization and Breakthrough Pressure: Water breakthrough pressure was measured via a differential pressure transducer (Honeywell FP2000) with a data acquisition system. Following our previous study [27], a syringe pump was used to inject a dilute distilled water solution of 1mM rhodamine B (excitation: 540 nm and emission: 635 nm) with a rate of 0.02 ml/min to the apparatus. The water height is correlated to the intensity of the image since the depth of field calculated from $d_field = \lambda/NA^2$, which is 150 µm, and due to the porous structure, the depth of field is up to 7-8 fibers which is ∼100 µm. As a result, the height calculated from $\eta = 100/255I[\mu\text{m}]$, where η is the observable height and I is the intensity of the image. The field of view is 6.5 mm × 5 mm and the resolution is 4.6 µm. The detail of the imaging is in Ref [27].

Thickness and Electrical Conductivity Measurement: A custom-made testbed (known as thickness under compression-resistivity under compression -`TUC_RUC`) was used to measure the sample thickness and the through-plane resistivity at various pressures. A sample was clamped between two gold-plated probes. To cancel electrical contact resistance (ECR) between plates and GDLs, it is required to test different thicknesses, which was achieved by stacking GDLs. By subtracting two stacks, ECRs between the probes and the GDL surfaces were mitigated, and since the ECR in stack of GDLs is negligible, the obtained value is the GDL resistivity, as shown in previous studies [27, 77].

X-µCT Imaging: X-ray microtomography (X-µCT) was performed by a Zeiss MIcroXCT-400 machine at UBC Okanagan. A 5 mm × 5 mm sample was cut and secured to the sample holder. It was glued to avoid any fluttering during movement. 2500 radiograph images obtained in spanning 360 degree with exposure of 15 seconds. A 4X objective lens was used to acquire spatial resolution of 3.16 µm for each micrograph. Image processing were performed by ImageJ, MATLAB and Avizo software followed by reconstructing the 2D slices from the scans. First, a median filter with a kernel size of 2 was applied on grayscale images to reduce the noise, then manual thresholding was performed to segment the materials from background. In order to segment the thread from the substrate, segmentation module of Avizo was used to manually separate the thread from GDL for subsequent transport properties analysis.

Transport Properties Estimation: The bulk porosity and porosity distribution were obtained by calculating porosity in each 2D radiograph. The details of the

procedure can be obtained from ref. [123]. For the permeability analysis, Darcy's law was employed via the absolute permeability experiment simulation tool within the Avizo X-lab module with a convergence criterion 10^{-6}. Molecular diffusivity following Fick's second law was solved with Molecular Diffusivity Experiment Simulations tool within Avizo X-lab module and thermal conductivity simulation was performed with Avizo XLAb thermal conductivity module.

In Situ Fuel Cell Testing: A single cell with an MEA size of 90 mm × 50 mm and flow field with channel size of 1.1 mm and landing 0.21 mm was used for the testing. The temperature set to 60 °C. RH in anode set to 100% and RH in cathode varied between 40% to 100%. A catalyst coated membrane (CCM) was 30 wt% Nafion and 0.1 mg/cm^2 and 0.4 mg/cm^2 Pt loading on anode and cathode, respectively. The control MEA has two carbon cloth (Avcarb 1071 HCB) on both cathode and anode sides. The carbon cloth (Avcarb 1071 HCB) with a thread sewed (polyester thread) 4 mm apart was used in the cathode side of MEA and in the anode side a pristine GDL was used.

Preparation of CNT Ink: 1.6 mg/ml fMWCNT and 10 mg/ml SDS were dispersed in distilled water with 1-minute probe sonication to achieve a well-dispersed solution.

Preparation of CNT Coated Cotton Thread: A commodity thread first corona discharged to enhance the wetting property. Then, they were dipped coated 6 times and dried in oven at 80 °C for half an hour in each dipping.

FEP Coating and PDMS Coating of CNT Coated Thread: A CNT coated thread was dipped into 55% FEP solution followed by de-moisorization at 100 °C in a hot plate. Subsequently, it was heated up to 300 °C in order for sintering FEP onto the thread. The CNT coated threads were dipped into PDMS (10:1 ratio of PDMS and curing agent) and dried on a hot plate at 90 °C for two hours.

Temperature and Humidity Measurement: The temperature and humidity were controlled by an environmental chamber (TESTEQUATY model 123H). Three pieces of thread-based sensors were placed in the chamber and the resistance was monitored by in-house made board.

Wireless Monitoring of Temperature: Two off-the-shelf components, the Arduino Nano Every and the HC-06 Class 2 Slave Bluetooth module, were used for data processing and transmission. For separate and simultaneous measurement of the surrounding environment's temperature and humidity, the output voltages of the two electrodes were logged by an Arduino (SparkFun, Niwot, CO, USA) microcontroller

with a 1kHz sampling frequency. A voltage divider circuit with an applied 5V voltage source and known R1 resistor values was employed to determine the resistance of the electrode, R2, via thresholding of the resulting analog output voltage. To reduce the error in measurement of the output voltage, a range of resistor values (100-10MΩ) was used to compare against the unknown electrode resistance in the voltage divider. The calculated electrode resistance data was then sent to a HC-06 (DSD TECH, USA) wireless serial Bluetooth module, and then transmitted to a mobile phone. A custom Android app allowed for the continuous collection of the temperature and humidity conditions. Electrode resistance measurements were updated every five seconds.

IR Camera: A thermal camera (Seek Thermal-Compact) was used to map temperature distribution. It monitored the change of temperature over a 30-minute test.

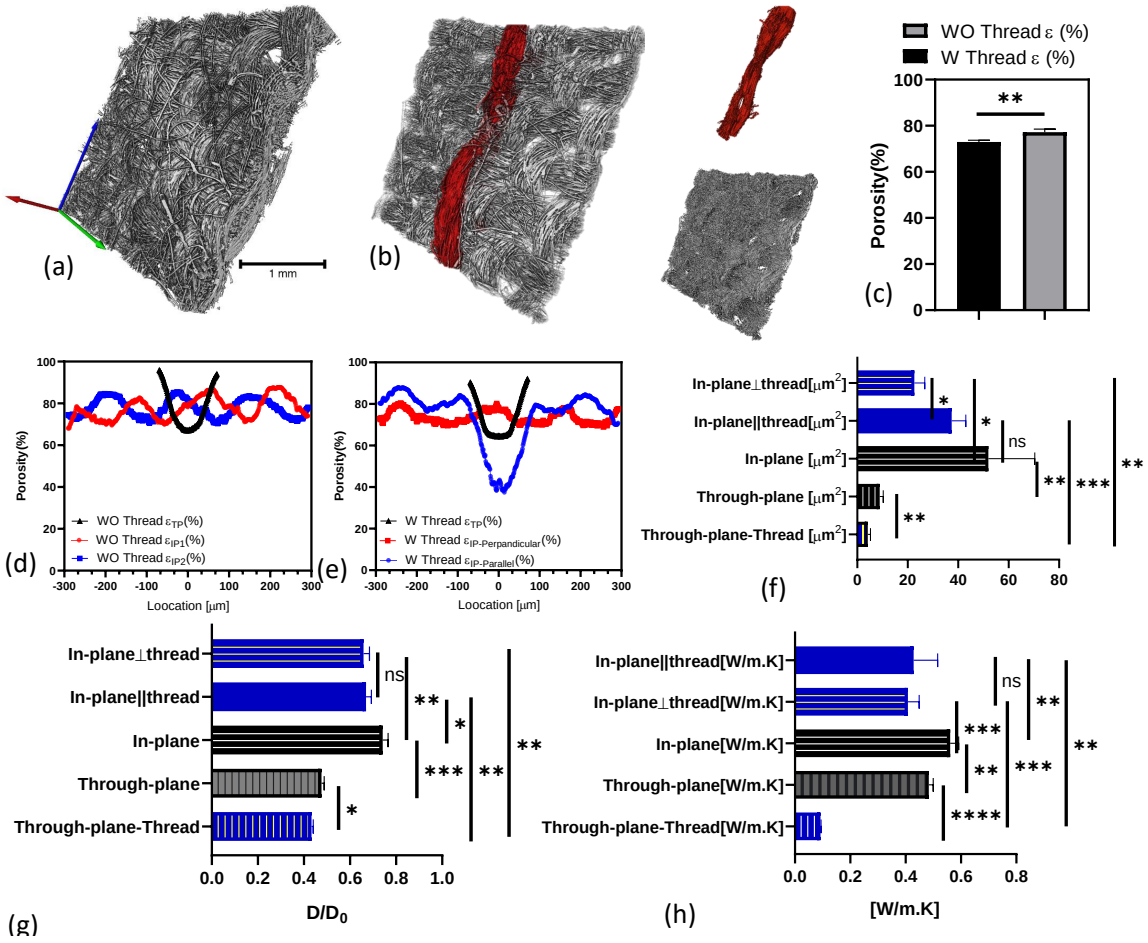

Figure 4.4: 3D microstructural analysis for evaluating transport properties. (a) X-μCT 3D image of pristine GDL and (b)with hydrophobic thread, thread and carbon cloth are segmented (scale bar is 1 mm). (c) Change in bulk porosity due to the existing thread. (d)Porosity distribution for pristine carbon cloth and (e) with hydrophilic thread. Analysis of the effect of thread on (f) diffusivity, (g) permeability and (h) thermal conductivity (Pristine carbon cloth is black and with thread is blue). Error bar represent SD (n = 3); $*p < 0.05$, $**p < 0.005$, $***p < 0.0005$ and $****p < 0.0001$.

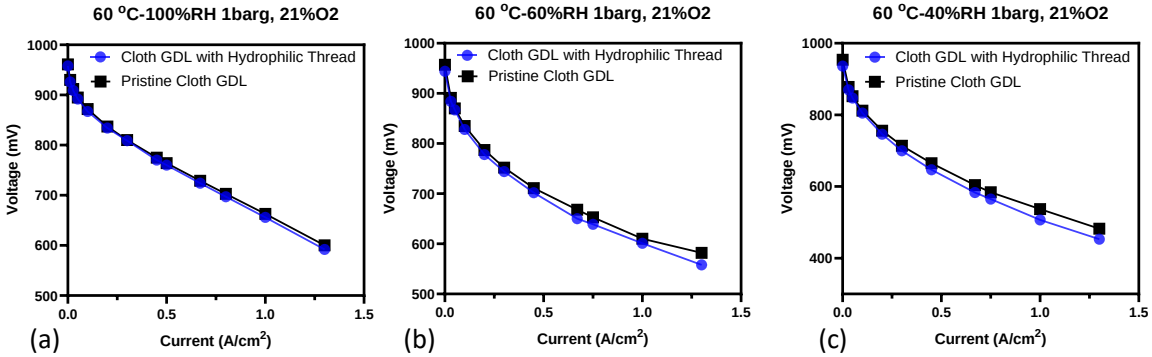

Figure 4.5: In-situ fuel cell testing for pristine carbon cloth GDL and cloth GDL with hydrophilic thread. The polarization curve under 60 °C and 21% O_2 for RH at (a) 100%, (b) 60%and (c) 40% RH

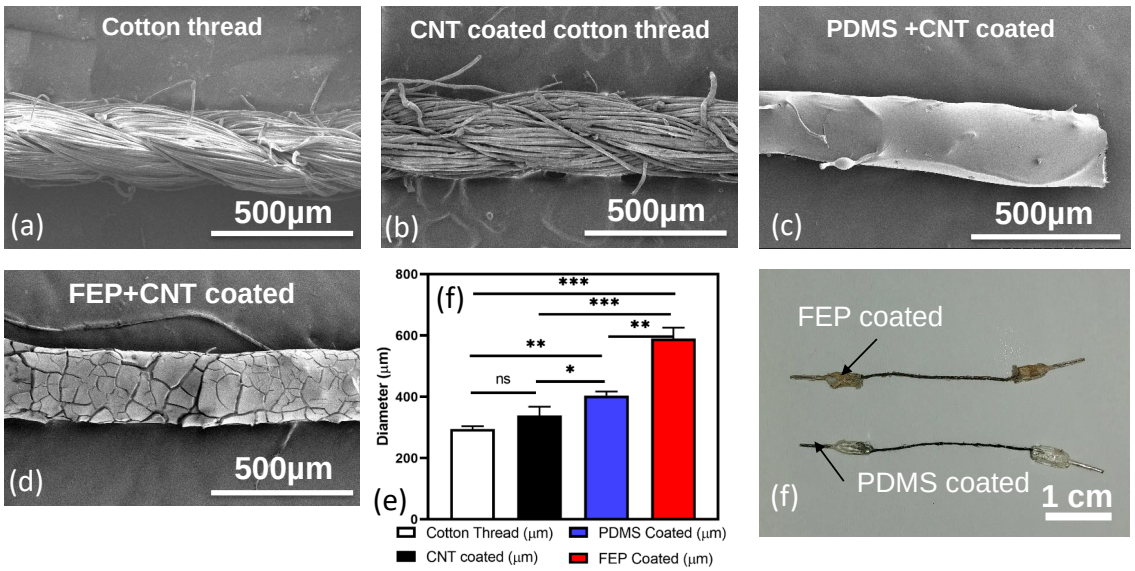

Figure 4.6: (a) Pristine cotton thread, (b) CNT coated, (c) CNT coated with PDMS and (d) CNT coated with FEP (scale bar 500 µm). (e) Change in diameter after different coatings. (f) Optical image of thread-based sensors. Error bar represent SD (n = 3); $*p < 0.05, **p < 0.005, ***p < 0.0005$.

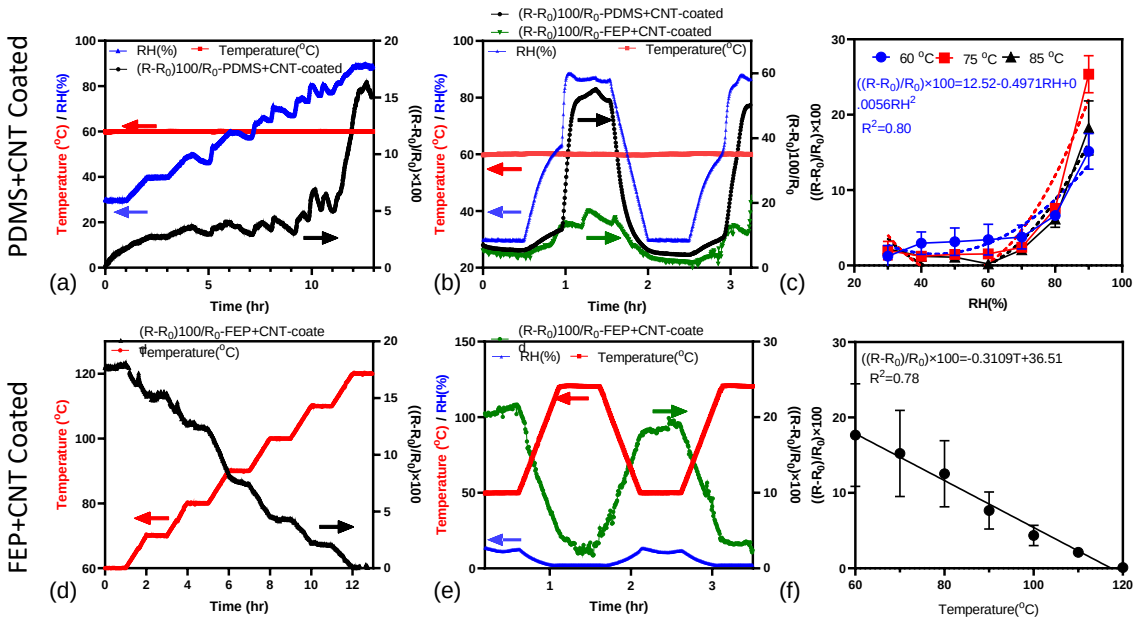

Figure 4.7: (a) Step wise response of the sensor between 30% to 90% RH changes. (b) Capturing the response of the sensor in changing RH values from 30% to 90%. (c) The sensor response for three different temperatures with varying RHs. (d) Step wise response of the sensor between 50°C to 120 °C. (e) Capturing the response of the sensor in changing temperature values from 60 °C to 120 °C. (f) The sensor response with varying temperatures. Error bar represent SD (n = 3).

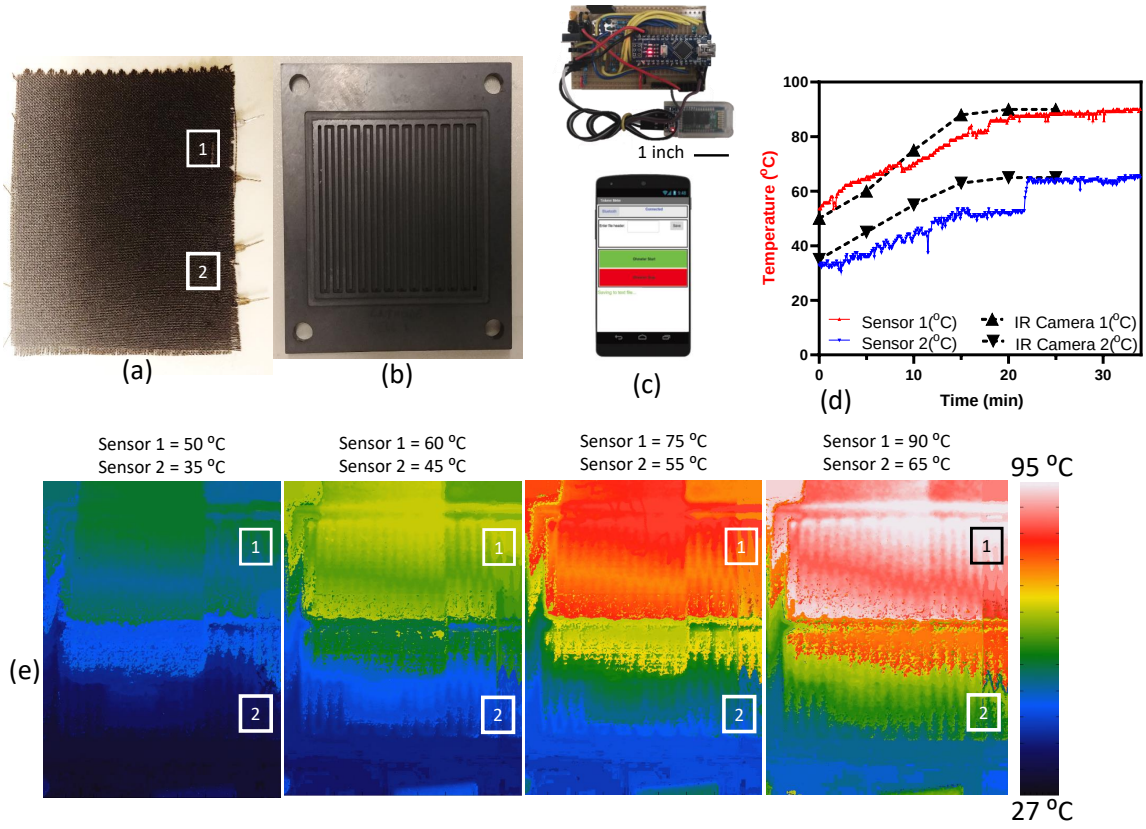

Figure 4.8: (a) carbon cloth GDL with two temperature sensors sewed and placed on (b) a flow field (c) A circuit board communicating with smart phone (d) Temperature monitoring via sensors (red and blue for locations 1 and 2 respectively) and black line via thermal camera. (e) Temperature map over half an hour of non-homogenous temperature distributions.

Chapter 5

A hybrid thread-based temperature and humidity sensor for continuous health monitoring

5.1 Abstract

The textile humidity and temperature sensors have a wide array of potential applications in clothing, management of wounds, and monitoring of patient health. Here, we illustrate the development of the textile-based humidity and temperature sensors, via a cost-effective and scalable dip-coating fabrication process. Cotton threads were coated in a functionalized multiwalled carbon nanotubes (fMWCNTs) suspension, and the resistance of CNT-coated thread is $\sim$20 $k\Omega/cm$ and with the durability of more than six months. The CNT-coated thread responds to both relative humidity (RH), and temperature changes were evaluated. We developed a process to mitigate the RH response by coating a hydrophobic polymer (FEP) via a dip-coating process on top of CNT-coated thread. The FEP+CNT-coated thread is a solo temperature sensor independent of RH showing linear resistance decrease by increasing temperature between (20 to 90 °C). In contrast, CNT-coated thread shows a response to both RH (i.e. a quadratic function of RH) and temperatures(i.e. linear response to temperature). CNT-coated thread and FEP+CNT-coated threads together can monitor both temperature and RH. The thread-based sensors did not show any negative impact on cell study and wound healing process in the animal model, which shows the promising application of these sensors in wearable biomonitoring.

5.2 Introduction

E-textile is a rapidly growing research field that converges textile technologies and wearable electronics for continuous health and wellness monitoring. Flexibility, combined with the ability to measure the level of various biological markers including pH, glucose, motion, temperature [124, 125, 126, 127] have led to the widespread application of e-textiles in digital health, sport, military applications [128, 129, 66, 130] and energy storage devices [122, 131, 132]. Successful applications of textile-based motion detector sensors have been demonstrated in several studies for posture monitoring, measuring vital health signals such as blood pressure, pulse rate, and respiration rate [110, 133]. Besides, Wang et al. [134] developed electrochemical fabrics that measure the level of glucose, pH and ions (i.e. K+ and Na+) in sweat by depositing active materials (e.g. glucose oxide and polyaniline (PANI)) and monitored human body response in real-time.

The ability to measure the humidity of the human environment, skin moisture, or sweat rate has the utmost importance in the continuous monitoring of human health and wellness. In the context of wound management, it is well-accepted that the healing process can be accelerated by keeping the wound moist6. Besides, bed-wetting and control humidity within clothing are other important applications [58]. Previous attempts for developing wearable RH sensors mainly relied on fabricating sensors on thin polymeric composite films [135, 136, 137, 138] or depositing carbon-based nanomaterials onto substrates (e.g. Kapton tape, cellulose paper) via drop-casting or dip-coating [61, 139, 140, 141]. Recently, a few studies transferred conventional humidity sensors onto textiles by weaving conductive yarns into electrodes [125, 59, 58] or screen printing electrodes onto fabrics [142]. Although these sensors display a major technological advancement in the field of e-textile and wearable sensors, challenges associated with the delamination of patterned sensors, the reliance of the sensor sensitivity on substrate wettability, and the dependence of the readings on the temperature limit the application of these sensors in continuous health monitoring [58, 143] since the effect of temperature on the RH response in the majority of studies were ignored.

Temperature sensing is essential for developing artificial skins, health monitoring systems and wearable devices that measure the performance of athletes [144, 145, 68]. Current commercial thermocouples and thermistors are not practical for health monitoring applications because they do not provide the required flexibility to be embedded

in clothing. Wearable electronics employ conductive metallic wires, carbon-based materials and polymeric materials to develop sensors that can be embedded in textiles for body temperature-monitoring [146, 147]. Notably, carbon- and graphene-based nanomaterials hold great potential for applications in temperature sensing because their electrical resistance is dependent on temperature [144, 147, 148, 149]. Excellent electrical properties of carbon nanotubes (CNTs) combined with their adaptability with various fabrication methods (e.g. screen printing, dip coating and 3D printing) have made CNTs attractive materials for creating temperature sensors on a wide range of substrates [144, 150]. To this end, Karimov et al. [148] developed temperature sensors from CNT film deposited on top of a paper substrate and characterized the resistance between 20 and 75 °C. The resistance of the film dropped approximately 20% within this range of temperatures. Honda et al. printed the mixture of poly(3,4-ethylenedioxythiophene):Poly(styrenesulfonate)(PEDOT:PSS) and CNTs on a polydimethylsiloxane (PDMS) substrate [144, 68]. This sensor fabrication method resulted in temperature sensors that operated in the range of 20 to 50 °C with a sensitivity of $\sim 0.61 \frac{\Delta R/R_0}{^\circ C}\%$. However, the integration of this sensor on textiles is the main challenge since film sensors cannot adapt to the irregular body surfaces and hinders the comfort in wearable applications. Thread-based temperature sensors offer a solution for embedding sensors in current textile fabrics without compromising the structure, design, or the ease of use of the textile. To this end, Mostafolu et al. [66] developed a thread-based temperature sensor by dip-coating cotton thread into a CNT ink and showed CNT-based sensors linear resistance change to temperature. However, majority of mentioned temperature sensors did not investigate the effect of RH on the sensor response.

Here, we report on developing thread-based humidity and temperature sensors, which exhibit high stability in various environmental and biological conditions. The sensors were made from CNT-infused cotton threads using roll-to-roll dipping approach, Although CNT-based temperature and humidity sensors were previously developed for biomonitoring [66, 58, 68, 144], the reciprocal effect of temperature and humidity on the performance of each sensor has been utterly neglected. Such reciprocal effects can be detrimental to the performance of the temperature and humidity sensors and can introduce significant errors in applications with high temperature and humidity fluctuations. To overcome this shortcoming, we coated the sensors with a thin layer of fluorinated ethylene propylene (FEP), which eliminates the effect of humidity on the temperature readings. These two sensors were then combined to

correct the effect of temperature on the humidity measurement. The biocompatibility of these sensors were analyzed through cytotoxicity and animal studies. The ease of fabrication, low material costs combined with the ability to integrate these sensors in textiles will pave a path towards designing wearable biosensors for continuous health monitoring.

5.3 Results and discussion

5.3.1 Fabrication and microstructure characterization of CNT-coated threads

The proposed process of fabricating thread-based sensors via a roll-to-roll method is illustrated in Figure 5.1(a). Prior to the coating step, the surface of the threads was treated with a corona discharge to remove the wax layer and promote the wettability of the thread by removing hydrophobic impurities on the surface [151, 152]. Threads were then sequentially dipped into a well-dispersed CNT ink bath, dried at 85 °C. Then, the CNT-coated thread dipped into an FEP bath, dried at 100 °C and sintered FEP on the thread at 300 °C. Functionalized multi-walled carbon nanotubes (fMWCNTs) were dispersed in distilled water with sodium dodecyl sulfate (SDS) as a surfactant, followed by tip sonication (Figure 5.1(b)).The dipping and drying process was repeated seven times to achieve a uniform coat. This dipping process led to the formation of a uniform layer of fMWCNTs onto the surface of threads (Figure 5.1(c) and (d)). The CNT-coated thread was flexible and sewn onto a piece of fabric (Figure 5.1(e)). Additionally, the CNT-coated thread was used to light-up a light-emitting diode (LED), as shown in Figure 5.1(f). Figure 5.1(g) and (h) show that the resistance of the CNT-coated thread was a function of both RH and temperature as CNTs are responsive to both RH and temperature of the environment. To eliminate the effect of RH on the temperature response, we coated the CNT-coated thread with a hydrophobic FEP suspension that uniformly covers the outer layer of the thread (Figure 5.1(i) and (j)). The RH response of the FEP+CNT-coated thread significantly reduced as shown in Figure 5.1(k). As a result, a thread-based temperature sensor independent of RH is developed, and the resistance of the thread in temperatures varied from 30 to 100 °C was monitored, and the resistance temperature curve shows a linear resistance decrease in that range.

To optimize the effect of the coating process on the quality of sensors, we system-

Table 5.1: Different ink compositions used for coating the threads.

	Concentration of fMWCNTs (mg/ml)	Concentration of SDS (mg/ml)
Ink 1	1	10
Ink 2	1.6	10
Ink 3	2	10
Ink 4	1.6	5
Ink 5	1.6	10
Ink 6	1.6	15

atically altered pertinent manufacturing parameters, including the concentration of the CNT-based ink, concentration of the surfactant, and the number of dipping steps while keeping the thread material unchanged. Scanning electron microscopy (SEM) images and the resistance of the manufactured conductive threads were used to evaluate the quality of the coating process. As illustrated in Figure 5.1(b), a CNT ink was developed by homogeneously dispersing fMWCNTs into distilled water with the addition of a surfactant, producing a uniform suspension in the aqueous solution. Sun et al. [153] quantitatively demonstrated a better CNT dispersion in water using SDS than five other surfactants (i.g. sodium dodecylbenzene sulfonate (SDBS), lithium dodecyl sulfate (LDS)), and the dispersion remained stable (without precipitation) over time, because surfactant-coated nanotubes generate strong electrostatic repulsion between them, and SDS shows a higher electrostatic repulsion compared to other alternatives. Furthermore, previous studies have shown that this ink can wet cotton fabrics10. Six different inks with varying SDS and fMWCNTs concentrations were developed to coat on cotton threads and evaluate the electrical conductivity. Inks 1-3 had different concentrations of fMWCNTs and constant SDS concentration, while inks 4-6 had different concentrations of SDS and constant fMWCNTs concentration, which is shown in Table 5.1.

Figure 5.2(a) shows the effect of the number of dipping and drying steps and a CNT concentration on the resistance of the sensors. Our results showed that increasing the number of dipping steps led to a substantial decrease in the electrical resistance of the sensors. It is worth noting that the electrical resistance reached a plateau for medium (1.6 mg/ml) and high (2.0 mg/ml) concentrations of fMWCNTs after six dipping and drying cycles (Figure 5.2(a)). However, the electrical resistance did not reach a plateau even after seven dipping and drying cycles for the low (1.0 mg/ml) concentration of fMWCNTs (Figure 5.2(a), inset). Additionally, increasing

the number of dipping and drying cycles improved the reproducibility of the sensors significantly, as evidenced by smaller error bars. We hypothesize that increasing the number of dipping and drying cycles has led to the infusion of more nanoparticles onto the surface and microporous structure of the threads, which in return reduced the air voids between the nanoparticles and enhanced the electrical conductivity of the coated layer.

The effect of the number of dipping and drying steps and an SDS concentration on the resistance of the sensors is shown in Figure 5.2(b). Low (5 mg/ml), medium (10 mg/ml) and high (15 mg/ml) concentrations of SDS shows the same resistance after four dipping and drying cycles. Besides, increasing the number of dipping and drying cycles improved the reproducibility of the coating, and after seven dipping and drying cycles, all three concentration converges to the same electrical resistance for the CNT-coated thread (Figure 5.2(b), inset). Then, 5 mg/ml SDS is enough of surfactant to coat CNT ink on the cotton thread.

To further confirm the effect of CNT concentration on the quality of the CNT layer on the threads, we obtained SEM images of pristine and coated threads with low (1.0 mg/ml), medium (1.6 mg/ml), and high (2.0 mg/ml) concentrations of CNT (Figure 5.3). A clear CNT attachment was observed on the surface of the cotton thread, Figure 5.3(b)-(d). Higher CNT concentrations in ink resulted in more accumulation of CNTs on the cotton thread. The CNT attachment is better shown in higher magnification images (with a scale bar of 1 µm). The outer layer of each filament of the thread was covered with CNTs. This result indicates that uniform CNT coating on the surface of the thread was achieved.

Furthermore, to evaluate the durability of the coating, the thread was sewn into a piece of cotton fabric. The resistance of the thread was measured in its unbent state, bent over a 10 mm cylinder, and bent over a 2 mm cylinder (Figure C.1). For these three configurations, the changes in the measured resistance was minimal, which shows that bending did not change the thread sensor response. Additionally, the CNT-coated thread resistance was monitored over a period of six months stored in a petri dish at room temperature (Figure C.2). The minimal change in resistance over time did not show any coating degradation.

5.3.2 Humidity Response of CNT-coated Thread

For the investigation into the CNT-coated thread response to RH, a series of experiments were performed to fully characterize the stability, sensitivity, hysteresis, and long-term RH response, which are essential characteristics of thread-based sensors. For the following experiments, three 4 cm-long cotton threads coated with CNT ink (1.6 mg/ml fMWCNTs and 10 mg/ml SDS formulation), were tested in a variety of different conditions in an environmental chamber.

A test was designed to modulate the RH from 30 to 90% RH with an interval of 10% RH increase at 25 °C. The resistance of the threads was monitored continuously via an in-house made board. The RH at each step was consistent for 30 minutes with a ramping time of 15 minutes. The thread resistance followed the RH changes as illustrated in Figure 5.4(a). The actual resistance of the thread in the test is drawn in Figure C.3. The gauge factor for RH sensitivity is $\frac{\Delta R}{\Delta(RH)} = 492\frac{\Omega}{RH}$ which shows substantial resistance changes to RH changes. A similar pattern of response was observed for two other replicates, which can be seen in the supplementary document (Figure C.3).

The experiment in Figure 5.4(a) was replicated at three different temperatures (25 °C, 50 °C and 75 °C). The summary of the data is shown in Figure 5.4(b). The thread response followed a quadratic function for all three temperatures and showed a higher sensitivity (i.e. 2% resistance change) in low RH regions (under 40% RH) at 25 °C, compared to 50 °C and 75 °C (i.e. 1% resistance change), a finding that is in line with literature [58]. The quadratic response of the CNT-coated thread to RH has a good fit at 25 °C ($R_{sq} = 0.99$) (See also Table C.1). One possible explanation of less sensitivity at a higher temperature may be that the amount of water is higher at the same RH, and higher water vapour concentration covers the CNTs and saturates outer layer of conductive layers at 50 °C and 75 °C.

The reversibility is one of the desired characteristics of mores sensors. In Figure 5.4(c), the RH was cycled between 30% and 90%. The thread resistance followed the pattern of RH in high and low values. This response showed good sensitivity to dynamic RH changes in a short period of time (on the order of seconds). At the beginning of the high RH region, a slight increase in resistance was seen, which may be due to the environmental chamber control system (as per the manufacturers manual, RH accuracy is within 2%). A similar pattern was observed for three replicates of the CNT-coated thread. Figure C.5 shows the dynamic response of threads in

different RH regions with fast RH variation, indicating that the response is fast (on the order of seconds), which is useful for wearable sensing applications. Another important characteristic of these threads is that the ability to produce the same response from high to low RH, and vice versa. Therefore, a hysteresis test was performed on the threads at 25 °C. The decreasing RH from 90% to 30% showed slightly higher resistance than increased RH from 30% to 90%, which is indicative of a small hysteresis effect (Figure 5.4(d)). A possible reason for this slight hysteresis may be due to the environmental chamber requiring more time to stabilize for changing RHs. Finally, to evaluate the long-term sensor response, the thread resistance was monitored for more than 5 hours at constant RH and temperature. Figure 5.4(e) shows a steady response in high and low RH at 25 °C. This steady signal proves that the resistance changes are due to environmental changes and not sensor degradation over time.

5.3.3 Temperature Response of CNT-coated Thread

We demonstrated that the CNT-coated threads showed a quadratic resistance increase to increasing RH. Here we examine the effect of temperature on the resistance of CNT-coated threads. W e analyzed the stability, sensitivity, hysteresis and long-term response of CNT-coated threads to temperature (Figure 5.5).

Three pieces of CNT-coated cotton threads with the length of 4 cm (coated with 1.6 mg/ml fMWCNTs and 10 mg/ml SDS) were placed in an environmental chamber, which was programmed to vary the temperature from 90 to 20 °C with an interval of 10 °C and a ramping rate of 0.67 °C/minutes at a constant RH of 30%. The temperature was kept constant at each step for 30 minutes. The thread resistance increased stepwise as the temperature dropped (Figure 5.5(a)), and Figure C.6). Our results suggested a linear variation of resistance with respect to temperature for the range of 20 to 90 °C. Furthermore, the gauge factor for the sensor is $\frac{\Delta R}{\Delta T} = 314 \frac{\Omega}{^{\circ}C}$ which provides good sensitivity to capture temperature changes Figure C.6). The same test was performed at RHs of 50% and 75%. For all constant three RHs, the thread resistance decreases linearly by increasing the temperature. The linear fitting function for all three RHs are drawn in Figure 5.5(b) in dashed lines, and Table C.2 has the resistance vs. temperature formula for all three constant RHs.

The temperature was changed in two extreme ends (25 °C and 90 °C) and cycled four times with 15 minutes constant temperature and 15 minutes ramping time.

Thread resistance followed temperature change, as shown in Figure 5.5(c). It shows that the resistance of the thread responds fast (in order of seconds) to temperature changes. However, keeping RH constant in fast temperature changes from 90 °C to 20 °C is not possible due to the limitation of the environmental chamber, and the RH was not constant for the duration of the test. The RH value increased from approximately 25% to 55%, and that caused the resistance of the thread was not horizontal at the constant temperature of 20 °C and 90 °C. This result is investigated further to show the CNT-coated thread response to RH and temperature simultaneously in section 5.3.4.

To evaluate the hysteresis effect, we systematically analyzed temperature response from high to low and low to high temperatures. Figure 5.5(d) shows that there is a hysteresis effect in the temperature response, due to the environmental chamber varying the RH for the duration of the test, as shown in Figure C.7. This experiment was performed from 20 °C to 90 °C and cooled from 90 °C to 20 °C at a supposedly constant RH; however, the RH rose by approximately 10%, which might be a reason for the hysteresis effect, also another possible explanation might be due to water accumulation around the thread. The other factor that might affect the hysteresis is the hygroscopic effect. Natural fibres expand when exposed to high humidity, and cotton thread expands and contracts while exposed to humidity changes [154]. Finally, the long-term response of the threads at high and low temperatures was characterized at RH 30% for both conditions. During the two-hour period, the thread resistance did not vary at constant conditions and a definite change was observed from high to low temperatures.

5.3.4 Investigating simultaneous RH and temperature effects on CNT-coated threads

As indicated in the previous two figure panels, the CNT-coated threads were responsive to both temperature and humidity. First, distilled water was sprayed over a sample thread while resistance was monitored. Upon spraying, the thread resistance increased suddenly, and it slowly decreased until reaching a dry condition. The sharp increase in resistance again indicates the fast response of the sensor to the change of humidity (Figure 5.6(a)). Second, to demonstrate the effect of applied heat on the thread response, a sample thread was heated with a commercial hairdryer. The resistance of thread dropped suddenly due to the heating, taking approximately 10

minutes to cool down and for the thread resistance to return to room temperature resistance, as shown in Figure 5.6(b). Supporting Videos 1 and 2 further show the response to humidity and heat.

Part of the results from the cycling temperature change was selected from Figure 5.5(c), to demonstrate the CNT-coated threads responsivity to both RH and temperature parameters. The forty 40 minutes of data were used to develop a polynomial fitting function of RH and temperature (Figure 5.7(a)). The polynomial fitting function (1) was obtained with a high level of confidence (95%), where T is temperature, RH is relative humidity, R is the resistance, and R_0 is the initial resistance.

$$\frac{(R-R_0)}{R_0} \times 100 = 22.21 - 0.2332 \times T + 0.05676 \times RH + 6.9339 \times 10^{-5} \times T^2 \\ \text{- } 0.002091 \times RH \times T - 0.0001066 \times RH^2 + 1.855 \times 10^{-5} \times RH^2 \times T + 1.182 \times 10^{-5} \times \\ RH \times T^2 + 4.0510^{-5} \times RH^3 \tag{5.1}$$

The 3D surface of the equation (1) is shown in Figure 5.7(b). This fitting function was used to predict the response of the CNT-coated threads for temperature and RH cycles (Figure 5.7(c)). This test proves that CNT-coated threads are a function of both parameters and that their use in an environment where both parameters vary, will result in substantial errors. Therefore, we subsequently developed a coating that can isolate temperature response from RH response with the CNT-coated threads.

5.3.5 Developing thread-based temperature sensor

The thread-based sensor that is exclusively responsive to the temperature needs a coating to mitigate the RH response while ensuring the flexible characteristics. Hydrophobic coatings are good candidates for this purpose, as RH response must be removed from the CNT-coated thread. FEP is a hydrophobic polymer that has been used for increasing the hydrophobicity of surfaces and porous media [27, 5]. Also, PDMS is a widely used polymer for coating substrates, as seen in previous studies [66, 56]. We coated threads with both polymers using the dipping and drying process, and achieved a uniform coat of FEP and PDMS on threads, as shown in the SEM images in Figure 5.8(a) and 5.8(b). In order to evaluate the RH response of PDMS and FEP coating, three samples of each coating were prepared and tested with cycled RH, at room temperature. The test indicated that FEP mitigated the RH response

completely; the resistance change was within 5% when RH was varied between 30% and 90%; however, the thread without any coating showed an instant response to RH change. On the other hand, PDMS coatings delayed and decreased RH response, but did not remove the response as completely, as shown in Figure 5.8(c). For a short term test, PDMS may work as a coating to cancel RH as used previously in ref42,43, but, to effectively mitigate the RH response, FEP showed better workability over 6 hours cycling RH at a constant temperature. In addition, a test performed for the proof-of-concept for RH response of FEP coated thread where water was sprayed over CNT-coated thread with and without FEP coatings (see Supplementary Video 3). The instant response to water spray was observed for non-coated threads; however, there was no significant change of resistance for FEP+CNT-coated threads for over 8 minutes (Figure 5.8(d) and 5.8(e)).

The temperature response of three thread types (CNT-coated, FEP+CNT-coated, and PDMS+CNT-coated) was characterized. The sensitivity of the PDMS+CNT-coated thread was higher than FEP+CNT-coated, and CNT-coated, as shown in Figure 5.8(f). The reason for higher sensitivity in the PDMS- and FEP-CNT-coated threads may be due to the thermal expansion of the coating, which results in better CNT connections and reduces the resistance of the thread with increasing temperature. We concluded that FEP+CNT-coated thread is a thread-based temperature sensor that shows a minimal response to RH while maintaining the temperature sensitivity.

A test was designed to control and monitor temperature by combining heating threads (cotton threads coated in commercial silver ink) and the aforementioned thread-based temperature sensor. As shown in Figure 5.8(g), a heating thread was twisted around the thread-based temperature sensor (FEP+CNT-coated thread) and monitored using a thermal camera. The targeted temperature was 30 °C, and the surrounding temperature was 20 °C. The heating thread climbed to the target temperature, as verified by the thermal camera (Figure 5.8(h) and (i)) and Supplementary Video S4). The temperature remained within 3 °C of the target value. For 12 cycles, a small drift was observed in the initial base value of the temperature sensor. After 12 cycles, a 4 $k\Omega$ change in base reading was observed, representing just 1.4% drift. The response to a 10 °C temperature cycle was 7.8$\pm$0.9 $k\Omega$, or 2.7%. To negate the effects of this drift, the controller was programmed to recalibrate temperature after every cycle. This test was performed on three samples, each of which demonstrated a similar trend (Supplementary Figure C.8).

5.3.6 Evaluation of the biocompatibility of the thread-based sensors

Textile-based sensors for monitoring human activity and developing smart wound dressing require an investigation into cytotoxicity and biosafety. In order to analyze the cytotoxicity of the temperature sensor (FEP+CNT-coated thread) and the humidity sensor (CNT-coated thread), cell viability was performed. The relative metabolic activity of HaCaT (Cultured Human Keratinocytes) and fibroblast cells were measured using PrestoBlue reagent. The results showed that the FEP+CNT-threads did not affect the viability of both cells used in this study (Figure 5.9(a and b)) after 7 days of culture. Overall, the viability of cells remained above 85%. Similar results were reported by others in previous studies [155, 156, 143, 157, 158].

We further evaluated the biocompatibility of the sensors for an application in wound monitoring in a pilot in vivo study. To this end, we embedded the sensors in PDMS flexible film to create a smart dressing capable measuring the moisture and temperature in wounds . The level of moisture and temperature of wound have a critical role in wound healing process. Keeping the interface between a wound and an applied dressing moist is taken into account for effective wound healing. Furthermore, It has been shown that whenever a wound loses its moisture, the temperature of the wound drop as well. The cells, proteins and enzymes function best at normal body temperature, around 37 °C. When wound temperature drops by as little as 2 °C, healing procedure can slow down or even stop . The patch consisted of two separate electrode arrays making contact with the skin (Figure 5.9(c)). To investigate the biocompatibility of the sensors and the progress of cutaneous wound healing, the wound contraction of mice was quantified for all groups at day 7, post-injury. As can be seen from Figure 5.9(d) and (e), wound contraction with and without sensors measured 25.94±3.01% and 24.9±2.82%, respectively ($p > 0.05$, no significant difference). However, commercial wound dressing (Mepitel®) treated group lead to 30.41±1.31% wound closure, a finding that was significantly higher than the wound closures observed in other groups ($p* < 0.05$).

To further distinguish the quality of regenerated skin in the defects among the three groups, in the early stage of wound healing (after 7 days), histopathological staining and sectioning with Hematoxylin and Eosin (H&E) and Masson's trichrome (MT) was performed. Figure 5.9(f) shows the H&E and MT staining results for wounds in the three different groups 7 days, post-injury. Our results showed that

the control group without dressing was not completely repaired, had dermis damage with poor structure, unarranged collagen fibers along with an area of connective tissue depletion (yellow arrows), and high inflammatory cell infiltration. However, wounds covered with sensors embedded in PDMS showed better re-epithelization and more new tissue formation, blood vessels formation, and well-organized fibroblastic cells in subcutaneous which indicates that the sensors did not increase foreign body response. Similar results have been reported by other studies, that show PDMS-based wound dressings accelerated wound healing via enhancement of the re-epithelialization and granulation tissue formation. No obvious sign of inflammatory response was observed for wounds with sensors, which indicates that the sensors did not increase foreign body response. Similar results have been reported by other studies, that show PDMS-based wound dressings accelerated wound healing via enhancement of the re-epithelialization and granulation tissue formation [159, 160]. The group that was treated with Mepitel®showed a similar level of skin regeneration in terms of tissue formation and epidermis generation, compared to the sensor groups. The majority of skin regeneration depends on the collagen production; since collagen is the main skin extracellular matrix (ECM) component [161]. Therefore, we performed MT staining to evaluate the advancement of collagen deposition during skin regeneration. In MT staining, collagen was stained blue, whereas the muscles, epidermis, sebaceous glands, and blood vessels were stained red. According to the Figure 5.9(f), collagen deposition clearly increased in Mepitel®and sensor treated groups, when compared to the control group. Moreover, the collagen fibers in the Mepitel®and sensor treated groups were in the form of well-arranged bundles, more mature, and the regenerated dermis layer was more similar to the normal skin. The control group displayed the least amount of mature collagen formation among all groups. In addition, the sensors resistances were monitored and showed no significant change over healthy wound (Figure C.9).

5.4 Conclusions

We developed textile-based RH and temperature sensors, via a cost-effective and scalable dip-coating fabrication process. The commercially available cotton threads were coated with fMWCNTs using simple dipping and drying process. The resulting uniform coating, combined with its durability (over 6 months), proved the good adhesion of CNTs onto the cotton substrate. Fast responses to RH and temperature

changes, combined with excellent measurement reversibility (RH from 30 to 80%, temperature 20 to 90 °C), were achieved. This study showed that CNT-coated threads cannot effectively be used as a sensor in an environment where both temperature and humidity are varying. We mitigated the RH response by coating the CNT-coated thread with a hydrophobic coating (FEP polymer) via a dip coating process. The FEP+CNT-coated thread was responsive to temperature and independent of RH. The combination of CNT-coated thread and FEP+CNT-coated threads can monitor both temperature and humidity in textiles. Furthermore, the cytotoxicity and biosafety of the thread-based sensors were evaluated, showing that the FEP+CNT-coated threads induced no negative effect in vitro and on the in vivo wound healing process in a murine wound model. We demonstrated an acceptable resistance response for a wide range of RH and temperatures, that covers a spectrum of versatile uses. These novel textile sensors have a wide array of potential applications, from monitoring humidity and temperature in clothing, wound healing monitoring, human sweat monitoring, and patient incontinence.

5.5 Experimental section

5.5.1 Preface

The experimental part of this chapter was performed as follow: I was responsible for CNT ink perpetration, coating process, the experimental setup of temperature and RH measurement, data analysis and writing the article. Lucas Karperian performed thread-based heating and cooling cycle using a thread-based temperature sensor. Maryam Jahanshahi performed cell cytotoxicity and Viability analysis. Zhina Hadisi performed animal studies.

Materials: fluorinated ethylene propylene (FEP) (FEPD121 DuPont 55% solids) was purchased from Fuelcell Earth, functionalized multiwalled carbon nanotubes (fMWCNT) and sodium dodecyl sulfate (SDS) were purchased from Sigma-Aldrich.

Preparation of CNT Ink: SDS (Sigma-Aldrich) was dissolved in distilled water with a concentration of 10 mg/ml. Then, fMWCNTs with concentration of 1.6 mg/ml (Sigma-Aldrich) were dispersed in distilled water by 1-minute probe sonication to achieve a well-dispersed solution. The same procedure was done for other concentrations of fMWCNTs and SDSs (1 and 2 mg/ml fMWCNTs, and 5 and 15 mg/ml SDS).

Preparation of CNT-coated Cotton Thread: Commercial cotton threads were corona discharged for one minute on both sides. Then, they were dipped into the CNT ink for one minute and were dried in a vacuum oven at 85 °C for half an hour in each dipping. The dipping and drying process was repeated in order to achieve the same resistance per centimetre in a subsequent dipping (7 times was enough for cotton thread).

Coating FEP on CNT-coated Thread: First the CNT-coated thread was dipped into 55% FEP solution. The coated thread was dried at 100 °C on a hot plate for 5 minutes. Then, it was heated to 300 °C to sinter FEP around the thread.

SEM Imaging: The SEM was performed using Hitachi S-4800N. False colouring was performed to distinguish between the cotton substrate and CNTs on the thread.

Resistance Measurement: The resistance was measured with an in-house made circuit. The circuit is used in ref. [162]. The board was tested with the Fluka 87V multimeter and calibrated for the range of working resistances. In the environmental chamber, the resistance of threads was measured every 20 seconds for a test more than an hour long.

Humidity and Temperature Control: The coated threads were tested inside the environmental chamber. The humidity and temperature were controlled by the environmental chamber (TESTEQUATY Model 123H). In each step, temperature and humidity were remained constant for half an hour to reach a stable state. Temperature and humidity were captured every 20 seconds.

Thread-based Heating and Cooling Cycle Combined with Temperature Control: Heating threads were fabricated by coating silver ink on threads, producing highly conductive elements. Silver ink was procured from Engineered Conductive Materials, and the apparatus was controlled with an Adafruit Feather M0 microcontroller. The thread-based temperature sensor was wound around the heating thread, coated with PDMS to produce and electrically insulating layer preventing interference from the current flowing through the heating element. A proportional-integral-derivative control system (PID) was implemented to establish effective control with rapid response time, allowing a target temperature to be set such that the temperature produced would reach that threshold quickly and without overshooting. Heating was provided using the pulse width modulator (PWM) on the Adafruit microcontroller to control the voltage delivered through the heating thread, adjusted by the PID. The system was then tested by running 12 cycles of heating and cooling back at room temperature for three replicates. Upon reaching the threshold temperature,

set to 33 °C, the control system kept the temperature steady for 30 seconds before deactivating the heating element. The temperature measurements were verified using a Seek Thermal camera, allowing real time measurement of the temperature being measured.

Cell Cytotoxicity and Viability Analysis: To study the effect of CNT-coated and FEP+CNT-coated threads on cell viability, immortalized human keratinocytes (HaCaTs, Addexbio, USA) and human fibroblast were used. HaCaTs and fibroblasts were seeded in 12-well cell culture plates with the seeding density of 30,000 and 20,000 cell/cm2, respectively using Dulbecco's Modified Eagle Media (DMEM, Gibco™ by Life Technologies™, USA) supplemented with 10% fetal bovine serum (Gibco™ by Life Technologies™, USA). After 24 hours of incubation at 37 °C in 5% CO2, the media of the wells were refreshed. Subsequently, 1 cm of CNT-coated and FEP+CNT-coated threads were individually placed into cell inserts in the wells to be in direct contact with the cell culture media. Afterward, control samples and samples with CNT-coated and FEP+CNT-coated threads were incubated at 37 °C in 5% CO2. Then, the samples were incubated with media containing PrestoBlue reagent (Invitrogen, USA) with 9:1 ratio for 45 minutes at 37 °C on days 1, 4, and 7. Immediately after incubation, 100 µl of supernatant was collected from each well and the fluorescence intensity was measured at excitation wavelengths of 560 nm and emission of 590 nm using a microplate reader (Infinite M Nano, Tecan, Switzerland). Relative viability was calculated by normalizing the measured intensity at each condition with respect to the control at each time point.

Animal study; (1) Induction of full-thickness wound: Six-week-old BALB/c mice (male, 20–30 g) were obtained from Jackson laboratories and acclimatized for one week before experiments. All animal procedures were performed following the policies and procedures of the Animal Care Committee at the University of Victoria. All mice were anesthetized with inhalation isoflurane (2%), and then the dorsal surface of animals was shaved by clippers and dried. Two parallel wounds with a diameter of 6 mm inducted using biopsy punch (Integra miltex®). The wound size was photographed by a camera (1). Next, the mice were randomly divided in three groups as follows: No-treatment (negative control), wounds treated with Mepitel®(positive control) and wounds covered with thread-based sensors embedded in PDMS. After 7 days of post-injury, the mice were euthanized by cervical dislocation, and the wound dressings were removed, and the amounts of wound contraction was calculated as follows (2): Wound closure (%) $= (A_0 - A_t)/A_t \times 100$ where, A_0 and A_t are the initial

wound area and the wound area at time t, respectively.

Animal Study; (2) Histopathological staining: Full-thickness wound tissues for all three groups were collected on day 7 and fixed in buffered formalin (10%). Fixed tissues transferred to 30% sucrose solution prior to slicing. 4 µm frozen sections were collected using a Leica CM1850 UV crytostat (Leica Biosystems, Concord, ON, Canada). Tissue sections were pretreated with Bouin's Solution (Sigma-Aldrich HT10132-1L) for 15 min at 56 °C and then stained with Hematoxylin and Eosin (H&E). Collagen formation was evaluated by Masson's trichrome (MT) staining according to manufacturer's instructions (Sigma-Aldrich). Finally, the stained sections were observed under a light microscope (Olympus BX51).

All procedures involving animals were performed following the policies and procedures determined by the Animal Care Committee at the University of Victoria (Protocol number: 2018-021(1)) C.1.

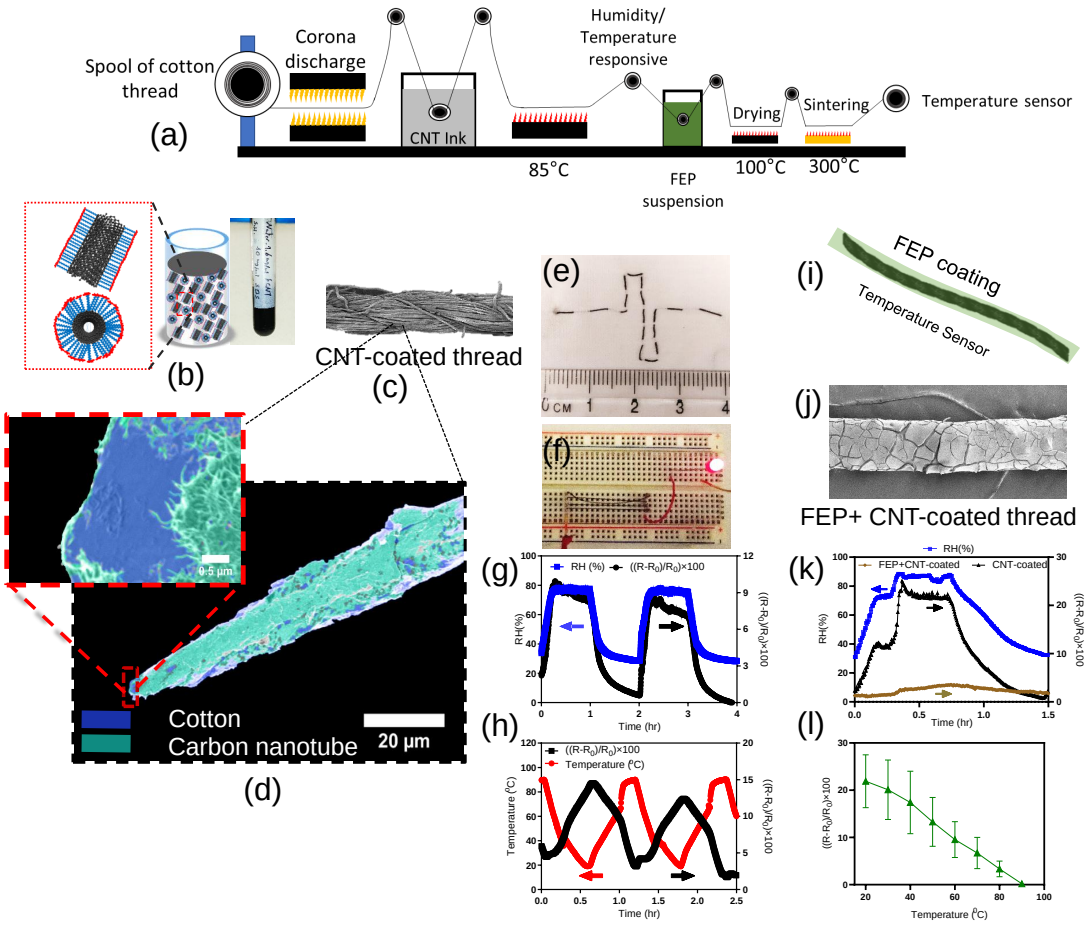

Figure 5.1: **Fabrication and characterization of thread-based RH and temperature sensors.**(a) The roll-to-roll process of coating a commodity thread via a CNT ink and FEP insulating layer. (b) A uniform CNT ink developed by suspending fMWCNTs via SDS in distilled water. (c) SEM image of CNT wrapped around the cotton thread and (d) observation of well-attached CNTs on a single cotton filament. (e) A flexible CNT-coated thread sewn in cotton fabric and (f) used to connect an LED in a circuit. (g) Response to RH and (h) temperature changes. (i) Schematic of FEP+CNT-coated thread and (j) SEM image of FEP+CNT-coated thread. (k) The RH response was mitigated via FEP coating for a wide range of RH. (l) A linear decrease in thread resistance with increasing temperature, showing the thread-based temperature sensor independent of RH.

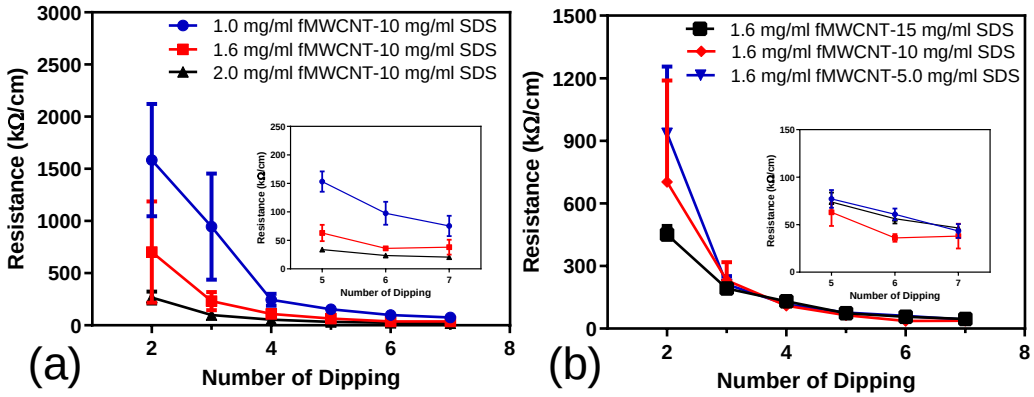

Figure 5.2: **Effect of the ink composition and dipping steps on the resistance of the CNT-coated thread.**(a) Dependence of electrical resistance on the number of coating, based on the variation of CNT concentrations (inset: resistance vs. the number of dipping from 5 to 7) and (b) SDS concentration(inset: resistance vs. the number of dipping from 5 to 7). Error bars indicate the standard deviation of triplicates (n=3).

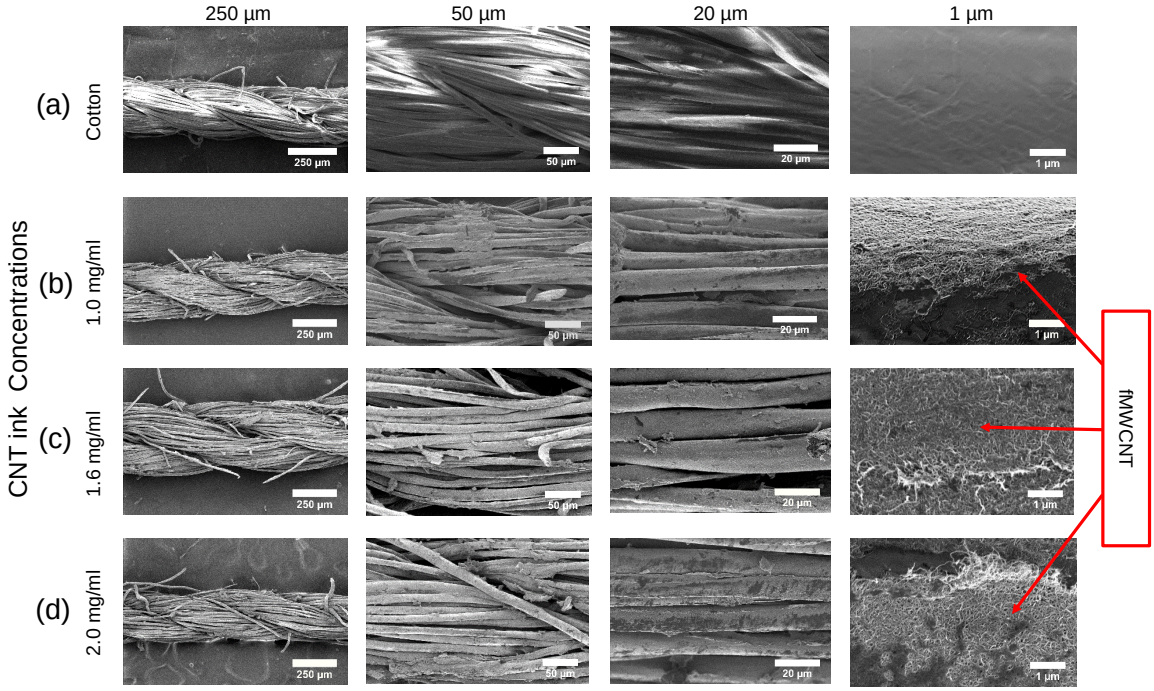

Figure 5.3: **Scanning electron microscopy (SEM) images of coated threads.** (a) cotton thread, coated with (b) 1 mg/ml fMWCNTs, (c) 1.6 mg/ml fMWCNTs and (d) 2mg/ml fMWCNTs at four different magnifications.

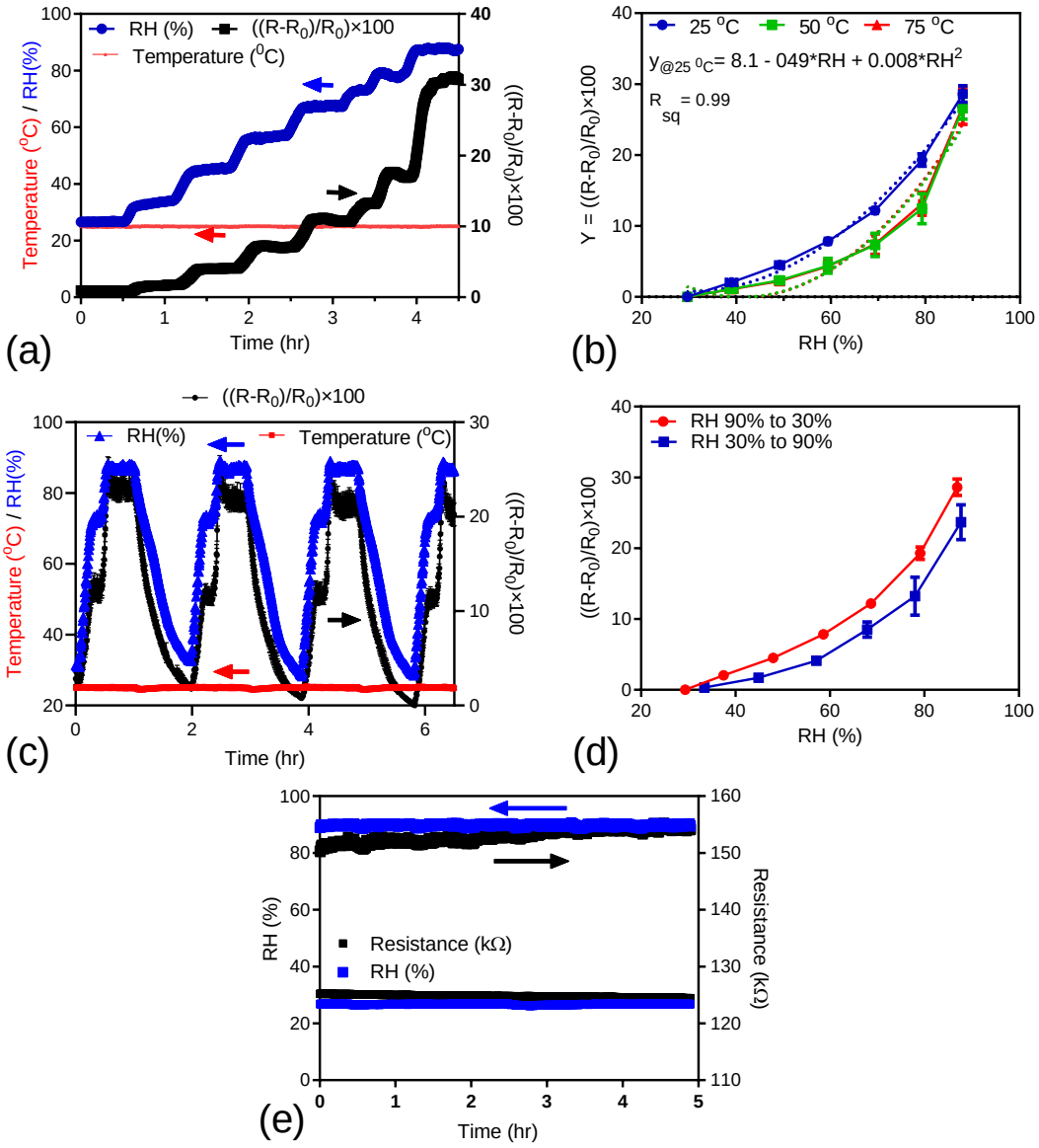

Figure 5.4: **Characterization of the RH response of the CNT-coated thread** (4 cm-long cotton threads coated with 1.6 mg/ml fMWCNTs and 10 mg/ml SDS). (a) Stepwise response to RH increase (Ramp time 15 min, soak time 30 min, temperature 25 °C). (b) Variation in the electrical resistance at three different temperatures (25, 50 and 75 °C) (the dotted lines are the fitted functions at three temperatures). (c) Repeatability test of the humidity sensor, humidity varied between 30% and 90% at 25 °C. (d) The hysteresis effect of the response from 30% to 90% and on return from 90% to 30%. (e) Steady response in high and low humidity for 5 hours (temperature 25 °C). Error bars indicate the standard deviation of triplicates (n=3).

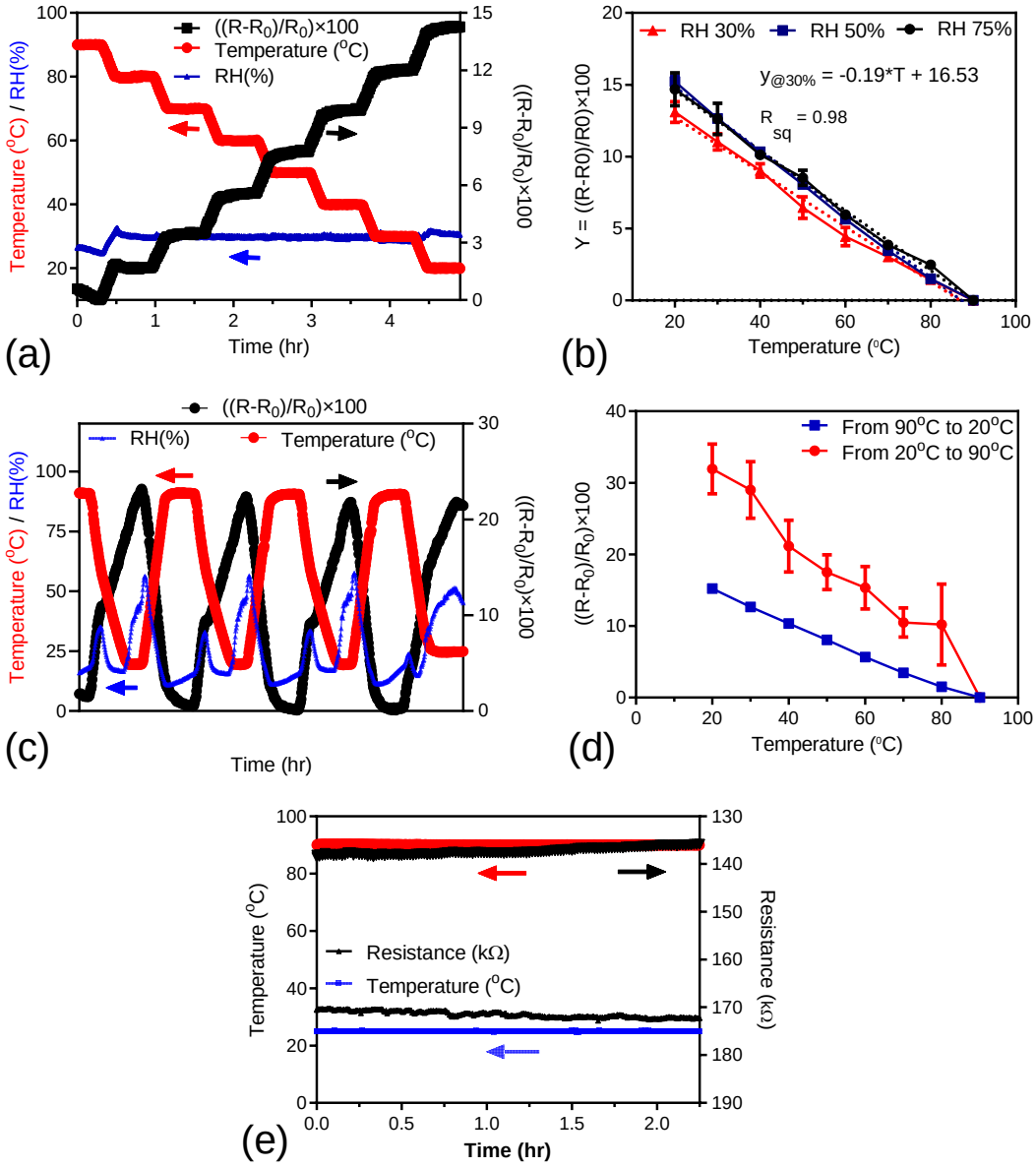

Figure 5.5: **Characterization of the temperature response of the CNT-coated thread** (4 cm-long cotton thread coated with 1.6 mg/ml fMWCNTs and 10 mg/ml SDS). (a) Stepwise response to temperature decrease (ramp time 10 min, soak time 30 min, RH 30%). (b) Variation in the electrical resistance at three different RH (30, 50 and 75%). (c) Repeatability test, changing temperature between 25 °C and 90 °C at approximately 30% RH. (d) Hysteresis effect of the response from 90 °C to 20 °C and return. (e) Steady response at high and low temperature for over two, at approximately 30% RH. Error bars indicate standard deviation of triplicates (n=3).

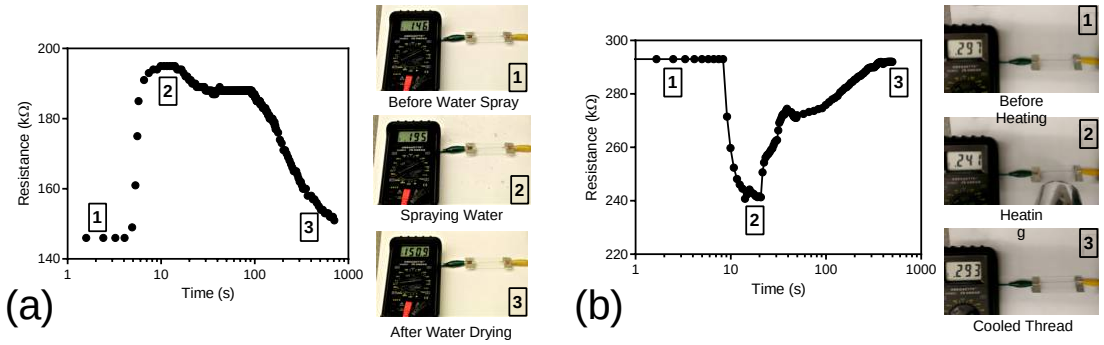

Figure 5.6: **The resistance response of the CNT-coated threads.** (4 cm-long cotton thread coated with 1.6 mg/ml and fMWCNTs and10 mg/ml SDS) to (a) water spray and (b) blown hot air.

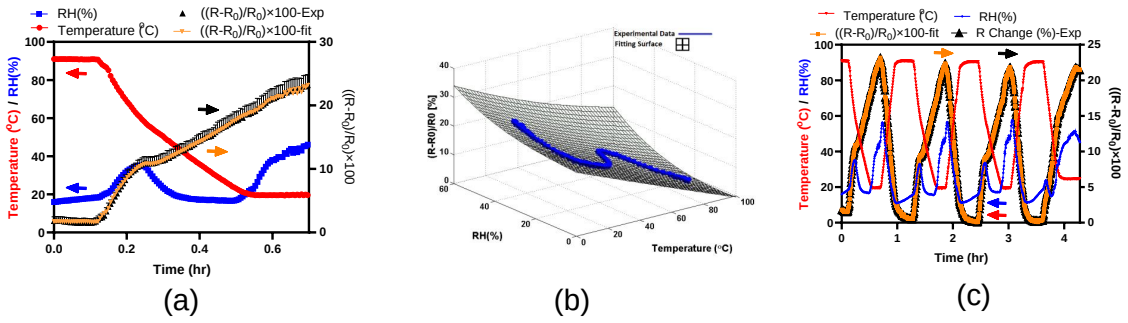

Figure 5.7: **Generating a response function of CNT-coated thread to both temperature and RH.** (a) Fitting function of CNT-coated thread and experimental data was shown for first 40 minutes of the test. (b) Generated surface based on the fitting function and experimental data (blue line). (c) The prediction of CNT-coated thread response based on fitting function.

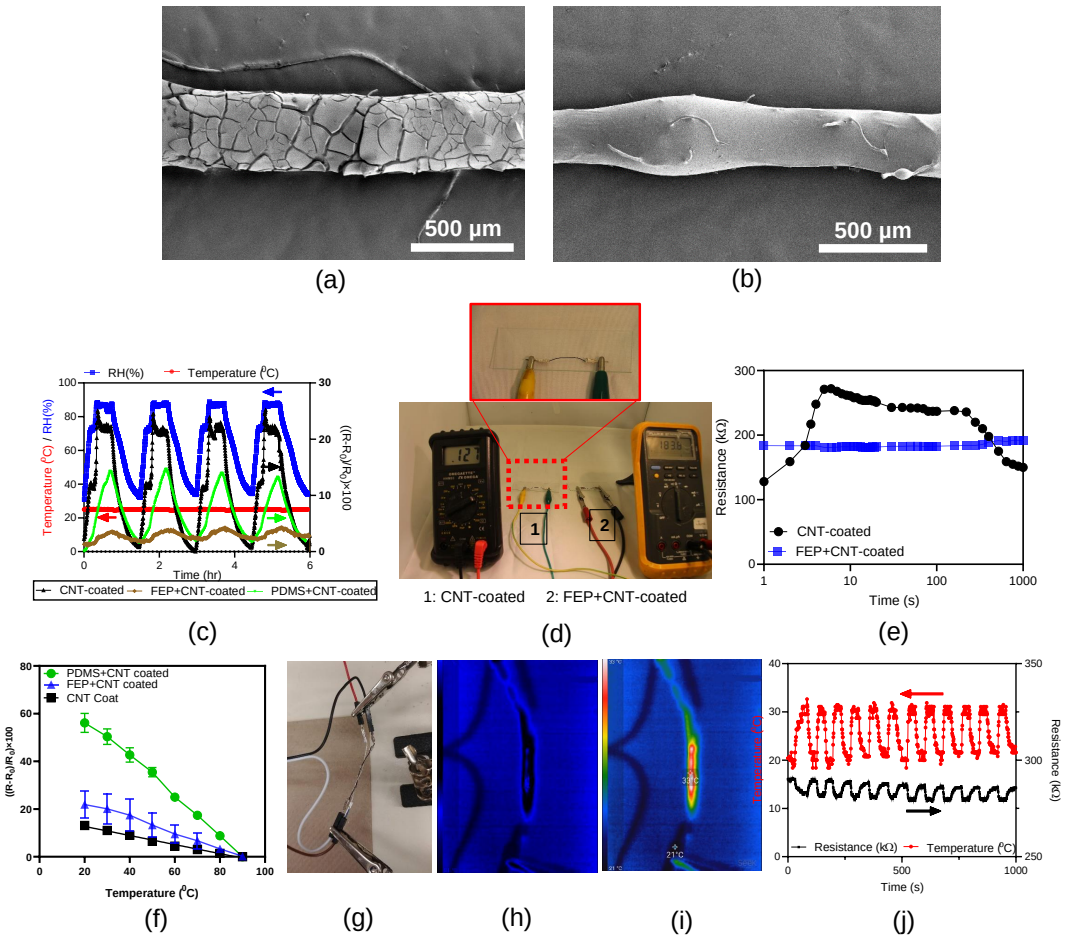

Figure 5.8: **Characterizing thread-based temperature sensor independent of RH.** SEM image of (a) FEP+CNT-coated and (b) PDMS+CNT-coated thread. (c) Cycling RH and monitoring thread resistance without coating, with FEP and with PDMS coating. (d) Water sprayed over FEP+CNT-coated thread and CNT-coated thread and (e) monitoring resistance of the CNT-coated thread rises and return to the base value, but FEP+CNT-coated thread did not show any response to water spray (supplementary video S3). (f) Temperature response of CNT-coated thread without coating, with FEP and with PDMS coating. (g) Wrapping heating thread around FEP+CNT-coated thread and monitoring temperature via thermal camera in (h) surrounding temperature (20 °C) and (i) targeted temperature (32 °C). (j) Temperature monitoring via thread-based temperature sensor and accordingly resistance of the thread in cycling heating of the thread. Error bars indicate standard deviation of triplicates (n=3).

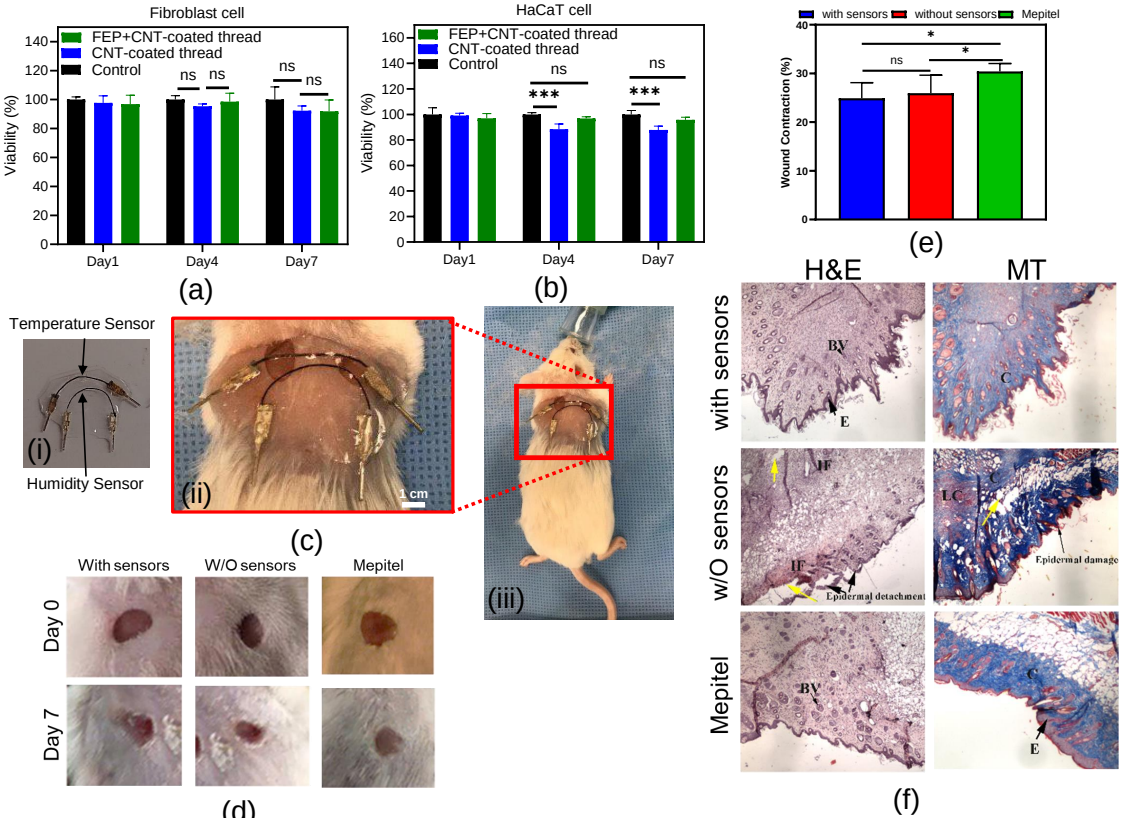

Figure 5.9: **Evaluation of the biocompatibility of thread-based sensors**. Cell viability study for (a) fibroblast and (b) HaCaT cells. (c) Attachment of the sensors (CNT-coated and CNT+FEP-coated) on mouse wounds. (d) Wound contraction for three groups: with sensors, without sensors, and with Mepitel®dressing. (e) Quantitative analysis of contraction at day 7. (f) H&E and MT evaluation of three groups, showing no negative effect was observed for wounds with thread-based sensors, compared to without treatment and with Mepitel®dressing groups. Error bars indicate standard deviation of triplicates (n=3); *ns = not significant, $*p < 0.05, **p < 0.005, ***p < 0.0005 and ****p < 0.0001$

Chapter 6

Conclusions and future work

This thesis describes (1) innovative approaches for characterizing water transport and conductivity of textile electrode of PEMFCs, (2) the development of integrated thread-based systems for water management and continuous monitoring in PEMFCs, and (3) novel thread-based RH and temperature sensors for wearable biomonitoring, each of which is described in Chapter 3 to 5 in details. In the following section a summary of findings, contributions and future work for each component are presented.

6.1 Woven gas diffusion layer for polymer electrolyte membrane fuel cells: liquid water transport and conductivity trade-offs

Chapter 3 presents the experimental study investigating the water transport in woven GDL under non-uniform compression. Additionally, the effect of hydrophobic coating on the through-plane electrical, and thermal conductivity was assessed.

6.1.1 Summary of findings

1. Ex-situ water visualization shows that hydrophobic coating causes water transport in the in-plane direction, utilizes more pores than non-coated GDL, and increases the water breakthrough pressure.

2. Through-plane electrical conductivity of woven GDLs with different hydrophobic loading (0, 30 and 55 wt% FEP) was investigated and showing the electri-

cal conductivity decreases linearly by increasing the hydrophobic loading. In addition, the GDL thickness increases by increasing the hydrophobic loading concentration.

3. The highest through-plane thermal conductivity is obtained at 30 wt% FEP loading and decreases by increasing FEP loading to 55 wt%.

6.1.2 Contributions

1. The hydrophobic coating improves the in-plane water transport using more pores within woven GDLs compared to pristine samples.

2. An optimum thermal conductivity value was obtained at 30 wt% FEP loading, while electrical conductivity decreases linearly by increasing the FEP loading.

3. There is a trade-off between better water transport and conductivity of GDLs while using the hydrophobic coating.

6.1.3 Recommendations for Future Works

1. *Performing water transport and conductivity analysis under temperature and humidity conditions corresponding to operating fuel cell conditions.* This study addresses the effect of compression and hydrophobic loading at room temperature. However, in elevated temperature (e.g. 80∼90 °C), water transport might follow different patterns. In addition, electrical conductivity and thermal conductivity were also measured at room temperature. Investigating the effect of temperature on the effective thermal and electrical conductivity will result in a more accurate estimation of GDL properties.

2. *Investigating thermal and electrical conductivity under saturated GDL conditions.* In this study, electrical and thermal conductivity were analyzed in dry conditions. However, in an operating fuel cell, water accumulates in GDL pores and alters the effective conductive properties. The effect of water saturation may have a significant effect on thermal conductivity since air is replaced by water with higher thermal conductivity.

3. *Analyzing the effect of hydrophobic coating drying process on water transport and conductivity.* This study investigated the fast drying (i.e. oven) for sinter-

ing hydrophobic coating on GDLs. It showed in previous work that hydrophobic distribution is directly related to the speed of drying. The effect of drying hydrophobic polymer on water transport and conductive properties will illustrate an optimum procedure for GDL manufacturers.

6.2 Electrode-integrated textile-based sensors for temperature and relative humidity monitoring in electrochemical cells

Chapter 4 presents the effect of external threads on carbon cloth GDL for generating water pathways within textile electrodes and measuring local RH and temperature. We developed a procedure to investigate the effect of hydrophilic thread on water transport, physical and microstructural properties and in-situ fuel cell testing. Besides, a scalable roll-to-roll process was developed to transform the cotton thread into RH and temperature sensors responsive to the working environment of PEMFCs. The summary of findings, contributions and suggestions for future work are presented in the following sections.

6.2.1 Summary of findings

1. The addition of threads on physical, microstructural and transport properties of woven GDL was investigated and showed minimal impacts on these properties with gain in generating water pathways within the woven GDL.

2. The in-situ fuel cell test showed that the addition of external threads did not affect the cell's performance in different operating conditions.

3. A proof of concept experiment was developed to monitor the temperature of carbon cloth GDL with the thread-based temperature sensor showing the sensor's effectiveness for the temperature monitoring of the textile electrode.

6.2.2 Contributions

1. Ex-situ water transport analysis shows that water pathways were generated within woven GDLs by sewing a hydrophilic thread on carbon cloth GDLs.

2. The addition of thread on carbon cloth GDL does not affect the performance of operating fuel cells in different RH levels (40% to 100% RH).

3. A scalable roll-to-roll process was developed to transform fibre-like RH and temperature sensors in a working range of PEMFCs environment.

4. The ex-situ experiment demonstrates fibre-like sensors' ability to monitor the temperature of the carbon cloth GDLs in a dynamic temperature range from 30 to 90 °C.

6.2.3 Recommendations for Future Works

1. *In-situ fuel cell testing combining with neutron imaging to monitor water pathways in woven GDL with hydrophilic threads.* We showed that hydrophilic threads play as water pathways within carbon cloth GDLs in the ex-situ experiment. Performing the test combining with neutron imaging can confirm this data in an in-situ fuel cell testing and shows the application of this method to modify woven GDLs to gain performance in operating fuel cells potentially.

2. *In-situ testing of fibre-like sensors in operating fuel cells.* In this work, we demonstrated a process to develop fibre-like sensors. Demonstrating the application of these sensors in operating fuel cells under various conditions (e.g. low and high RHs and temperatures) will prove the applicability of these sensors.

3. *Utilizing the local RH and temperature to control the input reactant conditions (i.e. temperature and RH) to improve the fuel cell performance..* These sensors can provide extra information that could be used to control the fuel cell conditions such as inlet temperature and, RH to improve the performance in a variety of different operating conditions.

6.3 A hybrid thread-based temperature and humidity sensor for continuous health monitoring

Chapter 5 presents the process of developing and characterizing thread-based RH and temperature sensors for application in health monitoring. A low-cost, dip-coating

process was employed to coat cotton threads with CNT ink. The aqueous ink composition is fMWCNTs and SDS, and they were optimized for achieving well-dispersed ink and well-attachment to the cotton threads. The CNT-coated response to RH and temperature changes were assessed and showed the CNT-coated thread is responsive to both RH and temperature. FEP coating was applied on top of CNT-coated thread to mitigate RH response. As a result, CNT+FEP-coated thread is solely sensitive to temperature. Combining CNT-coated and FEP+CNT-coated threads together can monitor temperature and RH of textiles. The biocompatibility analysis shows a benign effect on cell cytotoxicity and animal wound healing. The summary of findings, contributions and suggestions for future work are presented in the next sections.

6.3.1 Summary of findings

1. A durable and well-attached CNT-coated thread was achieved with the thread resistance of $\sim$20 kΩ/cm.

2. The CNT-coated thread response shows a quadratic resistance increase to RH (between 30 to 90%) changes and a linear resistance decrease to temperature changes (between 20 to 90 °C).

3. A function to predict the thread resistance to both temperature and RH changes were developed and showed the CNT-coated thread response to both parameters.

4. FEP polymer effectively coated on top of the CNT-coated thread, and a thread-based temperature sensor independent of RH was developed.

5. CNT-coated (RH sensor) and FEP+CNT-coated (temperature sensor) threads cytotoxicity was analyzed and showed cell viability of more than 85%. Also, the sensors did not show an adverse effect on the animal model wound healing process.

6.3.2 Contributions

1. The homogenous suspension was achieved by adding SDS as a surfactant. There is no difference between 5 mg/ml to 15 mg/ml SDS concentrations on the resistance of CNT-coated thread.

2. A durable, low-cost process was developed to coat cotton textile via a CNT ink, which is suitable for large scale manufacturing of CNT-coated threads.

3. We developed a procedure to characterize CNT-coated thread response to both temperature and RH changes and show that CNT-coated cotton thread is responsive to both temperature and RH.

4. A procedure was developed to mitigate the RH response of CNT-coated thread via a scalable and robust dip-coating thread in a hydrophobic FEP suspension.

5. A proof-of-concept experiment showed FEP+CNT-coated thread is independent of RH and can be used as a sensor in the e-textile system to reach a target temperature.

6. Combination of both CNT-coated and FEP+CNT-coated thread can effectively measure the temperature and RH within a textile clothing,

7. The developed thread-based sensors are biocompatible with a neutral effect on cell growth and wound healing process.

6.3.3 Recommendations for Future Works

z*Investigating the effect of different CNT types and surfactants on the performance of the sensors.* We made the CNT ink with fMWCNT and SDS in aqueous solution. However, CNT types such as single-wall carbon nanotubes and CNT length and dimension effects on the sensor response need to be investigated to obtain optimum performance out of thread-based sensors. *Investigating the CNT-coated response to temperature and RH in other environments.* We investigated the temperature response of CNT-coated thread in the air environment. The test can be performed to see the sensors' response to different settings such as Nitrogen, argon, or even in water bath varying temperature. *Investigating the durability of the sensors through washing cycles.* The sensors show excellent durability for more than six months. To further investigate the sensors' strength, washing the sensors can be done to confirm the washability of the sensors. *Performing in-vivo test for monitoring athlete skin temperature and RH via thread-based temperature and RH sensors.* For proof-of-concept, continuous monitoring of temperature and humidity of human skin under three different

conditions, seating, walking and running should be done to determine the applicability of the sensors for wearable health monitoring for athletes. *Combining thread-based sensors in advanced drug delivery textile patches to control the drug release based on the measured temperature.* The sensors can be embedded in the advanced drug delivery system that requires heating to release drugs from thermorespnosive particles. The temperature sensor can adjust the heating process in the smart wound dressing patches.

Appendix A

Supplementary information of chapter 3

A.1 Compression under the glass

One important parameter is the compression of GDLs. A pressure film allowed us to monitor the GDL compression. The pressure film has microcapsules that are released due to the compression. Increasing the compression releases more microcapsules and high intensity of red colors can be obtained from the film. By comparing the color with a reference, we can estimate the pressure. Figure A.1 shows the clamping device, the GDL and the pressure film. The pressure film is red on the border and in the middle. The red signs on the border is because of cutting samples. The red signs in the middle is due to the compression between plaxiglass and the O-ring. The intensity of that area was compared with a reference and it is around 1.6 MPa. The pressure is in a range of operating fuel cells [15].

A.2 Quantification of Carbon and Fluorine in GDLs

The following photos are the quantification of carbon and fluorine on the surface and cross section of woven GDLs (without coating, 30 wt% FEP and 55 wt% FEP).

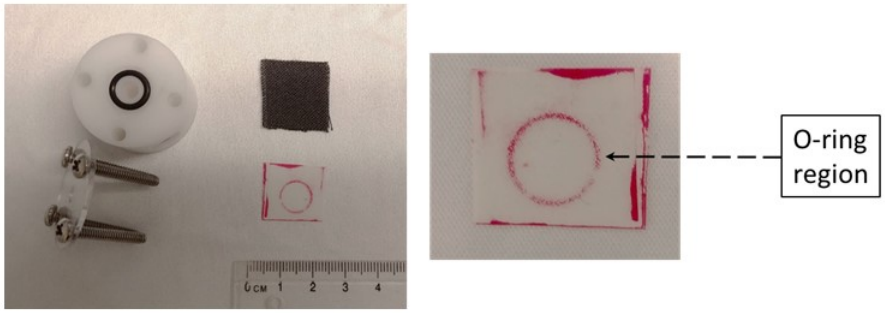

Figure A.1: The clamping setup, the GDL and the pressure film.

A.3 Reproducibility Test

Figure **??** shows the breakthrough analysis for similar samples, without coating, 30 wt% FEP and 55 wt% FEP. The results are following the conclusion in the manuscript. The coated samples have water in the compressed regions, which means lateral water transport, however, pristine sample did not show any lateral water transport. In addition, the breakthrough locations also follow the same pattern. The uncoated sample has the breakthrough in the uncompressed region and the coated samples had the breakthrough in the compressed regions.

A.4 Mechanical Test

FEP coating changes the elasticity of the woven GDLs. Higher loading is more brittle. To investigate this quality, three samples were tested in two tests. One is bending

sample 180 and the other one is the. tensile test. Bending 180 causes to break the 55 wt% FEP loaded GDL, and partial break on 30 wt% FEP loaded GDL. However, the untreated samples keep the shape and there is no sign of tear in the sample. Figure A.4 shows the result of the test.

The next test is measuring the module of elasticity of these three samples. The results show that the higher the FEP loading, the higher the modulus. Figure A.5 shows this fact. The summary of the results is available in the table S1. The test was performed with MT10K.

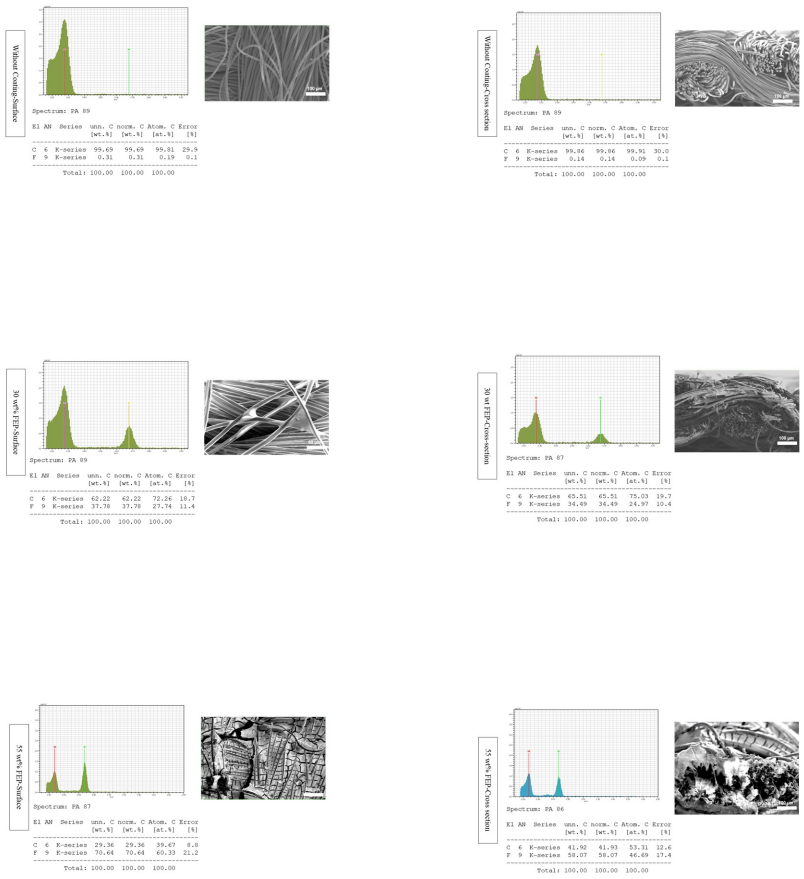

Figure A.2: quantification of carbon and fluorine on the surface and cross section of woven GDLs.

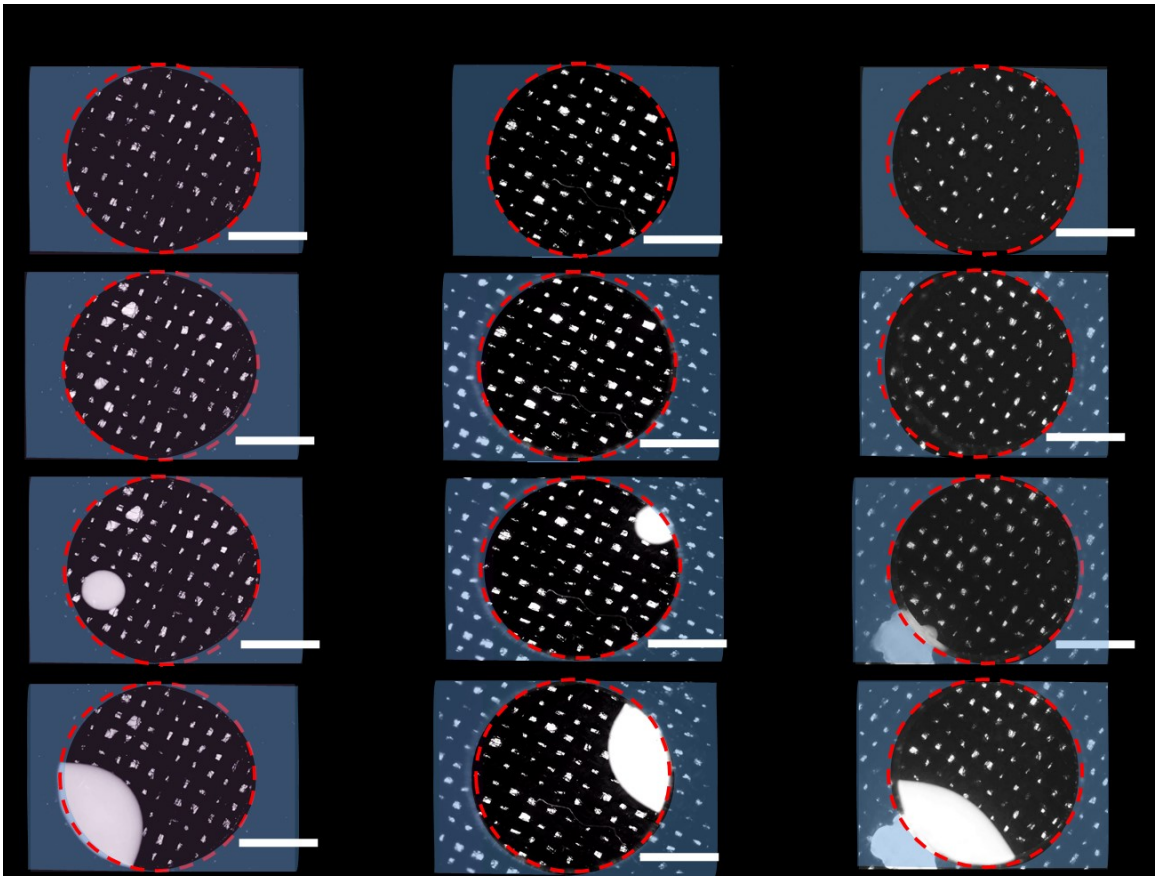

Figure A.3: Water breakthrough for GDLs without coating, 30wt% FEP and 55wt% FEP loading in four instances (the scale bar is 2 mm).

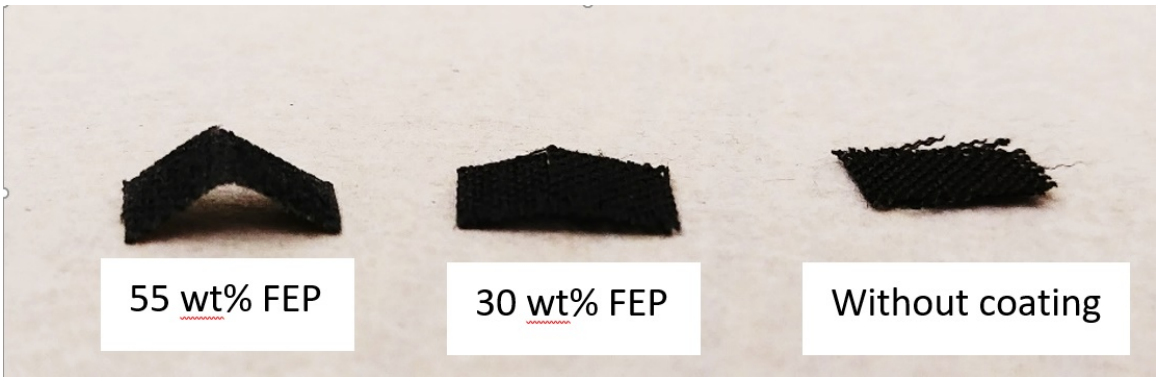

Figure A.4: Bending test of GDLs without coating, 30 wt% FEP and 55 wt% FEP.

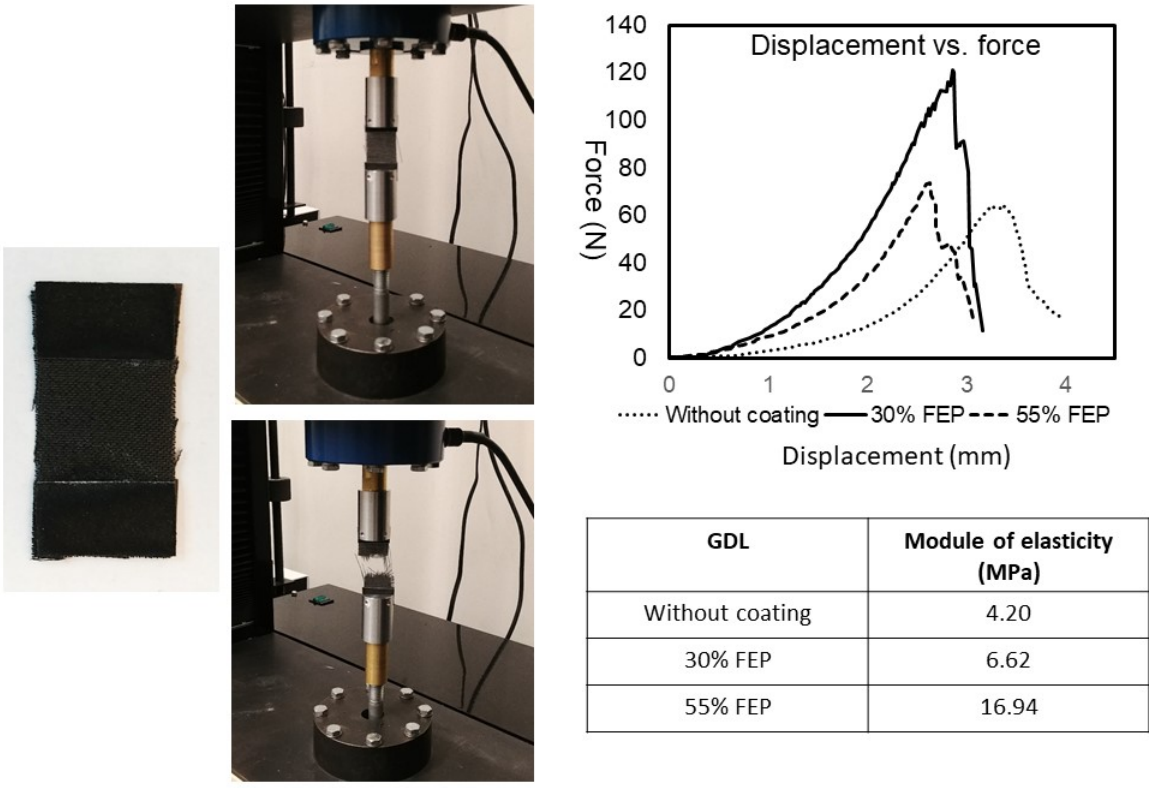

GDL	Module of elasticity (MPa)
Without coating	4.20
30% FEP	6.62
55% FEP	16.94

Figure A.5: Tensile test on woven GDL.

Appendix B

Supplementary information of chapter 4

This appendix illustrated supplementary results for chapter 4 of the thesis.

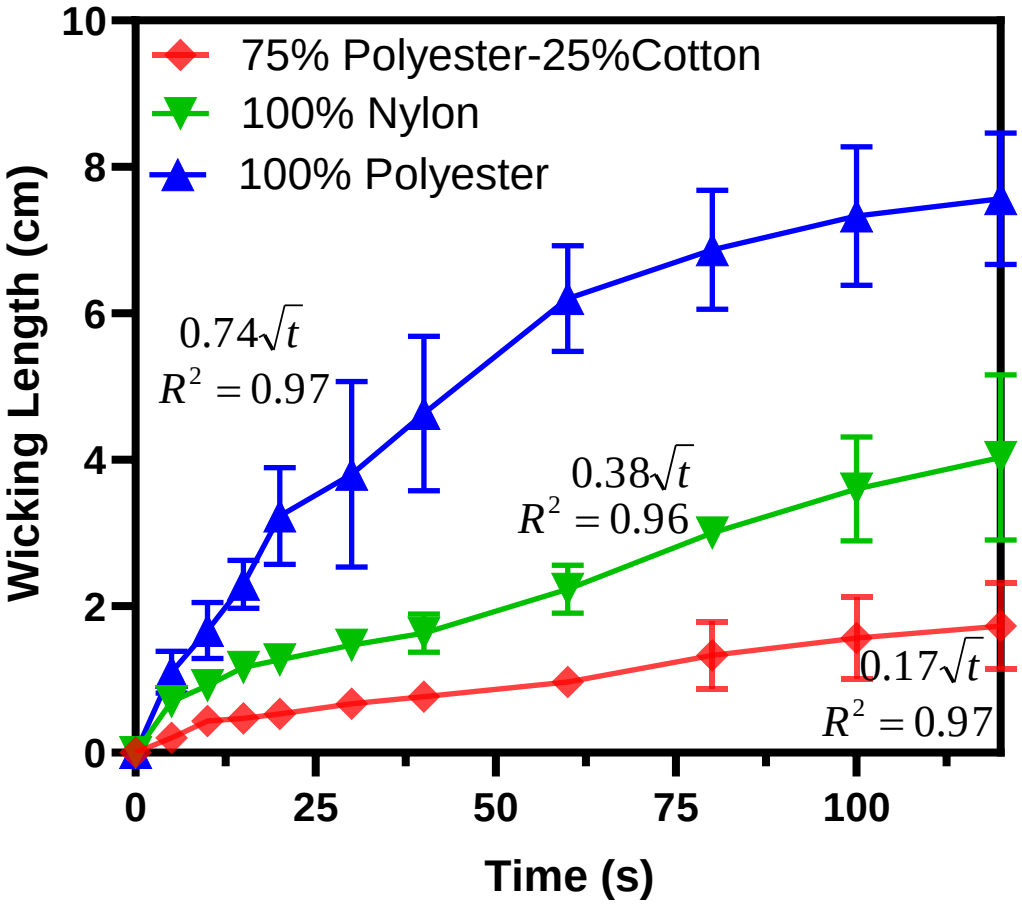

Figure B.1: Wicking test for three commercial threads (after corona discharge treatment). Thread wetting followed a square root of time and the polyester thread showed a highest wicking property.

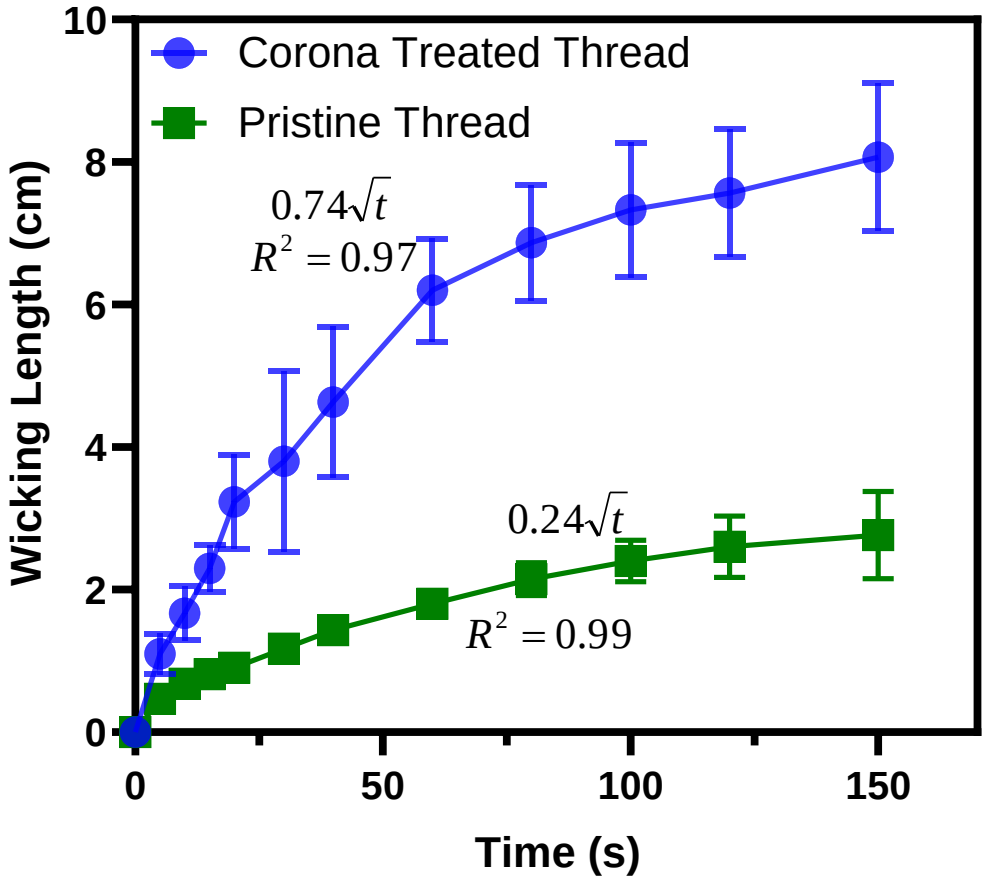

Figure B.2: Effect of Corona discharge on wicking property of polyester thread.

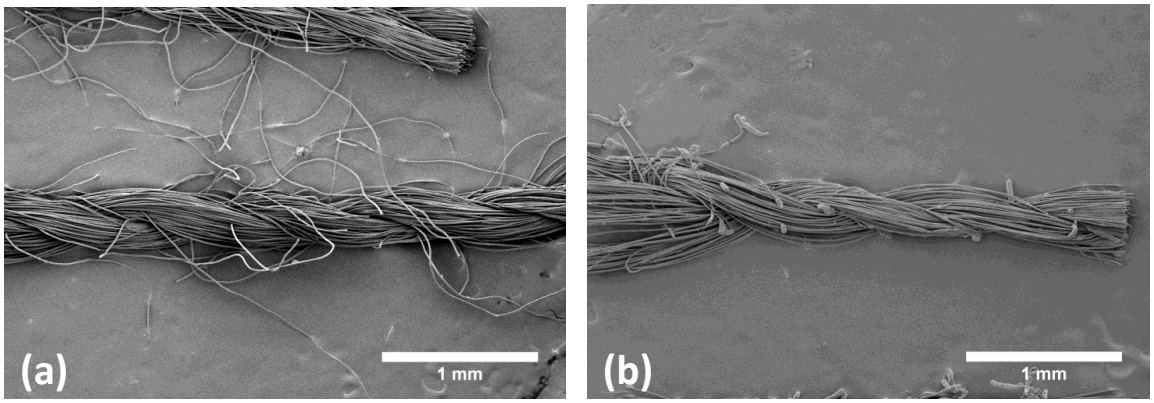

Figure B.3: Effect of Corona discharge on the microstructure of thread (a) before treatment (b)after treatment.

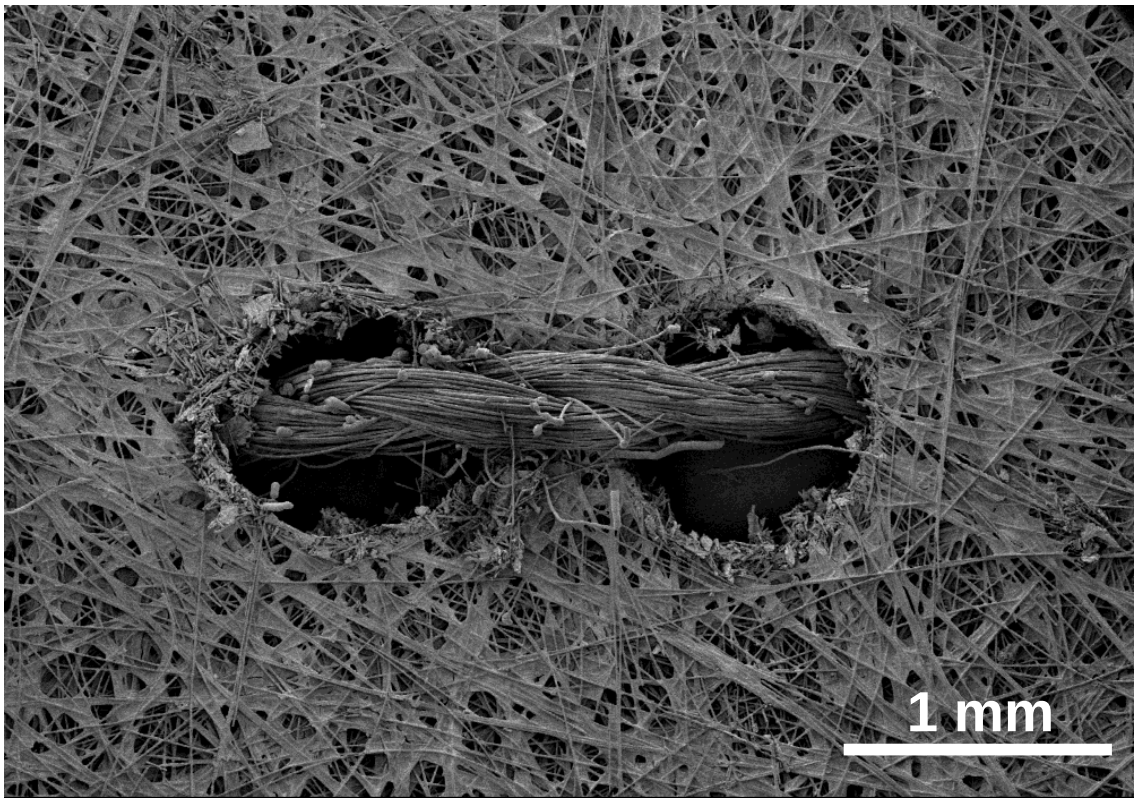

Figure B.4: Effect of sewing thread on non-woven GDL (Toray 090).

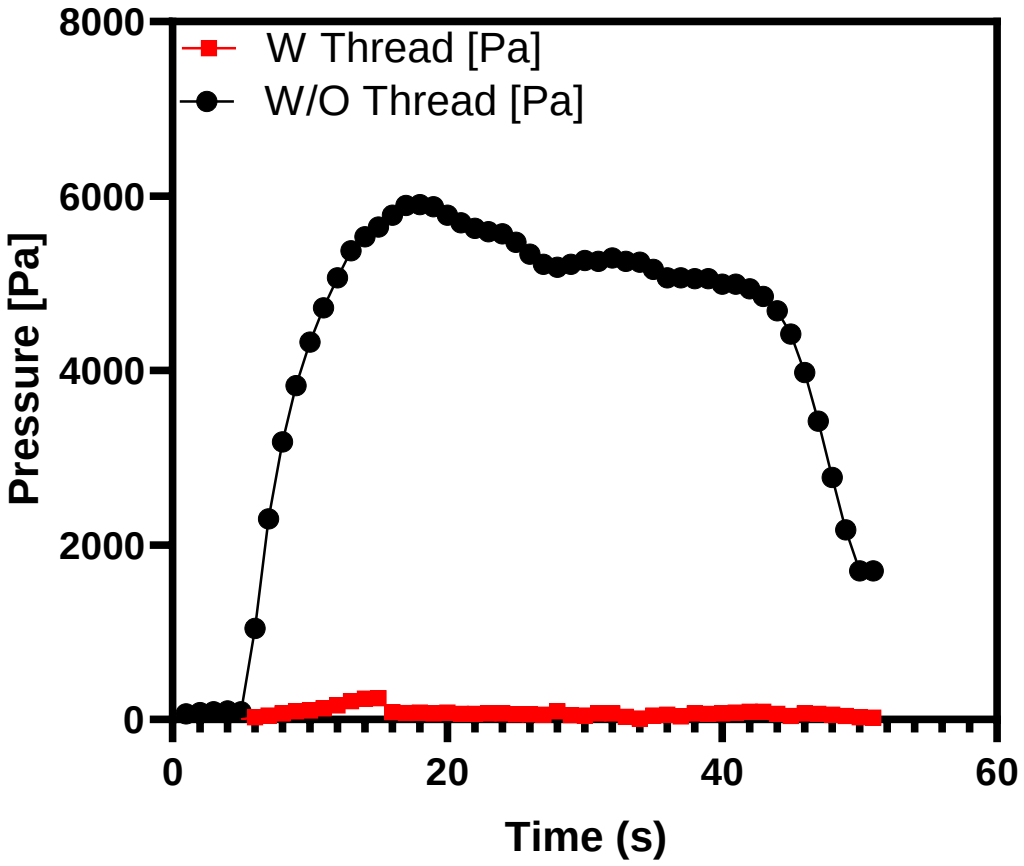

Figure B.5: Effect of sewing thread on breakthrough pressure of Non-woven GDL vs pristine non-woven GDL.

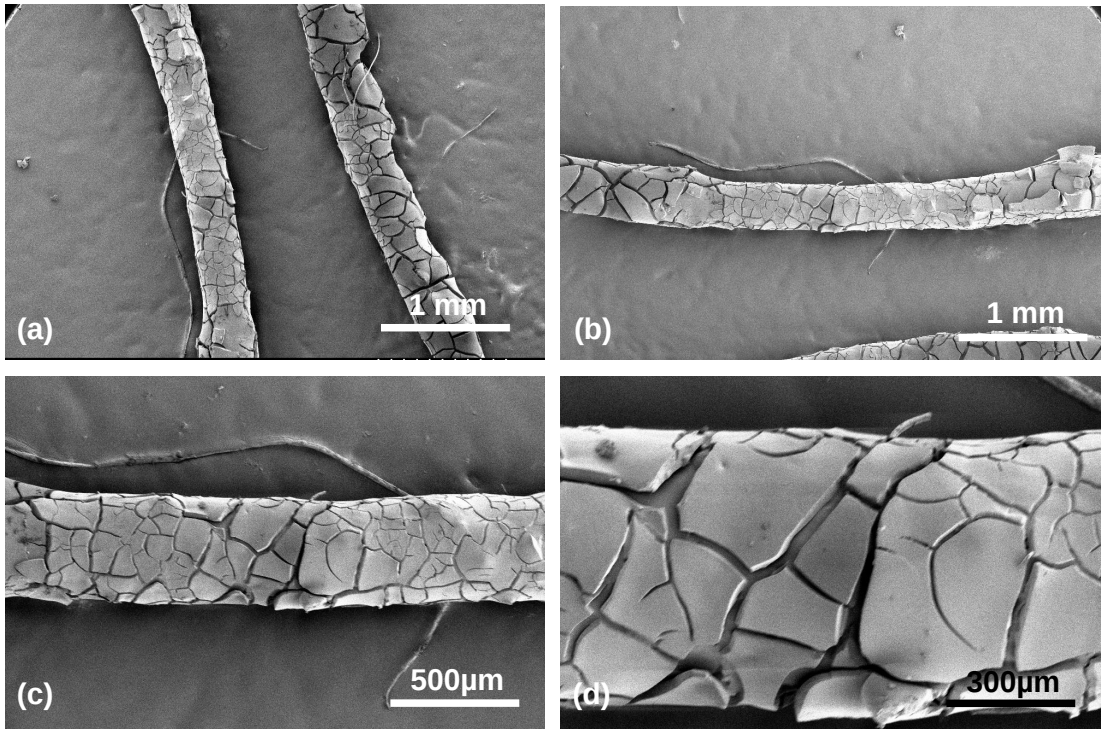

Figure B.6: SEM image of FEP coating on different samples showing cracking on the surface.

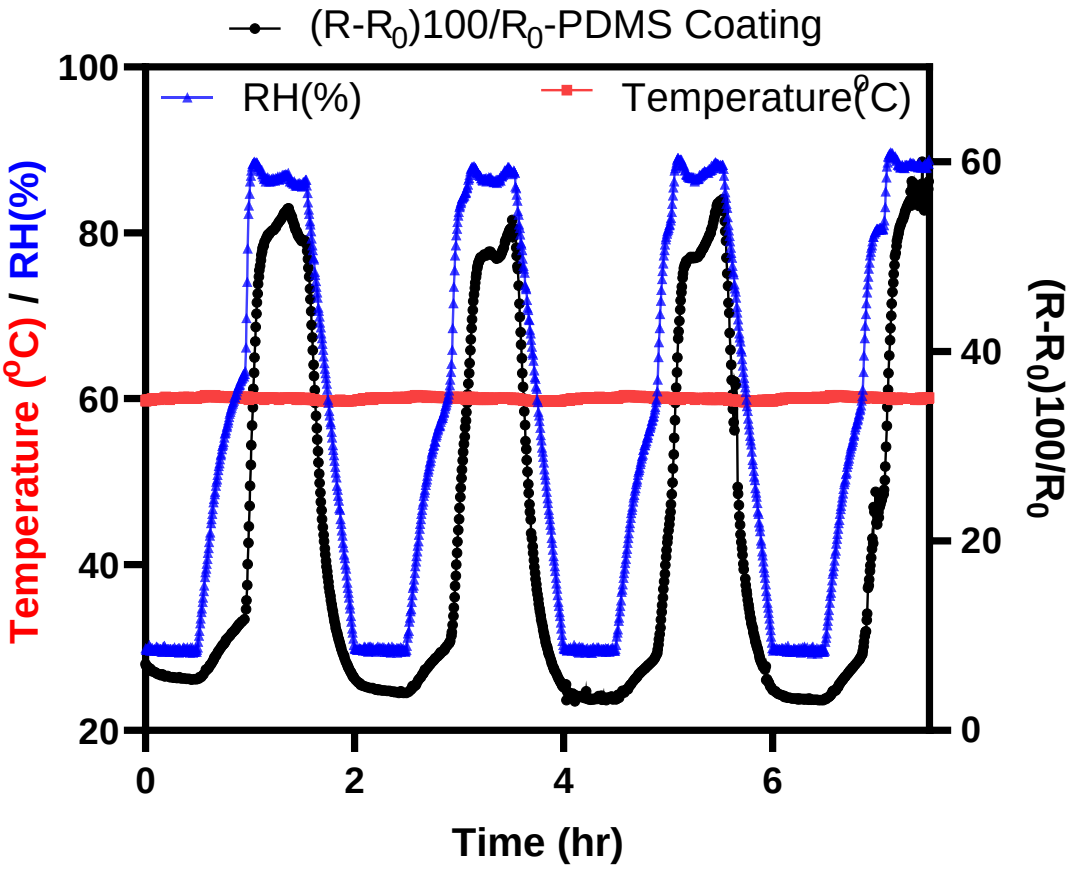

Figure B.7: Cyclic response to RH changes for thread-based RH sensor (CNT coated thread with PDMS coating).

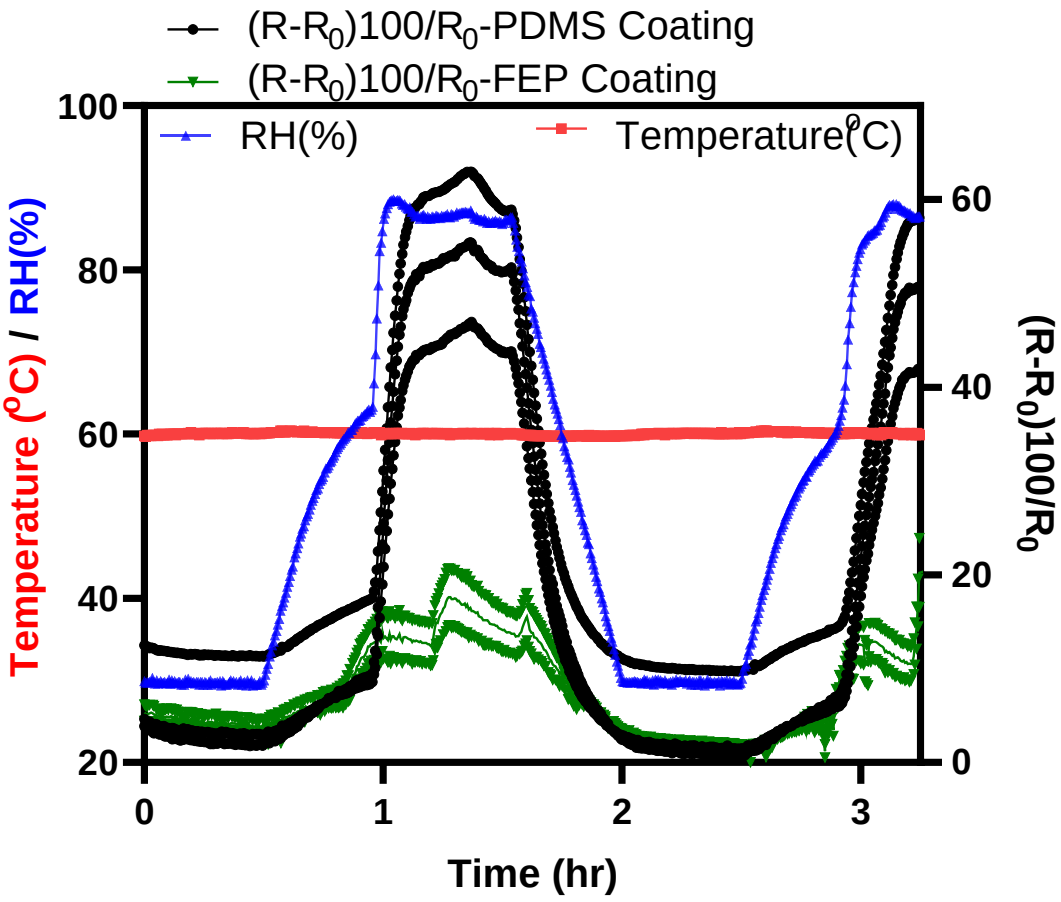

Figure B.8: Cyclic RH response for three replicates of thread bases temperature and RH sensors.

Appendix C

Supplementary information of chapter 5

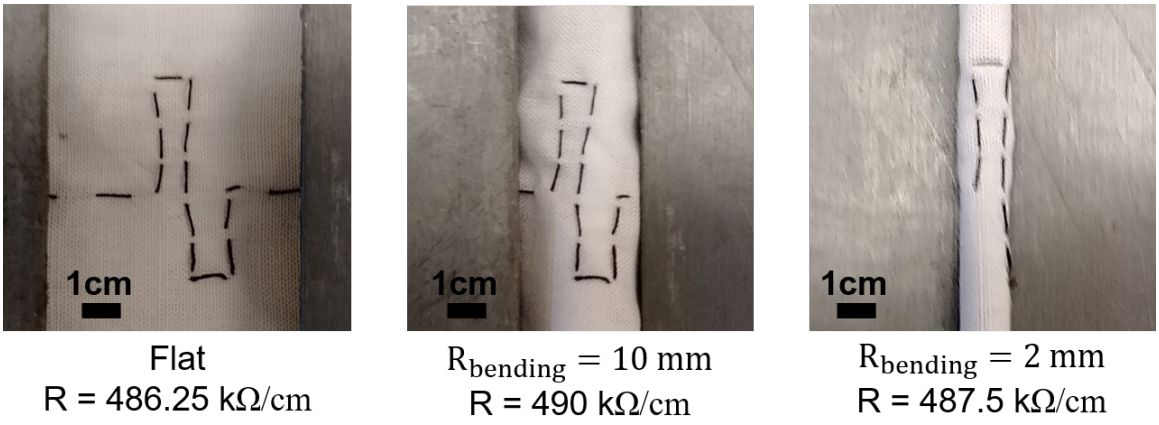

Figure C.1: Thread resistance, unbent, with radius of 10 mm and radius of 2 mm

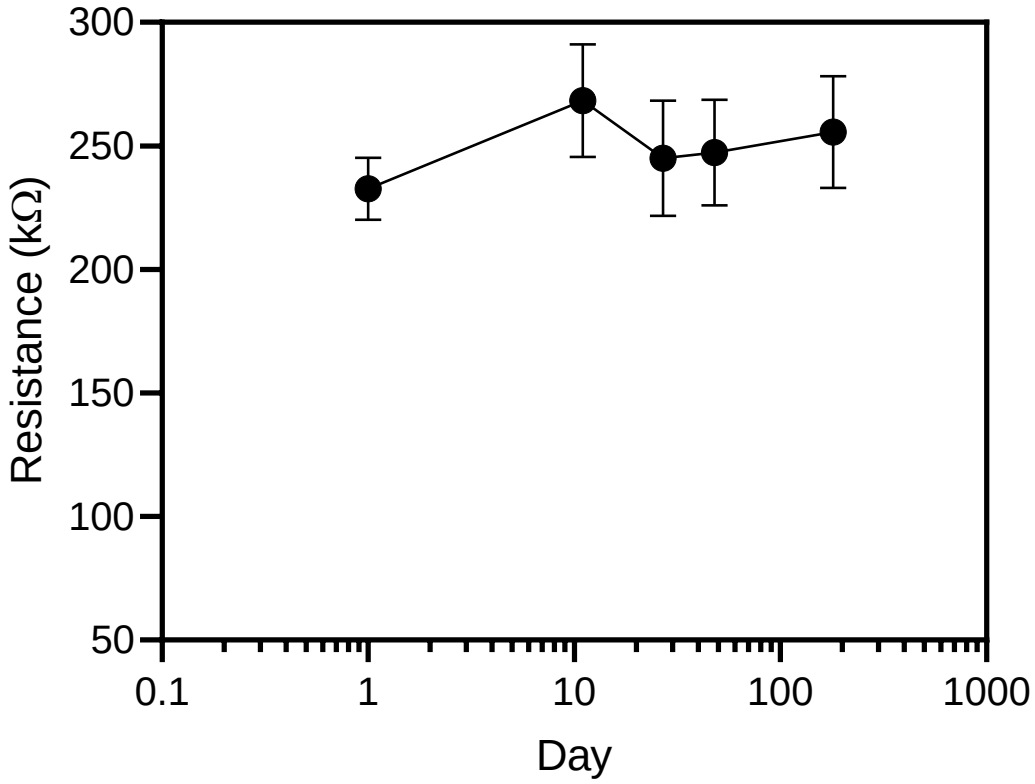

Figure C.2: Thread resistance over 6 months (kept in room temperature and closed petri dish).

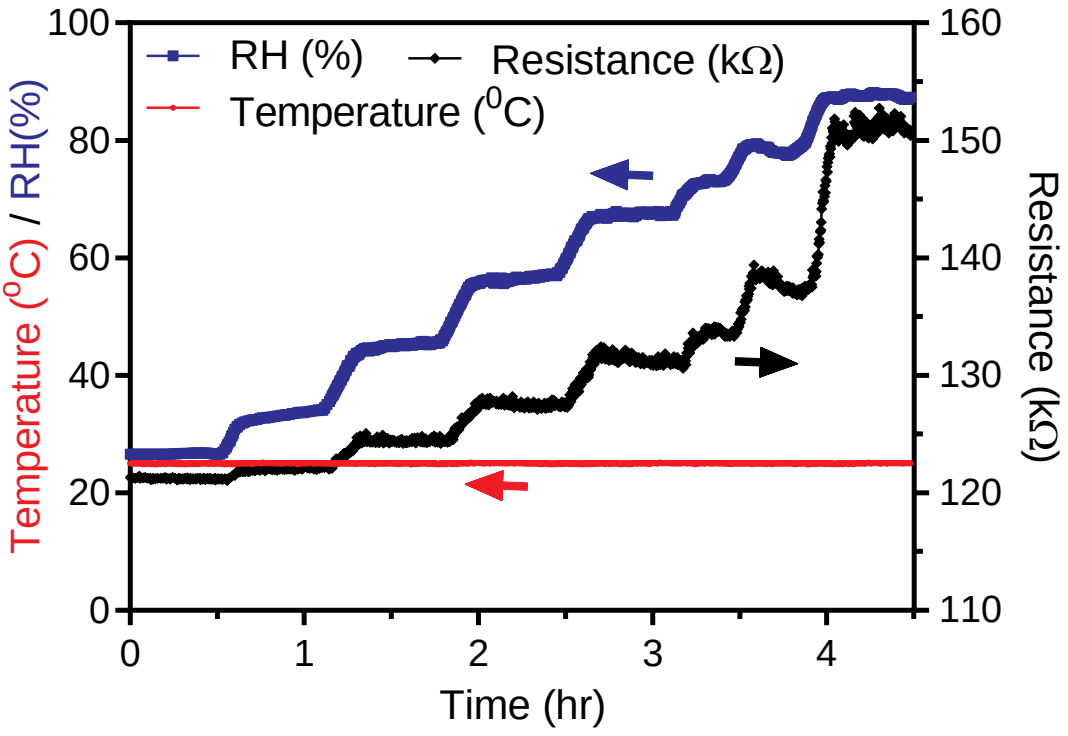

Figure C.3: The CNT-coated thread resistance vs. RH changes.

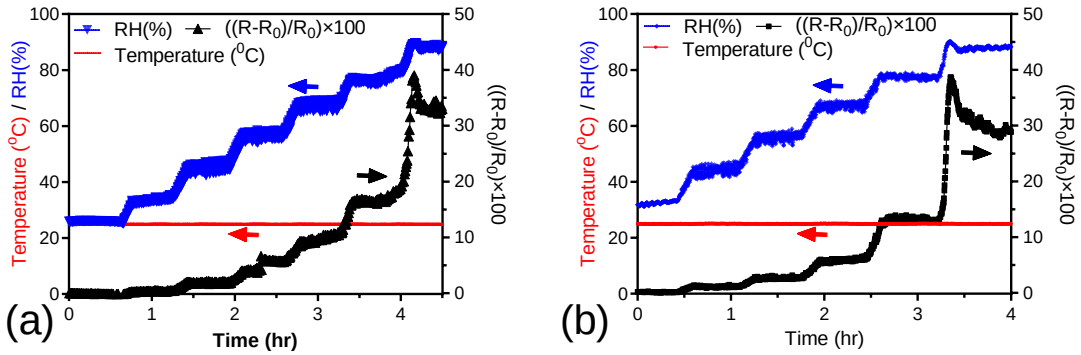

Figure C.4: Observations of a similar response of CNT-coated thread to RH changes for two more replicates.

Table C.1: Quadratic resistance changes to RH at 25, 50 and 75 °C.

Temperature (°C)	$\frac{(R-R_0)}{R_0} \times 100$	R_{sq}
25	$8.1 - 0.49RH + 0.008RH^2$	0.99
50	$19.16 - 0.93RH + 0.011RH^2$	0.93
75	$18.78 - 0.91RH + 0.011RH^2$	0.94

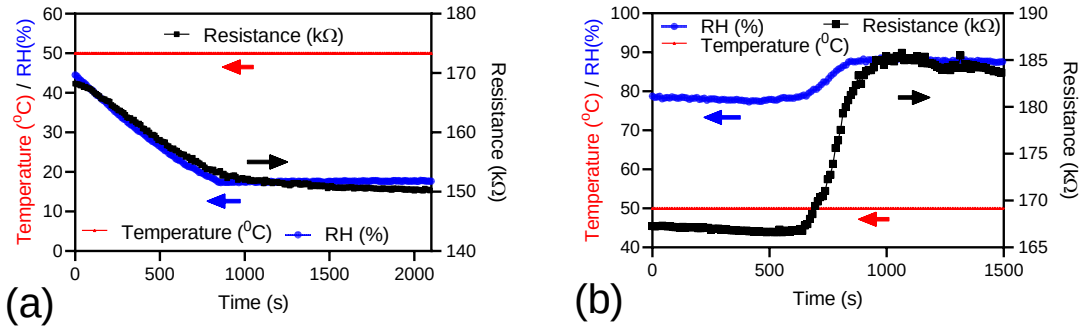

Figure C.5: Fast response of the CNT-coated thread to change of RH (a) in low RH regions and (b) in high RH regions

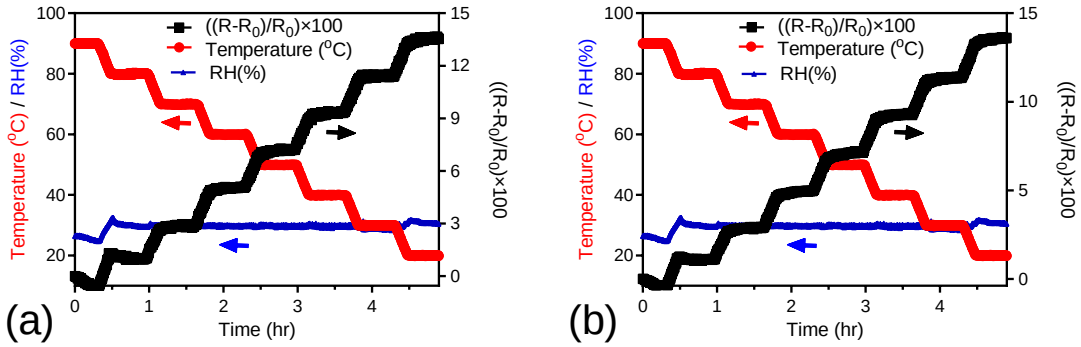

Figure C.6: Observations of the same response of CNT-coated thread to temperature change for two more replicates.

Table C.2: Linear resistance change to temperature at 30, 50 and 75% RHs.

RH(%)	$\frac{(R-R_0)}{R_0} \times 100$	R_{sq}
30	-0.19T+16.53	0.98
50	-0.22T+19.25	0.99
75	-0.21T+18.74	0.98

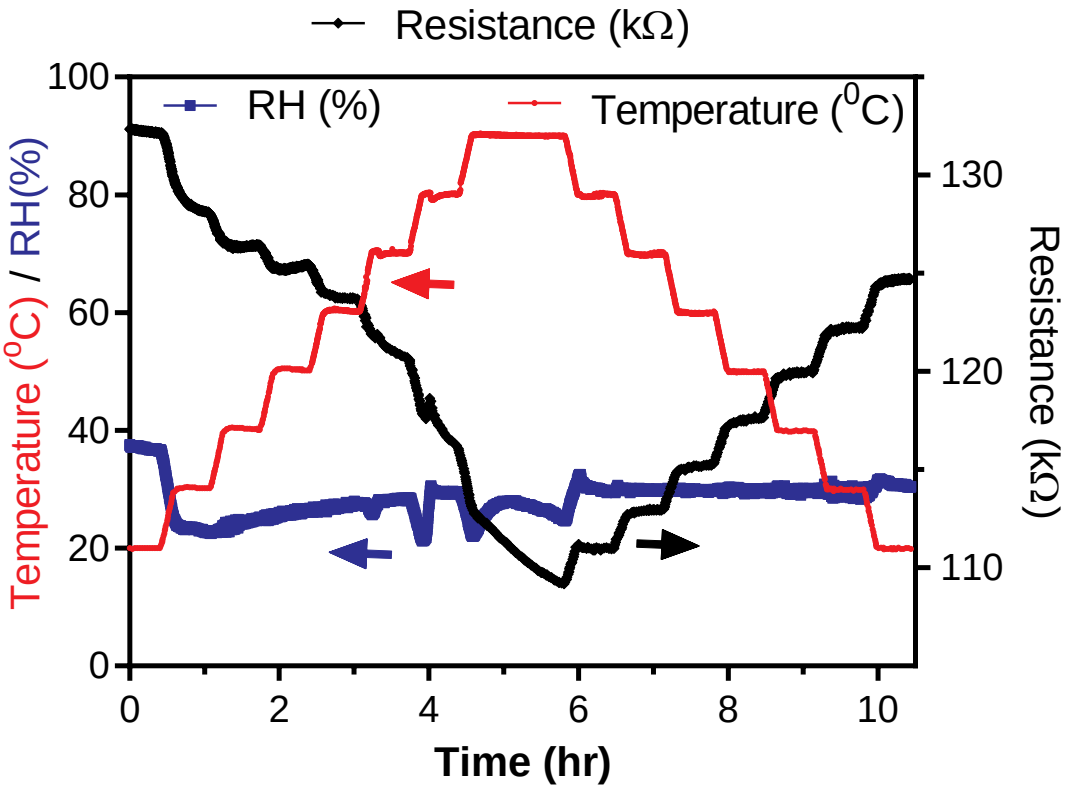

Figure C.7: Hysteresis test for temperature from 20 °C to 90 °C and 90 °C to 20 °C.

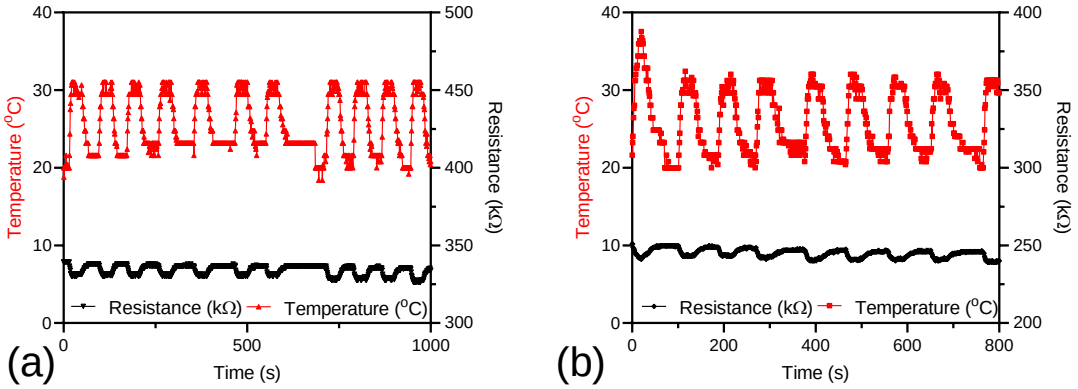

Figure C.8: Heating threads with thread-based sensor for two more replicates.

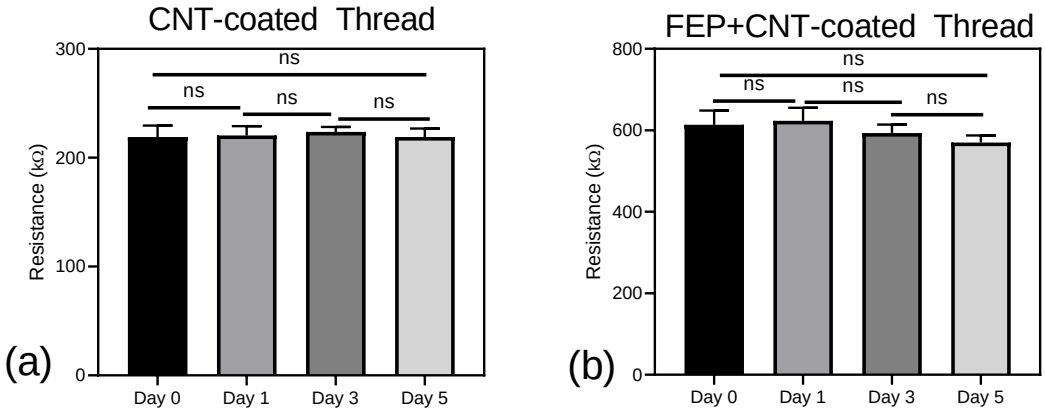

Figure C.9: Thread-based sensor resistance on the wound (a)CNT-coated (RH sensor) and (b) FEP+CNT-coated sensor(temperature sensor).

C.1 Animal Study ethics

In the following pages, application to use animals for research is presented.

University of Victoria

Office of Research Services
Animal Care Committee
Administrative Services Building, Room B202

Research & teaching with animals website (ACC)

Animal housing & care website (ACS)

Protocol Number:	Start Date:	Expiry Date:
2018-021 (1)	29-Nov-18	29-Nov-19
Amendment Dates: June 2019		

For Administrative Use Only (AUP4)
last revised November 20-2015

Application to Use Animals for Research

Click on blue text to display "help boxes" while completing this form.
The Application HELP SHEET is available on the ACC website to assist you.

1. Project

Title
Development of smart bandages for treatment of chronic wounds in a diabetic rodent model

STATUS ☐ New Application ☐ Pilot Project ☒ Amendment of Protocol #: _____

If your protocol is also due for its Continuation, please complete the Annual Renewal form.

2. Contact Information

PRINCIPAL INVESTIGATOR

Surname	First Name	Initial
Akbari	**Mohsen**	**MA**

Rank / Position (please indicate)	Department
Assistant Professor	**Mechanical Engineering**

Business & Laboratory Telephone	Residence Telephone	Emergency / Cell Telephone

Laboratory Address	E-mail Address
Engineering lab wing B239	

NAME OF DESIGNATED ALTERNATE FOR EMERGENCIES

A. (mandatory)

Surname	First Name	Emergency Telephone
Kaveh	**Mona**	

B. (optional)

Surname	First Name	Emergency Telephone
Hadisi	**Zhina**	

3. Declaration

The information in this application is exact and complete. I assure that all care and use of animals in this proposal will be in accordance with the guidelines and policies of the Canadian Council on Animal Care and those of the University of Victoria. I shall request the Animal Care Committee's approval prior to any deviations from this protocol as approved. I **understand that this approval is valid for one year and must be approved on an annual basis.**

Principal Investigator	Signature	Date
Mohsen Akbari		

UVic Department Chair	Signature	Date

(When the Department Chair is the Principal Investigator, the signature of the Dean is required)

4. Approvals

University Veterinarian Signature	Chairman, University Animal Care Committee Signature

5. Amendments made to Protocol

☐ **N/A (New protocol; go directly to section 6)**

5a) Please indicate the section/subsection numbers where the amendments have been made.

☐ 6	☒ 7	☐ 8	☐ 9a	☐ 9b	☐ 10a	☐ 10b	☐ 10c
☐ 11	☐ 12a	☒ 12b	☒ 12c	☒ 12d	☒ 13	☒ 14a	☒ 14b
☐ 14c	☐ 14d	☐ 14e	☐ 15a	☐ 15b	☒ 15c	☐ 16a	☐ 16b
☐ 17a	☐ 17b	☒ 17c	☒ 17d	☐ 17e			

5b) Justification for amendment(s):

Added the infected wound model using Biosafety level 2 bacteria and changing 1 wound to two wound per animal.

6. Primary Funding Information

Agency: **CIHR** ☒ External ☐ Internal ☐ Other

Status: ☒ Awarded ☐ Pending

Peer Reviewed: ☐ No ☒ Yes

Funding Start Date: **31 Mar 2017** Funding End Date: **31 Mar 2020**

Funds Administered by: ☒ UVic ☐ Other – Provide Details:

Billing Account Number (required for invoicing of project costs): **33054 52300**

7. Research Timelines

Proposed Start Date of Research: **15 Feb 2020**

Proposed End Date of Research: **15 Feb 2021**

8. Category of Invasiveness

☐ A ☐ B ☐ C ☒ D ☐ E

9. Animal Use Data for CCAC

9a) Purpose of Animal Use

If the application includes breeding, select 0. If the application also includes research, select one additional option of 1 - 5.

☐ 0. Breeding colony / stock
☐ 1. Studies of a fundamental nature / basic research
☒ 2. Studies for medical purposes relating to human / animal diseases / disorders
☐ 3. Studies for regulatory testing of products, for the protection of humans, animals or the environment
☐ 4. Studies for the development of products or appliances for human or veterinary medicine
☐ 5. Education and training of individuals in post-secondary institutions or facilities

9b) Study Details

i. Will field studies be conducted? ☐ Yes ☒ No

ii. Will research involve surgery? ☒ Yes ☐ No ☒ recovery surgery or ☐ terminal

Please review the Policy on Survival Surgery of Rodents, Recovery Surgery checklist and Surgical record template.

iii. If breeding transgenics, knockouts or mutant animals, please complete the Transgenic Information Sheet

10. Summary

10a) Lay description (in language that will be understood by members of the general public): (2-3 sentences please)

This study focuses on developing smart bandages and suture material that detect bacterial infections and release antibiotics automatically without removing the dressing. This bandage will be used for treatment of slow-healing epidermal injuries such as those in diabetic patients. These injuries represent a major life-threatening and life-altering event that impacts the quality of life of many Canadians each year. Our hi-tech dressing will generate significant savings in healthcare costs, due to reduced clinical inspection time and shorter hospital stays as a result of faster wound healing.

10b) Specific scientific objectives of the study (2 – 3 sentences):

The smart bandage technology and suture material will be primarily used to treat patients with diabetic wounds. These wounds are slow-healing and are prone to bacterial infections. Therefore, we will test the efficiency and safety of the smart bandages and suture material in diabetic and infected animals. Three objectives of this study are: 1) model development and surgical characterization, 2) toxicity/safety studies and 3) efficacy studies.

10c) Keywords (click here for a list of recommended keywords):

Research, study the effectiveness of a product, breeding, pilot study, tissue collection, rat,mouse, injection (subcutaneous, intravenous),infection induction, infectious agents, blood sampling (small volume), minor surgery, survival surgery.

11. Alternatives

State why animals must be used in the study. If alternatives to animals are available, indicate why they are not being used in this study.

There is no alternative exists at the moment that mimics the immunoresponse and multi-organ complexities of animals.

12. Animal Data

12a) Describe the rationale for using this specific species or strain.

We are proposing to use both mice and rats for this study to establish which species will be best for our larger study program. Based on our review of the literature, the strains that we are proposing are used extensively for diabetic and wound studies. Because the Smart Bandage and suture material is a new appliance, we are not sure which of these 2 species will be most appropriate from a size and management perspective, thus we are proposing both for the initial pilot study.

12b) Are there special housing requirements? (Normal housing parameters can be found at the ACS website **here**)

☐ No ☒ Yes

Please review the ACC Procedure on Alternative Housing of Experimental Animals.

If yes, please list them (including the species or strain):

Animals will need to be singly housed after surgical procedure until completion of the experiment to avoid any potential complications associated with cage-mate interference with the Smart Bandage or the splint. Until the surgical procedure, animals may be pair or group housed with compatible same-sex animals. Post-operatively, in-cage enrichment will be tailored to limit the risk to the bandage and splint (e.g. tall huts will be provided).

Animals given level II pathogens will need to be housed in quarantine.

12c) Indicate the number of animals required.

☒ Lab animals (mammalian) required?

Delete Strain Record

MAMMALIAN - Species			Common Name			Supplier / Source		Strain		
Rat			Rattus norvegicus			Charles River		Sprague Dawley		
Housing Location	Experimental Location	# Acquired / Purchased	# females breeding	# males breeding	# females culled	# males culled	# females for experiment	# males for experiment	# Needed at One Time	Total # Per Year
BWC	BWC	60	0	0	0	0	30	30	60	60

Delete Strain Record

MAMMALIAN - Species			Common Name			Supplier / Source		Strain		
Mouse			mus musculus			Charles River		C57BL/6		
Housing Location	Experimental Location	# Acquired / Purchased	# females breeding	# males breeding	# females culled	# males culled	# females for experiment	# males for experiment	# Needed at One Time	Total # Per Year
BWC	BWC	12	8	4	6	6	30	30	60	84

Delete Strain Record

MAMMALIAN - Species			Common Name			Supplier / Source		Strain		
Mouse			mus musculus			Jackson lab		BKS.Cg-Dock7<m> +/+ Lepr<db>/ (also called db/db) J Stock# 000642		
Housing Location	Experimental Location	# Acquired / Purchased	# females breeding	# males breeding	# females culled	# males culled	# females for experiment	# males for experiment	# Needed at One Time	Total # Per Year
BWC	BWC	60	0	0	0	0	30	30	60	60

Delete Strain Record

MAMMALIAN - Species			Common Name			Supplier / Source		Strain		
Mouse			mus musculus			Jackson lab		BALB/C		
Housing Location	Experimental Location	# Acquired / Purchased	# females breeding	# males breeding	# females culled	# males culled	# females for experiment	# males for experiment	# Needed at One Time	Total # Per Year
BWC	BWC	192	0	0	0	0	52	140	180	192

Delete Strain Record

MAMMALIAN - Species			Common Name			Supplier / Source		Strain		
Mouse			mus musculus			Jackson lab		BALB/C		
Housing Location	Experimental Location	# Acquired / Purchased	# females breeding	# males breeding	# females culled	# males culled	# females for experiment	# males for experiment	# Needed at One Time	Total # Per Year
BWC	BWC	66	0	0	0	0	33	33	40	66

Add Strain

☐ Field animals required?

☐ Lab animals (aquatic species) required?

12d) Indicate how you arrive at your total number of animals (click here for an example calculation):

Diabetic mice (not infected)

We will have 5 groups with 5 animals per group, per species for this pilot study.

1) Wound treated with blank GelDerm
2) Wound treated with commercial wound dressing (Integra or Tegaderm)
3) Wound treated with VEGF-loaded GelDerm
4) Wound treated with bFGF-loaded GelDerm
5) Wound treated with bFGF/VEGF-loaded GelDerm

We will be sacrificing the animals at 2 time points (7 days and 28 days).

Animal number = 5 groups * n 5 * 2 time points = 50 animals + 10 possible replacement experimental animals= 60 in total for experiment.
This is the smallest number of animals that will a) allow us to work out the logistics of the wound/bandage experiments b) provide us with sufficient information that can be used for larger animal studies of a similar design.

For the C57 mice we may breed the mice required for the study.
For breeding there will be 4 breeding cages with trios (12 mice - 8 female, 4 male).
Each breeding cage will average 9 pups every 3 weeks (based on two female breeders per cage)
4 breeding cages x 9 pups = 36 pups after 3 weeks, 72 pups after 6 weeks
72 pups - 60 experimental animals needed = 12 extra animals to be euthanized or re purposed
72 pups + 12 breeders = 84 animals total needed for this study

We will use the C57 model first as a pilot prior to bringing in the db/db mouse model from Jackson labs. The db/db mouse model from Jackson is infertile and therefore all mice will need to be purchased if using them for this project. The db/db model is predisposed to develop diabetes and has been used in wound impairment/healing studies so may be a valuable model for us to also use in this wound bandage study.

Non-diabetic (infected wounds)

1) Uninfected wound with no bandage
We will be sacrificing the animals at 3 time points (7, 14, and 28 days)--> 3 time points * n 4*2 (male and female) =24

2) Uninfected + GelDerm + no antibiotics
We will be sacrificing the animals at 3 time points (7, 14, and 28 days)--> 3 time points * n 4=12
3) Uninfected + GelDerm + Antibiotics
We will be sacrificing the animals at 3 time points (7, 14, and 28 days)--> 3 time points * n 4=12
4) Uninfected + Tegaderm + No Antibiotics
We will be sacrificing the animals at 3 time points (7, 14, and 28 days)--> 3 time points * n 4=12
5) Infected wounds with no treatment
We will be sacrificing the animals at one time point (7 days)--> 1 time point * n 10* 2 inoculation concentrations *2 (male and female) =40
6) Infected wounds with GelDerm and no treatment
We will be sacrificing the animals at one time point (max 7 days)--> 1 time point * n 10* 2 inoculation concentrations=20
7) Infected wounds with GelDerm+ antibiotics
We will be sacrificing the animals at one time point (7 days)--> 1 time point * n 10* 2 inoculation concentrations * 2 (male and female)=40
8) Infected with Tegaderm and antibiotics
We will be sacrificing the animals at one time point (max 7 days)--> 1 time point * n 10* 2 inoculation concentrations=20
9) Wound sutured with biocompatible polymer suture material (polystyrene sutures coated with a thin layer of silk fibroin- polycaprolactone- gentamycin)
We will be sacrificing the animals at 3 time points (7, 14, and 28 days)--> 3 time points * n 4=12
Animal number = Groups 1 n* 24, Groups 2-4 & 9* n 12 = 48 animals. Groups 5 & 7 n* 40 = 80, Groups 6 & 8* n 20 = 40 . Total for experiment= 192.
*The number of animals for infected wounds (groups 5-8) is higher as we expect higher possible morbidity rates in these models.
* Females have been added to groups 1, 5 & 7 to examine gender effect on wound healing.

** infected wounds with biosafety level 2 bacteria**

We will have 12 different type of bacteria (listed in Table 15c) with 5 animals per group.
We will be sacrificing the animals at 1 time point (max 14 days)---> 12 type of bacteria * n 5* 1 time point = 60
We also consider adding (10%) “buffer” to account for potential experimental challenges -----> 10% * 60= 6
-We will start with 6 type of bacteria at one time with 5 animals per group to evaluate the effect of each type of bacteria on wound contraction and pH changes
-we will do same experiment with the other 6 type of bacteria using 5 animals per group

---

13.
Standard Operating Procedures (SOP's) (click here to access all SOP folders on the ACS website)

Please click on the subject and choose the SOP's that apply to your research or teaching project:

☐	**Antibodies**
☐	**Aquatics - General Procedures**
☐	**Aquatics - Health**
☒	**Facility Procedures (mammalian)**

☒ AC1021 BWC - Entry/Exit Procedures

☐ AC1015 Disposal of Soiled Animal Bedding Containing Infectious Waste

☐ AC1016 MSB - Entry/Exit Procedures

☐ AC1045 AIMS Tattoo Machine Care and Maintenance

☐ AC1031 BWC - Intra-facility Movement of Personnel

- [ ] AC1033 Procedure Room Cleaning: BWC
- [ ] AC1034 Procedure Room Cleaning: MSB
- [ ] AC1038 BWC Sanitation
- [ ] AC1039 MSB Sanitation
- [ ] AC1040 BWC - Transportation of Laboratory Animals
- [ ] AC2059 Fecal Flotation Test
- [ ] AC2066 Perineal and Fur Testing for Endo/Ectoparasites
- [ ] AC2070 Procedures for Escaped Rodents
- [x] AC3001 Surgical Equipment Sterilization Techniques
- [ ] AC3009 BWC Dumpstation Use and Maintenance
- [ ] AC3011 MSB Dumpstation Use and Maintenance
- [ ] AC3014 Use of Freight Elevator - BWC
- [ ] AC3017 Processing of Cytotoxic Cages
- [ ] AC3021 Use of Class 3B Laser

- [ ] **Field studies**

- [x] **General Animal Procedures**

- [x] AC2009 Rodent Analgesia - Adult
- [x] AC2013 Rodent Euthanasia
- [ ] AC2015 Chicken- Blood Collection
- [ ] AC2027 Gavage Procedure in Adult Rats
- [ ] AC2030 Vaginal Lavage in Rats
- [ ] AC2032 Tail Tip Biopsy - Mice
- [x] AC2038 Monitoring of Animals with Abnormalities
- [x] AC2061 Necropsy - Rodents & Lagomorphs
- [ ] AC2069 Housing Immunocompromised Mice in a Ventilated Rack
- [x] AC2072 Rodent ear notching for genotyping: weanling and adult
- [ ] AC2073 Mouse Gavage Procedure
- [ ] AC2074 Rodent Tattoo Identification
- [x] AC2075 Use of a Heating Lamp of Coils - Rodents
- [ ] AC2076 Guillotine and Sharp Scissor Use

- [x] **Husbandry**

- [ ] AC1013 BWC - Mouse Cage Changing
- [ ] AC1014 MSB - Rat Cage Changing
- [x] AC1023 BWC - Biosafety Level II Containment: Cage Changing Procedures for Mice Housed in a Negative Air Rack
- [ ] AC1030 BWC - Rat Cage Changing
- [ ] AC1037 MSB - Mouse Cage Changing
- [ ] AC1042 Temporary Laboratory Housing of Experimental Animals
- [ ] AC1043 Mouse Husbandry in the C.R. Semi-Rigid Isolator
- [ ] AC1047 Receiving Rodents and Rabbits from a Commercial Source

☒ AC2048 Rodent Husbandry - Breeding Mice (all animal units)
☐ AC2069 BWC - Housing Immunocompromised Animals in a Ventilated Rack
☐ AC3017 Processing of Cytotoxic Cages
☐ **Rabbits**
☒ **Rodents - Anaesthesia & Surgery**
☒ AC2003 Anaesthesia - Adult
☐ AC2005 Castration
☐ AC2008 Ovariectomy
☒ AC2013 Rodent - Euthanasia
☒ AC2040 Implantation of LinBit Insulin Release Implants
☐ AC2041 Irradiation of Tumours - Mice
☒ **Rodents - Blood Collections & Injections**
☒ AC2007 Handling & Injection Techniques
☒ AC2018 Cardiac Blood Collection in Rodents
☐ AC2019 Jugular Blood Collection in Rodents
☒ AC2020 Lateral Saphenous Vein Blood Collection in Rodents
☐ AC2029 Tail Blood Sampling - Rodents
☒ AC2049 Medial Saphenous Vein Blood Collection in the Mouse
☐ AC2064 Intranasal Inoculation - Adult Mice

Will Animal Care Services Staff be assisting with the use of SOP's?
☒ Yes ☐ No

Research Lab specific or other SOPs? Please list:
SOP MA 001- Diabetes Mellitus Induction in Rats
SOP MA 002- Surgical Wound Model - Rodent
SOP MA003- Diabetes Mellitus Induction in Mice
SOP MA004- Preparation of Streptozocin
SOP AC1050-Entery and Exit from biosafety level 2 area
SOP AC1023- Biosafty level II contaminment: Cage-changing procedures for a negative pressure ventilated rack
All infected mice with biosafety level 2 bacteria will be housed in isolation/ quarantine.

---

14. Description of Procedures

14a) Describe all procedures and techniques (reference SOPs where possible):

Diabetic wound models

Induction of Type I Diabetes in Rats.- Follow SOP MA001 - Diabetes Mellitus Induction in Rats

Induction of Type I Diabetes in C57 Mice- Follow SOP MA003- Diabetes Mellitus Induction in Mice.

Induction of Type I Diabetes in the db/db is unnecessary as mice that are homozygous for the diabetes spontaneous mutation manifest morbid obesity, chronic hyperglycemia, pancreatic beta cell atrophy

and become hypoinsulinemic. They will have an elevated blood sugar at 4-8 weeks of age.

For Rats only: A single subcutaneous insulin implant (Linplant Canada, Scarborough Ontario) will be inserted into the anaesthetized animal following SOP # AC2040 Implantation of Linbit Insulin Implant at the time of STZ injection to keep blood glucose at ~20mmol/l and to allow the rodents to maintain their body weight. Animals will have free access to 5% sucrose in water for the first 48 hours to guard against hypoglycemia in the unlikely event that diabetes induction is unsuccessful. A single dose of meloxicam will be provided to the animal for implant-associated pain control. Animals with low blood glucose (<3.5mM/L) will be supplemented with oral glucose as a supportive treatment until their glucose levels can be normalized to alleviate seizures and/or death as potential complications associated with low blood glucose. This is the recommended protocol for diabetes induction in rats.

For Mice only- Not all mice will be treated with insulin pellets. One or two insulin pellets will be added if blood sugar levels are very elevated (23-33mM/L) and the animal experiences clinical morbidity with scores of 2 in the categories of posture, movement, coat condition, eyes/nose, vocalization, body, or hydration. Insulin implants will be done following SOP # AC2040 Implantation of Linbit Insulin Implant. Animals will have free access to 5% sucrose in water for the first 48 hours to guard against hypoglycemia following insulin implantation. A single dose of meloxicam will be provided to the animal for implant-associated pain control. If blood sugar levels drop too low (<3.5mM/L) an insulin pellet will be removed. Animals with low blood glucose (<3.5mM/L) will be supplemented with oral glucose in water as a supportive treatment until their glucose levels can be normalized to guard against seizures and/or death as potential complications associated with low blood glucose. This is an industry standard protocol for diabetes induction in mice.

For both rats and mice:

a) Diabetes induction for the C57 mice will be confirmed by taking blood samples 2 days following STZ injection and every 2 weeks for the duration of the study following SOP #AC2020 Lateral Saphenous Vein Blood Collection in Rodents. Sample volumes will be ~40 - 70ul. Diabetes in the db/db mice will be confirmed after their acclimation period of 1 week. Blood samples will be taken every 2 weeks for the duration of the study following SOP #AC2020 Lateral Saphenous Vein Blood Collection in Rodents. Sample volumes will be ~40 - 70ul

b) Animals will be weighed at the time of diabetes induction (day 0), and at the time of blood sampling. Any animal whose body weight decreases by more than 10% will be weighed twice weekly until the end of the experiment, or until body weight has decreased by 15% (endpoint), whichever comes first.

Surgically induced wound- 2 full thickness skin wound (diameter of 5mm for mice and 8mm for rats) will be surgically created using a sterile punch biopsy instrument or scalpel blade under isoflurane anesthesia in the dorsal area following SOP MA002 Surgical Wound Model - Rodent. Meloxicam will be provided at the time of surgical wound induction for up to 3 days post-operatively. In addition, buprenorphine will be administered in the event that more pain control is required, based on clinical signs of self-trauma, swelling, hunching, squinting or piloerection.

Bandages will be applied under isoflurane anaesthesia directly after a wound has been created following SOP MA002 Surgical Wound Model - Rodent.

Rodents will either have a "smart" bandage, a"smart" bandage applied with growth factors and/or antibiotics or a commercial bandage (e.g. Tegaderm) or a linear incision sutured with the biocompatible polymer suture (polystyrene suture coated with thin layer of silk fibroin-polycaprolactone-gentamycin) . The biocompatible suture will be sterilized using autoclave or ethylene oxide prior to application. For each incision we use 3 separate suture knots. Wound splints (a sterile silicone ring) may be placed over bandages and sutured in place to secure the splint to the

skin. Wound splints will be applied under anesthesia either at the time of surgery, or at the same time the bandages are removed for photographs. If the splint needs to be re-applied, sutures will be placed at a different location than originally placed.

Photographs of the wounds will be taken under anesthesia. Photographs will be taken right after surgery to document initial wound area, and at weeks 1 and 4. At each time point, animals will be anaesthetized with isoflurane, following which photographs of each wound will be taken to document the wound area and then the same bandage will be re-applied. At weeks 1 and 4 , a designated group of animals will be euthanized, bandages will be removed and skin tissue samples at the wound site and healthy skin will be taken for PCR, histology and immunohistochemical staining.

Euthanasia: Animals will be euthanized by anaesthesia followed by cardiac exsanguination according to SOP AC2018. Following euthanasia, tissue samples will be collected for subsequent laboratory analysis.

Infected wound models

Model development: Surgically induced wound- 2 full thickness skin wound (diameter of 5mm for mice and 8mm for rats) will be surgically created using a sterile punch biopsy instrument under isoflurane anesthesia in the dorsal area following SOP MA002 Surgical Wound Model - Rodent. Before the surgery the lower back of the animal will be shaved and cleansed with antiseptic. Wound perimeters will be traced onto sterile transparencies to determine the initial wound area. Following wounding, mice will receive 50 uL of Tryptic Soy Broth (TSB) inocula of lag (2*10^5) and mid-log phase (2*10^7) E. Coli W3110 using a 200-uL pipette tips for each wound. The broth containing E.coli will be applied directly on the open wound. Animals in all groups except 1 and 5 will be dressed with GelDerm (per each wound) and secured with secondary wound dressing such as Tegaderm. Bandages will be applied under isoflurane anaesthesia directly after a wound has been created following SOP MA002 Surgical Wound Model - Rodent. Rodents will be monitored daily and appendix 2 (Diabetic and wound model rodent monitoring sheet) outlines scoring and criteria for intervention/euthanasia.

For animals with no infection, dressing will be changed everyday under isoflurane anesthesia. During the changing of dressings, photographs of the wound will be taken, pH of the wound will be measure using pH strips, and swab samples will be taken for culture.

For infected animals, the dressing will remain on the wound and photographs of the smart bandage will be taken at t=0, 1, 2, 4, 6, 8, 10, 12, 18, 24, 36, 48, 72, 96, 120, 144, and 168 hours (unless animal is euthanized early for humane reasons - described under 14c, below).

*** infected wound model using Biosafety level 2 Bacteria***

Model development: Surgically induced wound- 2 full thickness skin wound (diameter of 5mm for mice) will be surgically created using a sterile punch biopsy instrument under isoflurane anesthesia in the dorsal area following SOP MA002 Surgical Wound Model - Rodent. Before the surgery the lower back of the animal will be shaved and cleansed with antiseptic. Wound perimeters will be traced onto sterile transparencies to determine the initial wound area. Following wounding, mice will receive 50 uL of Tryptic Soy Broth (TSB) inocula of lag (2*10^5) and mid-log phase (2*10^7) of biosaftey level 2 bacteria (listed in Table 15c) using a 200-uL pipette tips for each wound. The broth containing bacteria will be applied directly on the open wound and this procedure will be performed under class 2 biological safety cabinet since procedures likely to generate aerosols that possess low risk to public health and the animal population. Animals did not receive any topical or bandage treatment . animals will be monitored daily and appendix 2 (Diabetic and wound model rodent monitoring sheet) outlines scoring and criteria for intervention/euthanasia.

The pH of the wound will be measured using pH meter, and swab samples will be taken for culture every day. The whole procedure will be conducted following level II containment guidelines .

14b) Experimental endpoint:

Animals will be euthanized at weeks 1,2 and 4 following wound induction. The pilot experiment is completed 4 weeks after wound induction.
Animals infected with biosafety level 2 bacteria will be euthanized at week 2.

14c) Clinical endpoint:

Diabetic wound models

Clinical endpoints will be assessed following the outline in Appendix 1 (Clinical Endpoints). Animals scoring 1 in more than one category will either be treated medically, or euthanized. If medicated, animals that do not respond to appropriate treatment within 1 - 5 days (depending on condition and treatment) will be euthanized.

Rodents with surgically induced skin wound: Appendix 2 (Diabetic and wound model rodent monitoring sheet) outlines scoring and criteria for intervention/euthanasia.

Clinical Endpoints for STZ- induced and db/db rodents: Appendix 2 (Diabetic and wound model rodent monitoring) outlines assessment of STZ - induced and db/db rodents and criteria for intervention/euthanasia. Any animal scoring 2 or 3 in categories of posture, movement, coat condition, eyes/nose, vocalization, body, or hydration will be treated as recommended by ACS staff or veterinarian, or euthanized. Any animal scoring 3 in alertness, activity, movement, distended abdomen and breathing will be euthanized. Animals that do not respond to appropriate medical treatment within 1 - 5 days (depending on condition and treatment) will be euthanized.
Rodents with insulin implant- If blood sugar levels drop too low (<3.5mM/L) an insulin pellet will be removed. If blood sugar levels are very elevated (23-33mM/L) and the animal scores 2 or 3 in categories posture, movement, coat condition, eyes/nose, vocalization, body, or hydration , one or two insulin pellets will be added, respectively. Animals with low blood glucose (<3.5mM/L) will be supplemented with oral glucose as a supportive treatment until their glucose levels can be normalized to prevent seizures and/or death as potential complications associated with low blood glucose.

Body Weights: Weight loss of >15% from the induction weight that does not respond to intervention (i.e. high calorie food) within 7 days will result in euthanasia. "Response" is determined by a stabilization of weight loss at 15% or less from induction weight, or gaining of weight from maximum weight loss.

Animals will be euthanized if wounds become infected, no treatment of antibiotics will be administered.

Infected wound models

Rodents with infected skin wound: Appendix 2 (Diabetic and wound model rodent monitoring sheet) outlines scoring and criteria for intervention/euthanasia.

14d) Monitoring:

All Groups: All groups of animals will have a daily visual check done daily by ACS staff, with observations recorded on the monitoring form (Appendix 2 - Monitoring Form). Body weights will be taken on all animals 1 week after arrival, prior to any procedures, and at a minimum every 2 weeks for the duration of the study.

Any animal experiencing weight loss of 10% or more will be provided with high calorie food, and weighed at

least twice per week until the end of the study.
Blood glucose will be measured and recorded 2 days following STZ injection and every 2 weeks for the duration of the study. Blood glucose for db/db mouse model will be taken just after acclimation and every 2 weeks for the duration of the study.

Surgical Procedures and Recovery: ACS staff will be responsible for monitoring animals using SOP AC2038 as well as the use of Clinical Endpoints (Appendix 1) in the following manner:
(a) Twice per day for the first 2 days following surgery, then
(b) Once daily for the next 7 days.

All other animals are monitored daily by ACS staff, as normal following SOP AC2038. Observations specific to STZ, diabetic animals, infection and the bandage experiment will be documented following Appendix 2 - Diabetic and Wound Model Monitoring Form.

Surgical records are maintained using the Rodent Anesthesia Record (Appendix 3).
Monitoring of post-operative animals is documented using the Rodent Anesthesia Record.
Monitoring of medical abnormalities separate from the experimental model are documented using the ACS Morbidity Form (found in AC2038).

Bandage application: Bandages will be checked once daily. Outer bandages will be re-applied as necessary if they become soiled or damaged. If a wound splint is applied or the area has been sutured using the biocompatible suture material, they can be re-applied or repaired a maximum of twice outside of the week 1 and week 4 photograph time points. Animals will require anesthesia to re-apply the wound splint or suture.

14e) Morbidity rate:

All animals will experience expected morbidity associated with the induction of diabetes, and surgical wounding. Morbidity associated with diabetes includes increased urination and thirst, sub-clinical dehydration, and weight loss. Up to ~5% of animals may experience weight loss up to 15%, and low blood glucose when treated with insulin. Up to 5% of animals may experience surgical complications including wound infection and self-trauma. Up to 10% of induced wound infection model may experience morbidity, particularly where animals are not treated with antibiotics. Up to 20% of induced wound infection model with biosafety level II may experience morbidity, particularly where animals are not treated with antibiotics as a result of inflammation, self-trauma , weight loss and pain.

15. Drugs / Chemicals / Biologicals / Anaesthetic

15a) Pre-Anesthetic / Anaesthetic / Analgesic Agents

Add Item

	Species	Agent	Dosage	Total volume (ml) per administration	Route	Frequency / Duration	Purpose
X	Rat and mouse	Isoflurane	2-5%	1L/min (vaporized)	inhalation	Sessions will occur every 24 hours for up to 28 days. Duration of each anesthesia procedure will be ~15 minutes	STZ injection/ LinBit implantation, wound induction, photography, splint/bandage application
X	Rat/Mouse	Meloxicam	1-2mg/kg (Rat) 5mg/kg (Mouse)	0.3 - 1.0ml Rat (diluted) 0.1 - 0.3ml Mouse (diluted)	SC, oral or in gel	SC & oral- every 24 hours 3-7 days as needed meloxicam in gel will be placed in cage up to 7 days	Pain control

X	Rat and mouse	Lidocaine 2%	1mg/kg	up to 1.0ml (diluted)	SC	once at each wound induction site	local anesthetic - pain control
X	Rat and mouse	Bupivacaine 0.125%	1mg/kg	up to 1.0ml (diluted)	SC	once at each wound induction site	local anesthetic,- pain control
X	Rat and mouse	Buprenorphine	0.01-0.05mg/ kg (Rat) 0.05-0.1mg/kg (Mouse)	0.3 - 1.0ml Rat (diluted) 0.05 - 0.3ml Mouse (diluted)	SC	every 12 hours for up to 4 days as needed	Pain control
X							

15b) Clinical drugs including antibiotic

Add Item

	Species	Agent	Dosage	Total volume (ml) per administration	Route	Frequency / Duration	Purpose
X	mice	Enrofloxacin	0.05-0.2 mg/ml	ad lib	oral (drinking water)	14 days	antimicrobial
X							
X							

15c) All other substances administered to animals

Add Item

	Species	Agent	Dosage	Total volume (ml) per administration	Route	Frequency / Duration	Purpose
X	Rat and mouse	VEGF-loaded Gel Derm	100-500ng per mg of dressing	10 ug-50 ug	Topical	once	wound-healing (experimental)
X	Rat and mouse	bFGF-loaded Gel Derm	100-500ng per mg of dressing	10 ug-50 ug	Topical	once	wound-healing (experimental)
X	Rat and mouse	VEGF & bFGF - loaded Gel Derm	100-500ng of each per mg of dressing	10 ug-50 ug	Topical	once	wound-healing (experimental)
X	Rat and mouse	0.9% NaCl	0.2 - 0.9ml as diluent	0.2 - 0.9ml as diluent	SC	up to twice as diluent for local anaesthetic, up to 8 times as used for diluent with pain control, once as diluent for streptozotocin	Diluent
X	Rat	Streptozotocin	60mg/kg	0.05-0.5ml	IV	once	Diabetes induction
X	Mouse	Streptozotocin	75mg/kg	0.05-0.15ml	IP	up to three doses	Diabetes induction
X	Mouse	Tryptic Soy Broth (TSB)	50uL	50uL	Topical	once	culture broth for E.coli
X	Mouse	E. Coli W3110	lag (2*10^5) and mid-log phase (2*10^7)	50uL	Topical	once	wound infection

X	Mouse	Staphylococcus aureus (ATCC 29213)	lag (2*10^5) and mid-log phase (2*10^7)	50uL	Topical	once	wound infection
X	Mouse	Staphylococcus lugdunensis (ATCC 700328)	lag (2*10^5) and mid-log phase (2*10^7)	50uL	Topical	once	wound infection
X	Mouse	Staphylococcus epidermidis (ATCC 12228)	lag (2*10^5) and mid-log phase (2*10^7)	50uL	Topical	once	wound infection
X	Mouse	Staphylococcus capitis (ATCC 35661)	lag (2*10^5) and mid-log phase (2*10^7)	50uL	Topical	once	wound infection
X	Mouse	Corynebacterium striatum (ATCC 1293)	lag (2*10^5) and mid-log phase (2*10^7)	50uL	Topical	once	wound infection
X	Mouse	Acinetobacter baumannii (ATCC 19606)	lag (2*10^5) and mid-log phase (2*10^7)	50uL	Topical	once	wound infection
X	Mouse	Citrobacter koseri (ATCC 27156)	lag (2*10^5) and mid-log phase (2*10^7)	50uL	Topical	once	wound infection
X	Mouse	pseudomonas aeruginosa (ATCC 27853)	lag (2*10^5) and mid-log phase (2*10^7)	50uL	Topical	once	wound infection
X	Mouse	pseudomonas putida (MIFF-F03-BC729-3-7)	lag (2*10^5) and mid-log phase (2*10^7)	50uL	Topical	once	wound infection
X	Mouse	stenotrophomonas maltophilia (ATCC 17666)	lag (2*10^5) and mid-log phase (2*10^7)	50uL	Topical	once	wound infection
X	Mouse	alcaligenes faecalis (ATCC 35655)	lag (2*10^5) and mid-log phase (2*10^7)	50uL	Topical	once	wound infection
X	Mouse	aeromonas hydrophila (ATCC 35654)	lag (2*10^5) and mid-log phase (2*10^7)	50uL	Topical	once	wound infection

16. Euthanasia

16a) Method of euthanasia

Add Item

	Species	Method	List Agent / Dose / Route (if applicable)
X	Rat	Anesthetic overdose followed by cervical dislocation or exsanguination	Isoflurane 5% inhalation
X	Mouse	Anesthetic overdose followed by cervical dislocation or exsanguination	Isoflurane 5% inhalation
X			

16b) Final disposition of animals if not euthanized:

N/A all animals are euthanized.

17. Hazardous Agents

It is the responsibility of the investigator to obtain the necessary UVic Biosafety Committee and/or UVic Radiation Safety Committee permits before this protocol is submitted for review.

☐ No hazardous materials will be used in this study.

17a) Indicate which of the following will be used in animals:

☒ Infectious/Biological agents (includes vectors) ☒ Hazardous chemicals ☒ Carcinogens
☐ Transplantable tumours and/or tissues ☐ Radioisotopes

UVic Radiation Certificate Number: _____ UVic Biosafety Certificate Number: 47994-082

17b) After administration the animals will be housed in:

☒ Bob Wright Animal Care Unit ☐ Medical Sciences Animal Care Unit
☐ Outdoor Aquatic Unit ☐ Investigator/Teaching Laboratory
☐ Other (please specify building and room number) _____

Please note that cages must be appropriately labeled at all times.

17c) Describe potential health risk(s) to humans or animals:

Buprenorphine is considered a potential skin irritant for humans.
Isoflurane- Overexposure by inhalation to the vapors may cause temporary nervous system depression with anesthetic effects such as dizziness, headache, confusion, in-coordination, or loss of consciousness. May cause skin and eye irritation
STZ is a potential carcinogen. Please refer to SOP MA005 Preparation of Streptozocin.
E.coli W3110 is a Risk Group Level 1 pathogen. It may cause disease in healthy individuals but is not likely to do so.
A bacterial level 2 poses a moderate risk to the health of individuals or animals, and a low risk to public health and the animal population. These pathogens are able to cause serious disease in a human or animal but are unlikely to do so. Effective treatment and preventive measures are available and the risk of spread of diseases caused by these pathogens is low. Experiments that increase the risks posed by a pathogen can impact both the researcher and the community. For example, modifying a pathogen to become transmissible by the airborne route would increase the risks inherent in certain laboratory procedures that generate aerosols, as well as the impact on public or animal health if released from the laboratory.
There are some possible ways to minimize and mitigate the risk as follow:
1.Understanding the legislative requirements related to conducting activities with such material (e.g.,

importing, handling, and possessing), as well as the abilities of the individuals concerned and the limitations of the facilities where the material is being handled and stored.
2. Personnel working with animals, facility maintenance employees, and other staff that may need to enter the facility are to have specific training in animal facility procedures.
3.The PPE selected and worn by individuals to reduce or minimize the potential exposure to infectious material or toxins.
4. Biological safety cabinets (BSCs) provide effective primary containment for work with infectious material when they are properly maintained and used in conjunction with good microbiological laboratory practices.
5. The safe and effective decontamination of all waste, including animal waste, is critical to containment.

17d) Describe measures that will be used to reduce risk to the environment and all project and animal facility personnel:

Gloves and laboratory coats will be used with all drugs.
Isoflurane will be used with an anesthetic machine equipped with a precision vaporizer and calibrated annually. All staff or researchers using the anesthetic machine will be required to do the Anesthesia Course offered through Animal Care Services.
Safety goggles, gloves and N95 respirators must be used when making STZ and working with biosaftey level II bacteria. A fume hood or Type B2 BSC should be used for STZ preparation where possible. Refer to SOP MA004 Preparation of Streptozocin.
For the preparation and use of E.coli gloves, eye protection and lab coats must be worn.

17e) If using cell lines, have they been tested?

☐ Yes If yes, what human and/or animal pathogens have been tested:

N/A

☐ No If no, please justify:

N/A

Upon completion of the form, save and then email to acsc@uvic.ca. Print pages one & two, obtain the necessary signatures, and forward to the Animal Ethics Liaison, Office of Research Services (ASB room B202).

Bibliography

[1] D. Gerteisen, T. Heilmann, and C. Ziegler, "Enhancing liquid water transport by laser perforation of a GDL in a PEM fuel cell," *Journal of Power Sources*, vol. 177, no. 2, pp. 348–354, 2008.

[2] M. P. Manahan, J. T. Clement, A. K. Srouji, S. W. Brown, T. Reutzel, and M. M. Mench, "Laser modified fuel cell diffusion media: Engineering enhanced performance via localized water redistribution," *Journal of the Electrochemical Society*, vol. 161, no. 10, pp. F1061–F1069, 2014.

[3] T. Fabian, R. OHayre, S. Litster, F. B. Prinz, and J. G. Santiago, "Active water management at the cathode of a planar air-breathing polymer electrolyte membrane fuel cell using an electroosmotic pump," *Journal of Power Sources*, vol. 195, no. 11, pp. 3640–3644, 2010.

[4] T. Fabian, R. OHayre, S. Litster, F. B. Prinz, and J. G. Santiago, "Passive water management at the cathode of a planar air-breathing proton exchange membrane fuel cell," *Journal of Power Sources*, vol. 195, no. 10, pp. 3201–3206, 2010.

[5] A. Forner-Cuenca, J. Biesdorf, L. Gubler, P. M. Kristiansen, T. J. Schmidt, and P. Boillat, "Engineered water highways in fuel cells: Radiation grafting of gas diffusion layers," *Advanced Materials*, vol. 27, no. 41, pp. 6317–6322, 2015.

[6] H. Li, Y. Tang, Z. Wang, Z. Shi, S. Wu, D. Song, J. Zhang, K. Fatih, J. Zhang, H. Wang, Z. Liu, R. Abouatallah, and A. Mazza, "A review of water flooding issues in the proton exchange membrane fuel cell," *Journal of Power Sources*, vol. 178, no. 1, pp. 103–117, 2008.

[7] T. Berning and N. Djilali, "A 3D, Multiphase, Multicomponent Model of the Cathode and Anode of a PEM Fuel Cell," *Journal of The Electrochemical Society*, vol. 150, no. 12, p. A1589, 2003.

[8] U. Pasaogullari and C. Y. Wang, "Liquid Water Transport in Gas Diffusion Layer of Polymer Electrolyte Fuel Cells," *Journal of The Electrochemical Society*, vol. 151, no. 3, p. A399, 2004.

[9] M. F. Mathias, J. Roth, J. Fleming, and W. Lehnert, "Diffusion media materials and characterisation," in *Handbook of Fuel Cells*, vol. 3, pp. 517–537, 2010.

[10] A. Rofaiel, J. S. Ellis, P. R. Challa, and A. Bazylak, "Heterogeneous through-plane distributions of polytetrafluoroethylene in polymer electrolyte membrane fuel cell gas diffusion layers," *Journal of Power Sources*, vol. 201, pp. 219–225, 2012.

[11] Z. Fishman and A. Bazylak, "Heterogeneous through-plane porosity distributions for treated PEMFC GDLs I. PTFE effect," *Journal of the Electrochemical Society*, vol. 158, no. 8, pp. B841–B845, 2011.

[12] W. K. Lee, C. H. Ho, J. W. Van Zee, and M. Murthy, "Effects of compression and gas diffusion layers on the performance of a PEM fuel cell," *Journal of Power Sources*, vol. 84, no. 1, pp. 45–51, 1999.

[13] N. Djilali, "Computational modelling of polymer electrolyte membrane (PEM) fuel cells: Challenges and opportunities," *Energy*, vol. 32, no. 4, pp. 269–280, 2007.

[14] S. Litster, D. Sinton, and N. Djilali, "Ex situ visualization of liquid water transport in PEM fuel cell gas diffusion layers," *Journal of Power Sources*, vol. 154, no. 1, pp. 95–105, 2006.

[15] A. Bazylak, D. Sinton, Z.-S. Liu, and N. Djilali, "Effect of compression on liquid water transport and microstructure of PEMFC gas diffusion layers," *Journal of Power Sources*, vol. 163, no. 2, pp. 784–792, 2007.

[16] R. Flückiger, F. Marone, M. Stampanoni, A. Wokaun, and F. N. Büchi, "Investigation of liquid water in gas diffusion layers of polymer electrolyte fuel cells using X-ray tomographic microscopy," *Electrochimica Acta*, vol. 56, no. 5, pp. 2254–2262, 2011.

[17] A. Bazylak, "Liquid water visualization in PEM fuel cells: a review," *International Journal of Hydrogen Energy*, vol. 34, no. 9, pp. 3845–3857, 2009.

[18] A. Forner-Cuenca, J. Biesdorf, A. Lamibrac, V. Manzi-Orezzoli, F. N. Bchi, L. Gubler, T. J. Schmidt, and P. Boillat, "Advanced Water Management in PEFCs: Diffusion Layers with Patterned Wettability II. Measurement of Capillary Pressure Characteristic with Neutron and Synchrotron Imaging," *Journal of the Electrochemical Society*, vol. 163, no. 9, pp. F1038–F1048, 2016.

[19] R. T. White, F. P. Orfino, M. E. Hannach, O. Luo, M. Dutta, A. P. Young, and E. Kjeang, "3D Printed Flow Field and Fixture for Visualization of Water Distribution in Fuel Cells by X-ray Computed Tomography," *Journal of The Electrochemical Society*, vol. 163, no. 13, pp. F1337–F1343, 2016.

[20] E. J. Xu H, Bührer M, Marone F, Schmidt T, Büchi F, "Fighting the Noise: Towards the Limits of Subsecond X-ray Tomographic Microscopy of PEFC H. Xu," in *ECS Transactions*, vol. 80, pp. 395–402, 2017.

[21] I. V. Zenyuk, D. Y. Parkinson, G. Hwang, and A. Z. Weber, "Probing water distribution in compressed fuel-cell gas-diffusion layers using X-ray computed tomography," *Electrochemistry Communications*, vol. 53, pp. 24–28, 2015.

[22] Y. Wu, J. I. Cho, X. Lu, L. Rasha, T. P. Neville, J. Millichamp, R. Ziesche, N. Kardjilov, H. Markötter, P. Shearing, and D. J. Brett, "Effect of compression on the water management of polymer electrolyte fuel cells: An in-operando neutron radiography study," *Journal of Power Sources*, vol. 412, no. December 2018, pp. 597–605, 2019.

[23] S. M. Moosavi, M. Niffeler, J. Gostick, and S. Haussener, "Transport characteristics of saturated gas diffusion layers treated with hydrophobic coatings," *Chemical Engineering Science*, vol. 176, pp. 503–514, 2018.

[24] A. Ozden, S. Shahgaldi, X. Li, and F. Hamdullahpur, "A review of gas diffusion layers for proton exchange membrane fuel cells—With a focus on characteristics, characterization techniques, materials and designs," *Progress in Energy and Combustion Science*, vol. 74, pp. 50–102, 2019.

[25] E. Sadeghi, N. Djilali, and M. Bahrami, "Effective thermal conductivity and thermal contact resistance of gas diffusion layers in proton exchange mem-

brane fuel cells. Part 1: Effect of compressive load," *Journal of Power Sources*, vol. 196, no. 1, pp. 246–254, 2011.

[26] G. Xu, J. M. Lamanna, J. T. Clement, and M. M. Mench, "Direct measurement of through-plane thermal conductivity of partially saturated fuel cell diffusion media," *Journal of Power Sources*, vol. 256, pp. 212–219, 2014.

[27] S. Hasanpour, M. Ahadi, M. Bahrami, N. Djilali, and M. Akbari, "Woven gas diffusion layers for polymer electrolyte membrane fuel cells: Liquid water transport and conductivity trade-offs," *Journal of Power Sources*, vol. 403, 2018.

[28] E. Sadeghi, N. Djilali, and M. Bahrami, "A novel approach to determine the in-plane thermal conductivity of gas diffusion layers in proton exchange membrane fuel cells," *Journal of Power Sources*, vol. 196, no. 7, pp. 3565–3571, 2011.

[29] P. Teertstra, G. Karimi, and X. Li, "Measurement of in-plane effective thermal conductivity in PEM fuel cell diffusion media," *Electrochimica Acta*, vol. 56, no. 3, pp. 1670–1675, 2011.

[30] Z. Zhan, H. Zhao, P. C. Sui, P. Jiang, M. Pan, and N. Djilali, "Numerical analysis of ice-induced stresses in the membrane electrode assembly of a PEM fuel cell under sub-freezing operating conditions," *International Journal of Hydrogen Energy*, vol. 43, no. 9, pp. 4563–4582, 2018.

[31] M. Blanco, *Study of selected water management strategies for proton exchange membrane fuel cells*. PhD thesis, The University of British Columbia, 2011.

[32] G. Okuhata, T. Tonoike, K. Nishida, S. Tsushima, and S. Hirai, "Effect of perforation structure of cathode GDL on liquid water removal in PEFC," *ECS Transactions*, vol. 58, no. 1, pp. 1047–1057, 2013.

[33] M. P. Manahan, M. C. Hatzell, E. C. Kumbur, and M. M. Mench, "Laser perforated fuel cell diffusion media. Part I: Related changes in performance and water content," *Journal of Power Sources*, vol. 196, no. 13, pp. 5573–5582, 2011.

[34] M. P. Manahan and M. M. Mench, "Laser perforated fuel cell diffusion media: engineered interfaces for improved ionic and oxygen transport," *Journal of the Electrochemical Society*, vol. 159, no. 7, pp. F322–F330, 2012.

[35] R. Omrani and B. Shabani, "Gas diffusion layer modifications and treatments for improving the performance of proton exchange membrane fuel cells and electrolysers : A review," *International Journal of Hydrogen Energy*, pp. 1–22, 2017.

[36] M. D. Kok, R. Jervis, D. Brett, P. R. Shearing, and J. T. Gostick, "Insights into the Effect of Structural Heterogeneity in Carbonized Electrospun Fibrous Mats for Flow Battery Electrodes by X-Ray Tomography," *Small*, vol. 14, no. 9, pp. 1–15, 2018.

[37] J. H. Chun, K. T. Park, D. H. Jo, J. Y. Lee, S. G. Kim, S. H. Park, E. S. Lee, J. Y. Jyoung, and S. H. Kim, "Development of a novel hydrophobic/hydrophilic double micro porous layer for use in a cathode gas diffusion layer in PEMFC," *International Journal of Hydrogen Energy*, vol. 36, no. 14, pp. 8422–8428, 2011.

[38] A. Forner-Cuenca, V. Manzi-Orezzoli, J. Biesdorf, M. El Kazzi, D. Streich, L. Gubler, T. J. Schmidt, and P. Boillat, "Advanced Water Management in PEFCs: Diffusion Layers with Patterned Wettability I. Synthetic Routes, Wettability Tuning and Thermal Stability," *Journal of the Electrochemical Society*, vol. 163, no. 8, pp. F788–F801, 2016.

[39] A. Forner-Cuenca, J. Biesdorf, V. Manzi-Orezzoli, L. Gubler, T. J. Schmidt, and P. Boillat, "Advanced Water Management in PEFCs: Diffusion Layers with Patterned Wettability III. Operando Characterization with Neutron Imaging," *Journal of the Electrochemical Society*, vol. 163, no. 13, pp. F1389–F1398, 2016.

[40] R. J. Gene Kim, Kelley and U. S. D. Pratt, "FUEL CELL HAVING A THERMO-RESPONSIVE POLYMER INCORPORATED THEREIN," 2004.

[41] G. Zhang, L. Guo, L. Ma, and H. Liu, "Simultaneous measurement of current and temperature distributions in a proton exchange membrane fuel cell," *Journal of Power Sources*, vol. 195, no. 11, pp. 3597–3604, 2010.

[42] H. Pei, Z. Liu, H. Zhang, Y. Yu, Z. Tu, Z. Wan, and W. Liu, "In situ measurement of temperature distribution in proton exchange membrane fuel cell i a hydrogen-air stack," *Journal of Power Sources*, vol. 227, pp. 72–79, 2013.

[43] H. Shao, D. Qiu, L. Peng, P. Yi, and X. Lai, "In-situ measurement of temperature and humidity distribution in gas channels for commercial-size proton

exchange membrane fuel cells," *Journal of Power Sources*, vol. 412, no. November 2018, pp. 717–724, 2019.

[44] H. Lin, T. F. Cao, L. Chen, Y. L. He, and W. Q. Tao, "In situ measurement of temperature distribution within a single polymer electrolyte membrane fuel cell," *International Journal of Hydrogen Energy*, vol. 37, no. 16, pp. 11871–11886, 2012.

[45] C. Y. Lee, W. Y. Fan, and C. P. Chang, "A novel method for in-situ monitoring of local voltage, temperature and humidity distributions in fuel cells using flexible multi-functional micro sensors," *Sensors*, vol. 11, no. 2, pp. 1418–1432, 2011.

[46] C. Y. Lee, F. B. Weng, S. M. Chuang, S. J. Lee, Y. P. Huang, Y. T. Cheng, and C. K. Cheng, "Flexible five-in-one micro sensor for in-situ diagnosis of high-temperature proton exchange membrane fuel cell stack," *International Journal of Hydrogen Energy*, vol. 40, no. 45, pp. 15679–15689, 2015.

[47] C. Y. Lee, W. J. Hsieh, and G. W. Wu, "Embedded flexible micro-sensors in MEA for measuring temperature and humidity in a micro-fuel cell," *Journal of Power Sources*, vol. 181, no. 2, pp. 237–243, 2008.

[48] S. Basu, M. W. Renfro, H. Gorgun, and B. M. Cetegen, "In situ simultaneous measurements of temperature and water partial pressure in a PEM fuel cell under steady state and dynamic cycling," *Journal of Power Sources*, vol. 159, no. 2, pp. 987–994, 2006.

[49] K. Inman, X. Wang, and B. Sangeorzan, "Design of an optical thermal sensor for proton exchange membrane fuel cell temperature measurement using phosphor thermometry," *Journal of Power Sources*, vol. 195, no. 15, pp. 4753–4757, 2010.

[50] K. Inman and X. Wang, "In-Situ Temperature Measurement on Cathode GDL in a PEMFC Using an Optical Fiber Temperature Sensor," *Journal of The Electrochemical Society*, vol. 160, no. 6, pp. F496–F500, 2013.

[51] N. A. David, P. M. Wild, J. Hu, and N. Djilali, "In-fibre Bragg grating sensors for distributed temperature measurement in a polymer electrolyte membrane fuel cell," *Journal of Power Sources*, vol. 192, no. 2, pp. 376–380, 2009.

[52] N. A. David, P. M. Wild, J. Jensen, T. Navessin, and N. Djilali, "Simultaneous In Situ Measurement of Temperature and Relative Humidity in a PEMFC Using Optical Fiber Sensors," *Journal of The Electrochemical Society*, vol. 157, no. 8, p. B1173, 2010.

[53] N. A. David, P. M. Wild, and N. Djilali, "Parametric study of a polymer-coated fibre-optic humidity sensor," *Measurement Science and Technology*, vol. 23, no. 3, 2012.

[54] N. David, *Fiber Optic Sensors for PEM Fuel Cells*. PhD thesis, University of Victoria, 2011.

[55] S. R. Larimi, H. Rezaei Nejad, M. Oyatsi, A. O'Brien, M. Hoorfar, and H. Najjaran, "Low-cost ultra-stretchable strain sensors for monitoring human motion and bio-signals," *Sensors and Actuators, A: Physical*, vol. 271, pp. 182–191, 2018.

[56] H. Montazerian, A. Rashidi, A. Dalili, H. Najjaran, A. S. Milani, and M. Hoorfar, "Graphene-Coated Spandex Sensors Embedded into Silicone Sheath for Composites Health Monitoring and Wearable Applications," *Small*, vol. 15, no. 17, pp. 1–12, 2019.

[57] J. Shi, S. Liu, L. Zhang, B. Yang, L. Shu, Y. Yang, M. Ren, Y. Wang, J. Chen, W. Chen, Y. Chai, and X. Tao, "Smart Textile-Integrated Microelectronic Systems for Wearable Applications," vol. 1901958, pp. 1–37, 2020.

[58] G. Zhou, J. H. Byun, Y. Oh, B. M. Jung, H. J. Cha, D. G. Seong, M. K. Um, S. Hyun, and T. W. Chou, "Highly Sensitive Wearable Textile-Based Humidity Sensor Made of High-Strength, Single-Walled Carbon Nanotube/Poly(vinyl alcohol) Filaments," *ACS Applied Materials and Interfaces*, vol. 9, no. 5, pp. 4788–4797, 2017.

[59] B. S. Shim, W. Chen, C. Doty, C. Xu, and N. A. Kotov, "Smart electronic yarns and wearable fabrics for human biomonitoring made by carbon nanotube coating with polyelectrolytes," *Nano Letters*, vol. 8, no. 12, pp. 4151–4157, 2008.

[60] D. H. Ho, Q. Sun, S. Y. Kim, J. T. Han, D. H. Kim, and J. H. Cho, "Stretchable and Multimodal All Graphene Electronic Skin," *Advanced Materials*, vol. 28, no. 13, pp. 2601–2608, 2016.

[61] C. Lv, C. Hu, J. Luo, S. Liu, Y. Qiao, Z. Zhang, J. Song, Y. Shi, J. Cai, and A. Watanabe, "Recent Advances in Graphene-Based Humidity Sensors," *Nanomaterials*, vol. 9, no. 3, p. 422, 2019.

[62] H. Farahani, R. Wagiran, and M. N. Hamidon, *Humidity Sensors Principle, Mechanism, and Fabrication Technologies: A Comprehensive Review*. 2014.

[63] M. Mehrali, S. Bagherifard, M. Akbari, A. Thakur, B. Mirani, M. Mehrali, M. Hasany, G. Orive, P. Das, J. Emneus, T. L. Andresen, and A. Dolatshahi-pirouz, "Blending Electronics with the Human Body : A Pathway toward a Cybernetic Future," 2018.

[64] Q. Li, H. Chen, Z. Y. Ran, L. N. Zhang, R. F. Xiang, X. Wang, X. M. Tao, and X. Ding, "Full fabric sensing network with large deformation for continuous detection of skin temperature," *Smart Materials and Structures*, vol. 27, no. 10, 2018.

[65] G. Rosace, V. Trovato, C. Colleoni, M. Caldara, V. Re, M. Brucale, E. Piperopoulos, E. Mastronardo, C. Milone, G. De Luca, and M. R. Plutino, "Structural and morphological characterizations of MWCNTs hybrid coating onto cotton fabric as potential humidity and temperature wearable sensor," *Sensors and Actuators, B: Chemical*, vol. 252, pp. 428–439, 2017.

[66] P. Mostafalu, M. Akbari, K. A. Alberti, Q. Xu, A. Khademhosseini, and S. R. Sonkusale, "A toolkit of thread-based microfluidics, sensors, and electronics for 3D tissue embedding for medical diagnostics," *Microsystems and Nanoengineering*, vol. 2, no. March, 2016.

[67] J. W. Lee, D. C. Han, H. J. Shin, S. H. Yeom, B. K. Ju, and W. Lee, "PEDOT:PSS-based temperature-detection thread for wearable devices," *Sensors (Switzerland)*, vol. 18, no. 9, pp. 2–9, 2018.

[68] W. Honda, S. Harada, T. Arie, S. Akita, and K. Takei, "Wearable, human-interactive, health-monitoring, wireless devices fabricated by macroscale print-

ing techniques," *Advanced Functional Materials*, vol. 24, no. 22, pp. 3299–3304, 2014.

[69] A. El-Kharouf, T. J. Mason, D. J. Brett, and B. G. Pollet, "Ex-situ characterisation of gas diffusion layers for proton exchange membrane fuel cells," *Journal of Power Sources*, vol. 218, pp. 393–404, 2012.

[70] S. Park and B. N. Popov, "Effect of a GDL based on carbon paper or carbon cloth on PEM fuel cell performance," *Fuel*, vol. 90, no. 1, pp. 436–440, 2011.

[71] J. Benziger, J. Nehlsen, D. Blackwell, T. Brennan, and J. Itescu, "Water flow in the gas diffusion layer of PEM fuel cells," *Journal of Membrane Science*, vol. 261, no. 1, pp. 98–106, 2005.

[72] S. G. Kandlikar, M. L. Garofalo, and Z. Lu, "Water management in a PEMFC: Water transport mechanism and material degradation in gas diffusion layers," *Fuel Cells*, vol. 11, no. 6, pp. 814–823, 2011.

[73] Z. Lu, M. M. Daino, C. Rath, and S. G. Kandlikar, "Water management studies in PEM fuel cells, part III: Dynamic breakthrough and intermittent drainage characteristics from GDLs with and without MPLs," *International Journal of Hydrogen Energy*, vol. 35, no. 9, pp. 4222–4233, 2010.

[74] S. Hasanpour, M. Hoorfar, and A. B. Phillion, "Characterization of transport phenomena in porous transport layers using X-ray microtomography," *Journal of Power Sources*, vol. 353, pp. 221–229, 2017.

[75] K. Yoshizawa, K. Ikezoe, Y. Tasaki, D. Kramer, E. H. Lehmann, and G. G. Scherer, "Analysis of gas diffusion layer and flow-field design in a PEMFC using neutron radiography," *Journal of the Electrochemical Society*, vol. 155, no. 3, pp. B223–B227, 2008.

[76] M. Ahadi, M. Tam, M. S. Saha, J. Stumper, and M. Bahrami, "Thermal conductivity of catalyst layer of polymer electrolyte membrane fuel cells: Part 1Experimental study," *Journal of Power Sources*, vol. 354, pp. 207–214, 2017.

[77] M. Ahadi, M. Andisheh-Tadbir, M. Tam, and M. Bahrami, "An improved transient plane source method for measuring thermal conductivity of thin films: Deconvoluting thermal contact resistance," *International Journal of Heat and Mass Transfer*, vol. 96, pp. 371–380, 2016.

[78] O. Burheim, P. J. S. Vie, J. G. Pharoah, and S. Kjelstrup, "Ex situ measurements of through-plane thermal conductivities in a polymer electrolyte fuel cell," *Journal of Power Sources*, vol. 195, no. 1, pp. 249–256, 2010.

[79] O. S. Burheim, J. G. Pharoah, H. Lampert, P. J. S. Vie, and S. Kjelstrup, "Through-plane thermal conductivity of PEMFC porous transport layers," *Journal of Fuel Cell Science and Technology*, vol. 8, no. 2, p. 21013, 2011.

[80] O. S. Burheim, H. Su, S. Pasupathi, J. G. Pharoah, and B. G. Pollet, "Thermal conductivity and temperature profiles of the micro porous layers used for the polymer electrolyte membrane fuel cell," *International Journal of Hydrogen Energy*, vol. 38, no. 20, pp. 8437–8447, 2013.

[81] O. S. Burheim, G. Ellila, J. D. Fairweather, A. Labouriau, S. Kjelstrup, and J. G. Pharoah, "Ageing and thermal conductivity of porous transport layers used for PEM fuel cells," *Journal of Power Sources*, vol. 221, pp. 356–365, 2013.

[82] O. S. Burheim, H. Su, H. H. Hauge, S. Pasupathi, and B. G. Pollet, "Study of thermal conductivity of PEM fuel cell catalyst layers," *International Journal of Hydrogen Energy*, vol. 39, no. 17, pp. 9397–9408, 2014.

[83] M. Khandelwal and M. M. Mench, "Direct measurement of through-plane thermal conductivity and contact resistance in fuel cell materials," *Journal of Power Sources*, vol. 161, no. 2, pp. 1106–1115, 2006.

[84] I. Nitta, T. Hottinen, O. Himanen, and M. Mikkola, "Inhomogeneous compression of PEMFC gas diffusion layer: part I. Experimental," *Journal of Power Sources*, vol. 171, no. 1, pp. 26–36, 2007.

[85] J. Becker, R. Flckiger, M. Reum, F. N. Bchi, F. Marone, and M. Stampanoni, "Determination of material properties of gas diffusion layers: experiments and simulations using phase contrast tomographic microscopy," *Journal of the Electrochemical Society*, vol. 156, no. 10, pp. B1175–B1181, 2009.

[86] N. Zamel, X. Li, and J. Shen, "Numerical estimation of the effective electrical conductivity in carbon paper diffusion media," *Applied Energy*, vol. 93, pp. 39–44, 2012.

[87] M. Secanell, R. Songprakorp, A. Suleman, and N. Djilali, "Multi-objective optimization of a polymer electrolyte fuel cell membrane electrode assembly," *Energy & Environmental Science*, vol. 1, no. 3, p. 378, 2008.

[88] M. Secanell, B. Carnes, A. Suleman, and N. Djilali, "Numerical optimization of proton exchange membrane fuel cell cathodes," *Electrochimica Acta*, vol. 52, no. 7, pp. 2668–2682, 2007.

[89] S. Chu and A. Majumdar, "Opportunities and challenges for a sustainable energy future," *Nature*, vol. 488, no. 7411, pp. 294–303, 2012.

[90] C. Flox, M. Skoumal, J. Rubio-Garcia, T. Andreu, and J. R. Morante, "Strategies for enhancing electrochemical activity of carbon-based electrodes for all-vanadium redox flow batteries," *Applied Energy*, vol. 109, pp. 344–351, sep 2013.

[91] A. Forner-Cuenca, E. E. Penn, A. M. Oliveira, and F. R. Brushett, "Exploring the Role of Electrode Microstructure on the Performance of Non-Aqueous Redox Flow Batteries," *Journal of The Electrochemical Society*, vol. 166, pp. A2230–A2241, jun 2019.

[92] P.-C. Sui, X. Zhu, and N. Djilali, *Modeling of PEM Fuel Cell Catalyst Layers: Status and Outlook*, vol. 2. Springer Singapore, 2019.

[93] S. D. Knights, D. Wilkinson, and P. Beattie, "Electrochemical fuel cell with fluid distribution layer having non-uniform perforations," vol. 1, no. 19, 2003.

[94] N. Hussain, E. Van Steen, S. Tanaka, and P. Levecque, "Metal based gas diffusion layers for enhanced fuel cell performance at high current densities," *Journal of Power Sources*, vol. 337, pp. 18–24, 2017.

[95] S. Litster, C. R. Buie, T. Fabian, J. K. Eaton, and J. G. Santiago, "Active water management for PEM fuel cells," *Journal of the Electrochemical Society*, vol. 154, no. 10, pp. B1049–B1058, 2007.

[96] B. Zahiri, R. M. Felix, A. Hill, C. H. Kung, T. Sharma, J. D. Real, and W. Mérida, "Through-plane wettability tuning of fibrous carbon layers via O2 plasma treatment for enhanced water management," *Applied Surface Science*, vol. 458, no. June, pp. 32–42, 2018.

[97] F. B. Weng, B. S. Jou, C. W. Li, A. Su, and S. H. Chan, "The effect of low humidity on the uniformity and stability of segmented PEM fuel cells," *Journal of Power Sources*, vol. 181, no. 2, pp. 251–258, 2008.

[98] D. H. Jeon, K. N. Kim, S. M. Baek, and J. H. Nam, "The effect of relative humidity of the cathode on the performance and the uniformity of PEM fuel cells," *International Journal of Hydrogen Energy*, vol. 36, no. 19, pp. 12499–12511, 2011.

[99] G. Hinds, M. Stevens, J. Wilkinson, M. de Podesta, and S. Bell, "Novel in situ measurements of relative humidity in a polymer electrolyte membrane fuel cell," *Journal of Power Sources*, vol. 186, no. 1, pp. 52–57, 2009.

[100] V. A. Raileanu Ilie, S. Martemianov, and A. Thomas, "Investigation of the local temperature and overheat inside the membrane electrode assembly of PEM fuel cell," *International Journal of Hydrogen Energy*, vol. 41, no. 34, pp. 15528–15537, 2016.

[101] S. T. Ali, J. Lebæk, L. P. Nielsen, C. Mathiasen, P. Møller, and S. K. Kær, "Thin film thermocouples for in situ membrane electrode assembly temperature measurements in a polybenzimidazole-based high temperature proton exchange membrane unit cell," *Journal of Power Sources*, vol. 195, no. 15, pp. 4835–4841, 2010.

[102] H. Y. Wang, W. J. Yang, and Y. B. Kim, "Analyzing in-plane temperature distribution via a micro-temperature sensor in a unit polymer electrolyte membrane fuel cell," *Applied Energy*, vol. 124, pp. 148–155, 2014.

[103] C. Y. Lee and Y. M. Lee, "In-situ diagnosis of local fuel cell performance using novel micro sensors," *International Journal of Hydrogen Energy*, vol. 37, no. 5, pp. 4448–4456, 2012.

[104] C.-Y. Lee, S.-J. Lee, Y.-M. Lee, and K.-Y. Chu, "GDL in Micro Fuel Cell," *Fuel*, no. 217019, pp. 637–640, 2009.

[105] N. David, K. Von Schilling, P. M. Wild, and N. Djilali, "In situ measurement of relative humidity in a PEM fuel cell using fibre Bragg grating sensors," *International Journal of Hydrogen Energy*, vol. 39, no. 31, pp. 17638–17644, 2014.

[106] T. Lopes, O. Beruski, A. M. Manthanwar, I. Korkischko, R. Pugliesi, M. A. Stanojev, M. L. G. Andrade, E. N. Pistikopoulos, J. Perez, F. C. Fonseca, J. R. Meneghini, and A. R. Kucernak, "Spatially resolved oxygen reaction, water, and temperature distribution: Experimental results as a function of flow field and implications for polymer electrolyte fuel cell operation," *Applied Energy*, vol. 252, no. June, p. 113421, 2019.

[107] M. Reches, K. A. Mirica, R. Dasgupta, M. D. Dickey, M. J. Butte, and G. M. Whitesides, "Thread as a Matrix for Biomedical Assays," *ACS Applied Materials and Interfaces*, vol. 2, no. 6, pp. 1722–1728, 2010.

[108] X. Li, J. Tian, and W. Shen, "Thread as a versatile material for low-cost microfluidic diagnostics," *ACS Applied Materials and Interfaces*, vol. 2, no. 1, pp. 1–6, 2010.

[109] R. Safavieh, G. Z. Zhou, and D. Juncker, "Microfluidics made of yarns and knots: From fundamental properties to simple networks and operations," *Lab on a Chip*, vol. 11, no. 15, pp. 2618–2624, 2011.

[110] L. Yu, J. C. Yeo, R. H. Soon, T. Yeo, H. H. Lee, and C. T. Lim, "Highly Stretchable, Weavable, and Washable Piezoresistive Microfiber Sensors," *ACS Applied Materials and Interfaces*, vol. 10, no. 15, pp. 12773–12780, 2018.

[111] G. Kiaee, P. Mostafalu, M. Samandari, and S. Sonkusale, "A pH-Mediated Electronic Wound Dressing for Controlled Drug Delivery," *Advanced Healthcare Materials*, vol. 7, no. 18, pp. 1–8, 2018.

[112] J. W. Han, B. Kim, J. Li, and M. Meyyappan, "A carbon nanotube based ammonia sensor on cellulose paper," *RSC Advances*, vol. 4, no. 2, pp. 549–553, 2014.

[113] K. P. Yoo, L. T. Lim, N. K. Min, M. J. Lee, C. J. Lee, and C. W. Park, "Novel resistive-type humidity sensor based on multiwall carbon nanotube/polyimide composite films," *Sensors and Actuators, B: Chemical*, vol. 145, no. 1, pp. 120–125, 2010.

[114] A. Malekian, S. Salari, M. Tam, K. Oldknow, N. Djilali, and M. Bahrami, "Compressive behaviour of thin catalyst layers. Part I - Experimental study,"

International Journal of Hydrogen Energy, vol. 44, no. 33, pp. 18450–18460, 2019.

[115] Z. Fishman, J. Hinebaugh, and a. Bazylak, "Microscale Tomography Investigations of Heterogeneous Porosity Distributions of PEMFC GDLs," *Journal of The Electrochemical Society*, vol. 157, no. 11, p. B1643, 2010.

[116] K. J. Lange, P.-C. Sui, and N. Djilali, "Pore Scale Simulation of Transport and Electrochemical Reactions in Reconstructed PEMFC Catalyst Layers," *Journal of The Electrochemical Society*, vol. 157, no. 10, p. B1434, 2010.

[117] P. A. García-Salaberri, I. V. Zenyuk, A. D. Shum, G. Hwang, M. Vera, A. Z. Weber, and J. T. Gostick, "Analysis of representative elementary volume and through-plane regional characteristics of carbon-fiber papers: diffusivity, permeability and electrical/thermal conductivity," *International Journal of Heat and Mass Transfer*, vol. 127, pp. 687–703, 2018.

[118] J. T. Gostick, M. W. Fowler, M. D. Pritzker, M. A. Ioannidis, and L. M. Behra, "In-plane and through-plane gas permeability of carbon fiber electrode backing layers," *Journal of Power Sources*, vol. 162, no. 1, pp. 228–238, 2006.

[119] J. Wu, X. Z. Yuan, J. J. Martin, H. Wang, J. Zhang, J. Shen, S. Wu, and W. Merida, "A review of PEM fuel cell durability: Degradation mechanisms and mitigation strategies," *Journal of Power Sources*, vol. 184, no. 1, pp. 104–119, 2008.

[120] M. Liu, X. Pu, Z. Cong, Z. Liu, T. Liu, Y. Chen, J. Fu, W. Hu, and Z. L. Wang, "Resist-Dyed Textile Alkaline Zn Microbatteries with Significantly Suppressed Zn Dendrite Growth," *ACS Applied Materials and Interfaces*, vol. 11, no. 5, pp. 5095–5106, 2019.

[121] X. Huang, J. Liu, J. Ding, Y. Deng, W. Hu, and C. Zhong, "Toward Flexible and Wearable Zn-Air Batteries from Cotton Textile Waste," *ACS Omega*, vol. 4, no. 21, pp. 19341–19349, 2019.

[122] Q. Huang, D. Wang, and Z. Zheng, "Textile-Based Electrochemical Energy Storage Devices," *Advanced Energy Materials*, vol. 6, no. 22, pp. 1–28, 2016.

[123] S. Hasanpour, M. Hoorfar, and A. Phillion, "Different methods for determining porosity of gas diffusion layer using X-ray microtomography," *Electrochimica Acta*, vol. 185, 2015.

[124] L. M. Castano and A. B. Flatau, "Smart fabric sensors and e-textile technologies: A review," *Smart Materials and Structures*, vol. 23, no. 5, 2014.

[125] T. Pereira, P. Silva, H. Carvalho, and M. Carvalho, "Textile moisture sensor matrix for monitoring of diSabled and bed-rest patients," *EUROCON 2011 - International Conference on Computer as a Tool - Joint with Conftele 2011*, pp. 1–4, 2011.

[126] M. Stoppa and A. Chiolerio, "Wearable electronics and smart textiles: A critical review," *Sensors (Switzerland)*, vol. 14, no. 7, pp. 11957–11992, 2014.

[127] L. Wang, X. Fu, J. He, X. Shi, T. Chen, P. Chen, B. Wang, and H. Peng, "Application Challenges in Fiber and Textile Electronics," *Advanced Materials*, vol. 32, no. 5, pp. 1–25, 2020.

[128] T. R. Dargaville, B. L. Farrugia, J. A. Broadbent, S. Pace, Z. Upton, and N. H. Voelcker, "Sensors and imaging for wound healing: A review," *Biosensors and Bioelectronics*, vol. 41, no. 1, pp. 30–42, 2013.

[129] D. McColl, B. Cartlidge, and P. Connolly, "Real-time monitoring of moisture levels in wound dressings in vitro: An experimental study," *International Journal of Surgery*, vol. 5, no. 5, pp. 316–322, 2007.

[130] M. Akbari, A. Tamayol, S. Bagherifard, L. Serex, P. Mostafalu, N. Faramarzi, M. H. Mohammadi, and A. Khademhosseini, "Textile Technologies and Tissue Engineering: A Path Toward Organ Weaving," *Advanced Healthcare Materials*, vol. 5, no. 7, pp. 751–766, 2016.

[131] L. Li, Z. Wu, S. Yuan, and X. B. Zhang, "Advances and challenges for flexible energy storage and conversion devices and systems," *Energy and Environmental Science*, vol. 7, no. 7, pp. 2101–2122, 2014.

[132] L. Hu, M. Pasta, F. La Mantia, L. Cui, S. Jeong, H. D. Deshazer, J. W. Choi, S. M. Han, and Y. Cui, "Stretchable, porous, and conductive energy textiles," *Nano Letters*, vol. 10, no. 2, pp. 708–714, 2010.

[133] C. S. Boland, U. Khan, C. Backes, A. O'Neill, J. McCauley, S. Duane, R. Shanker, Y. Liu, I. Jurewicz, A. B. Dalton, and J. N. Coleman, "Sensitive, high-strain, high-rate bodily motion sensors based on graphene-rubber composites," *ACS Nano*, vol. 8, no. 9, pp. 8819–8830, 2014.

[134] L. Wang, L. Wang, Y. Zhang, J. Pan, S. Li, X. Sun, B. Zhang, and H. Peng, "Weaving Sensing Fibers into Electrochemical Fabric for Real-Time Health Monitoring," *Advanced Functional Materials*, vol. 28, no. 42, pp. 1–8, 2018.

[135] Q. Y. Tang, Y. C. Chan, and K. Zhang, "Fast response resistive humidity sensitivity of polyimide/multiwall carbon nanotube composite films," *Sensors and Actuators, B: Chemical*, vol. 152, no. 1, pp. 99–106, 2011.

[136] P. Zhu, Y. Liu, Z. Fang, Y. Kuang, Y. Zhang, C. Peng, and G. Chen, "Flexible and Highly Sensitive Humidity Sensor Based on Cellulose Nanofibers and Carbon Nanotube Composite Film," *Langmuir*, p. acs.langmuir.8b04259, 2019.

[137] T. Fei, K. Jiang, F. Jiang, R. Mu, and T. Zhang, "Humidity switching properties of sensors based on multiwalled carbon nanotubes/polyvinyl alcohol composite films," *Journal of Applied Polymer Science*, vol. 131, no. 1, pp. 1–7, 2014.

[138] S. H. Hwang, D. Kang, R. S. Ruoff, H. S. Shin, and Y. B. Park, "Poly(vinyl alcohol) reinforced and toughened with poly(dopamine)-treated graphene oxide, and its use for humidity sensing," *ACS Nano*, vol. 8, no. 7, pp. 6739–6747, 2014.

[139] A. Benchirouf, S. Palaniyappan, R. Ramalingame, P. Raghunandan, T. Jagemann, C. Müller, M. Hietschold, and O. Kanoun, "Electrical properties of multiwalled carbon nanotubes/PEDOT:PSS nanocomposites thin films under temperature and humidity effects," *Sensors and Actuators, B: Chemical*, vol. 224, pp. 344–350, 2016.

[140] S. L. Zhang, H. H. Choi, H. Y. Yue, and W. C. Yang, "Controlled exfoliation of molybdenum disulfide for developing thin film humidity sensor," *Current Applied Physics*, vol. 14, no. 3, pp. 264–268, 2014.

[141] U. Kalsoom, S. Waheed, and B. Paull, "Fabrication of Humidity Sensor Using 3D Printable Polymer Composite Containing Boron-Doped Diamonds and LiCl," *ACS Applied Materials and Interfaces*, vol. 12, no. 4, pp. 4962–4969, 2020.

[142] J. Weremczuk, G. Tarapata, and R. Jachowicz, "Humidity sensor printed on textile with use of ink-jet Technology," *Procedia Engineering*, vol. 47, pp. 1366–1369, 2012.

[143] L. Peterková, S. Rimpelová, I. Křížová, P. Slepička, N. S. Kasálková, V. Švorčík, and T. Ruml, "Biocompatibility of Ar plasma-treated fluorinated ethylene propylene: Adhesion and viability of human keratinocytes," *Materials Science and Engineering C*, vol. 100, no. October 2018, pp. 269–275, 2019.

[144] S. Harada, K. Kanao, Y. Yamamoto, T. Arie, S. Akita, and K. Takei, "Fully printed flexible fingerprint-like three-Axis tactile and slip force and temperature sensors for artificial skin," *ACS Nano*, vol. 8, no. 12, pp. 12851–12857, 2014.

[145] S. Y. Hong, Y. H. Lee, H. Park, S. W. Jin, Y. R. Jeong, J. Yun, I. You, G. Zi, and J. S. Ha, "Stretchable Active Matrix Temperature Sensor Array of Polyaniline Nanofibers for Electronic Skin," *Advanced Materials*, vol. 28, no. 5, pp. 930–935, 2016.

[146] T. Q. Trung, S. Ramasundaram, B. U. Hwang, and N. E. Lee, "An All-Elastomeric Transparent and Stretchable Temperature Sensor for Body-Attachable Wearable Electronics," *Advanced Materials*, vol. 28, no. 3, pp. 502–509, 2016.

[147] T. Vuorinen, J. Niittynen, T. Kankkunen, T. M. Kraft, and M. Mäntysalo, "Inkjet-printed graphene/PEDOT:PSS temperature sensors on a skin-conformable polyurethane substrate," *Scientific Reports*, vol. 6, no. September, pp. 1–8, 2016.

[148] K. S. Karimov, M. T. S. Chani, and F. A. Khalid, "Carbon nanotubes film based temperature sensors," *Physica E: Low-Dimensional Systems and Nanostructures*, vol. 43, no. 9, pp. 1701–1703, 2011.

[149] M. Tian, Y. Huang, W. Wang, R. Li, P. Liu, C. Liu, and Y. Zhang, "Temperature-dependent electrical properties of graphene nanoplatelets film dropped on flexible substrates," *Journal of Materials Research*, vol. 29, no. 11, pp. 1288–1294, 2014.

[150] S. R. Shin, R. Farzad, A. Tamayol, V. Manoharan, P. Mostafalu, Y. S. Zhang, M. Akbari, S. M. Jung, D. Kim, M. Comotto, N. Annabi, F. E. Al-Hazmi,

M. R. Dokmeci, and A. Khademhosseini, "A Bioactive Carbon Nanotube-Based Ink for Printing 2D and 3D Flexible Electronics," *Advanced Materials*, vol. 28, no. 17, pp. 3280–3289, 2016.

[151] N. Carneiro, A. P. Souto, E. Silva, A. Marimba, B. Tena, and H. Ferreira, "Dyeability of corona-treated fabrics Coloration Technology," *Coloration Technology*, vol. 117, pp. 298–302, 2001.

[152] W. Xu and X. Liu, "Surface modification of polyester fabric by corona discharge irradiation," *European Polymer Journal*, vol. 39, no. 1, pp. 199–202, 2003.

[153] Z. Sun, V. Nicolosi, D. Rickard, S. D. Bergin, D. Aherne, and J. N. Coleman, "Quantitative Evaluation of Surfactant-stabilized Single-walled Carbon Nanotubes: Dispersion Quality and Its Correlation with Zeta Potential," *The Journal of Physical Chemistry C*, vol. 112, no. 29, pp. 10692–10699, 2008.

[154] X. Yang, W. Wang, and M. Miao, "Moisture-Responsive Natural Fiber Coil-Structured Artificial Muscles," *ACS Applied Materials and Interfaces*, vol. 10, no. 38, pp. 32256–32264, 2018.

[155] L. Zhou, H. J. Forman, Y. Ge, and J. Lunec, "Multi-walled carbon nanotubes: A cytotoxicity study in relation to functionalization, dose and dispersion," *Toxicology in Vitro*, vol. 42, no. February, pp. 292–298, 2017.

[156] S. Nardecchia, M. C. Serrano, M. C. Gutiérrez, M. L. Ferrer, and F. Del Monte, "Modulating the cytocompatibility of tridimensional carbon nanotube-based scaffolds," *Journal of Materials Chemistry B*, vol. 1, no. 24, pp. 3064–3072, 2013.

[157] L. Peterková, S. Rimpelová, P. Slepička, I. Křížová, N. S. Kasálková, V. Švorčík, and T. Ruml, "Argon plasma-treated fluorinated ethylene propylene: Growth of primary dermal fibroblasts and mesenchymal stem cells," *Tissue and Cell*, vol. 58, no. February, pp. 121–129, 2019.

[158] M. De Nicola, S. Bellucci, E. Traversa, G. De Bellis, F. Micciulla, and L. Ghibelli, "Carbon nanotubes on Jurkat cells: Effects on cell viability and plasma membrane potential," *Journal of Physics Condensed Matter*, vol. 20, no. 47, 2008.

[159] W. Qian, X. Hu, W. He, R. Zhan, M. Liu, D. Zhou, Y. Huang, X. Hu, Z. Wang, G. Fei, J. Wu, M. Xing, H. Xia, and G. Luo, "Polydimethylsiloxane incorporated with reduced graphene oxide (rGO) sheets for wound dressing application: Preparation and characterization," *Colloids and Surfaces B: Biointerfaces*, vol. 166, pp. 61–71, 2018.

[160] L. Hao-ran, L. Xiao, N. Xin-ye, Y. Hui-lin, and Y. Lei, "A novel hydrogel-polydimethylsiloxane elastomer for wound dressing application," *Ferroelectrics*, vol. 523, no. 1, pp. 104–111, 2018.

[161] C. W. Li, Q. Wang, J. Li, M. Hu, S. J. Shi, Z. W. Li, G. L. Wu, H. H. Cui, Y. Y. Li, Q. Zhang, X. H. Yu, and L. C. Lu, "Silver nanoparticles/chitosan oligosaccharide/poly(vinyl alcohol) nanofiber promotes wound healing by activating TGFβ1/Smad signaling pathway," *International Journal of Nanomedicine*, vol. 11, pp. 373–387, 2016.

[162] I. Locher, *Technologies for System-on-textile integration*. PhD thesis, ETH, 2006.